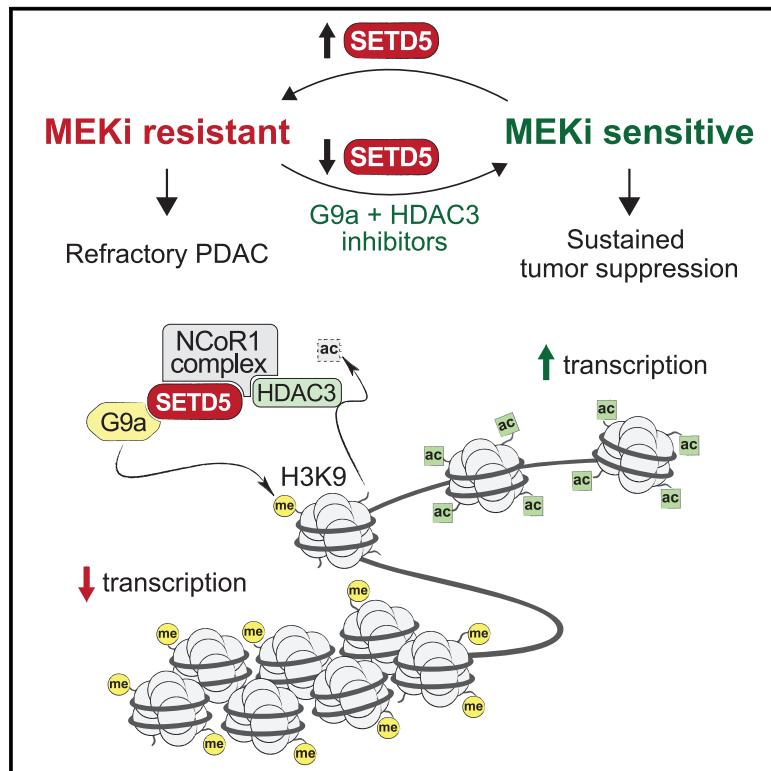


## SETD5-Coordinated Chromatin Reprogramming Regulates Adaptive Resistance to Targeted Pancreatic Cancer Therapy

### Graphical Abstract



### Authors

Zhentian Wang, Simone Hausmann, Ruitu Lyu, ..., Julien Sage, Or Gozani, Pawel K. Mazur

### Correspondence

ogozani@stanford.edu (O.G.),  
pkmazur@mdanderson.org (P.K.M.)

### In Brief

In pancreatic ductal adenocarcinoma (PDAC), a major roadblock in therapies targeting the KRAS-MAPK pathway, such as MEK1/2 inhibition (MEKi), is the rapid emergence of resistance. Wang et al. identify a clinically actionable epigenetic pathway mediated by SETD5 to drive PDAC resistance to MEKi.

### Highlights

- SETD5 is an epigenetic driver of pancreatic cancer resistance to MEK1/2 inhibition
- SETD5 has no intrinsic methylation activity on histones, including at H3 lysine 36
- A SETD5 co-repressor complex regulates a network of drug resistance pathways
- Co-targeting of MEK1/2 and the SETD5 complex results in sustained tumor inhibition



## Article

# SETD5-Coordinated Chromatin Reprogramming Regulates Adaptive Resistance to Targeted Pancreatic Cancer Therapy

Zhentian Wang,<sup>1,11</sup> Simone Hausmann,<sup>2,11</sup> Ruitu Lyu,<sup>3</sup> Tie-Mei Li,<sup>1</sup> Shane M. Lofgren,<sup>2</sup> Natasha M. Flores,<sup>2</sup> Mary E. Fuentes,<sup>2</sup> Marcello Caporicci,<sup>2</sup> Ze Yang,<sup>1</sup> Matthew Joseph Meiners,<sup>4</sup> Marcus Adrian Cheek,<sup>4</sup> Sarah Ann Howard,<sup>4</sup> Lichao Zhang,<sup>5</sup> Joshua Eric Elias,<sup>5</sup> Michael P. Kim,<sup>6</sup> Anirban Maitra,<sup>7</sup> Huamin Wang,<sup>7,8</sup> Michael Cory Bassik,<sup>9</sup> Michael-Christopher Keogh,<sup>4</sup> Julien Sage,<sup>9,10</sup> Or Gozani,<sup>1,\*</sup> and Pawel K. Mazur<sup>2,12,\*</sup>

<sup>1</sup>Department of Biology, Stanford University, Stanford, CA 94305, USA

<sup>2</sup>Department of Experimental Radiation Oncology, The University of Texas MD Anderson Cancer Center, Houston, TX 77030, USA

<sup>3</sup>Department of Chemistry, The University of Chicago, Chicago, IL 60637, USA

<sup>4</sup>EpiCypher Inc., Durham, NC 27709, USA

<sup>5</sup>Chan Zuckerberg Biohub, Stanford, CA 94305, USA

<sup>6</sup>Department of Surgical Oncology, The University of Texas MD Anderson Cancer Center, Houston, TX 77030, USA

<sup>7</sup>Department of Translational Molecular Pathology, The University of Texas MD Anderson Cancer Center, Houston, TX 77030, USA

<sup>8</sup>Department of Pathology, The University of Texas MD Anderson Cancer Center, Houston, TX 77030, USA

<sup>9</sup>Department of Genetics, Stanford University School of Medicine, Stanford, CA 94305, USA

<sup>10</sup>Department of Pediatrics, Stanford University School of Medicine, Stanford, CA 94305, USA

<sup>11</sup>These authors contributed equally

<sup>12</sup>Lead Contact

\*Correspondence: [ogozani@stanford.edu](mailto:ogozani@stanford.edu) (O.G.), [pkmazur@mdanderson.org](mailto:pkmazur@mdanderson.org) (P.K.M.)

<https://doi.org/10.1016/j.ccell.2020.04.014>

## SUMMARY

Molecular mechanisms underlying adaptive targeted therapy resistance in pancreatic ductal adenocarcinoma (PDAC) are poorly understood. Here, we identify SETD5 as a major driver of PDAC resistance to MEK1/2 inhibition (MEKi). SETD5 is induced by MEKi resistance and its deletion restores refractory PDAC vulnerability to MEKi therapy in mouse models and patient-derived xenografts. SETD5 lacks histone methyltransferase activity but scaffolds a co-repressor complex, including HDAC3 and G9a. Gene silencing by the SETD5 complex regulates known drug resistance pathways to reprogram cellular responses to MEKi. Pharmacological co-targeting of MEK1/2, HDAC3, and G9a sustains PDAC tumor growth inhibition *in vivo*. Our work uncovers SETD5 as a key mediator of acquired MEKi therapy resistance in PDAC and suggests a context for advancing MEKi use in the clinic.

## INTRODUCTION

Pancreatic ductal adenocarcinoma (PDAC) is one of the deadliest major cancer types, killing on a yearly basis more than 430,000 patients worldwide (Rawla et al., 2019). The 5-year survival rate of PDAC is <8%, with progress in improving outcomes

lagging behind most other neoplastic diseases (Siegel et al., 2019). The difficult prognosis of PDAC is due to the disease typically being diagnosed at an advanced stage, at which point surgical resection is not beneficial, and the absence of effective medical options (Ryan et al., 2014). The vast majority of PDAC cases are driven by oncogenic activating mutations in KRAS

### Significance

Oncogenic KRAS signaling is a hallmark of PDAC, a lethal malignancy with few treatment options. A major roadblock in deploying therapies targeting the KRAS-MAPK pathway is the rapid emergence of resistant cancer cells. Here, we show that SETD5 is a clinically actionable epigenetic driver of PDAC resistance to MEKi. We find that acute deletion of SETD5 in aggressive PDAC refractory to MEKi restores the vulnerability of tumors to targeted MEKi therapy. Pharmacologic blockade with inhibitors of histone-modifying activities associated with SETD5 disrupts a SETD5-driven resistance program and sustains inhibition of tumor growth by MEKi in pre-clinical murine and human models of PDAC. Together, our study reveals a potential clinical path for rationale testing of FDA-approved MEK inhibitors to treat PDAC.



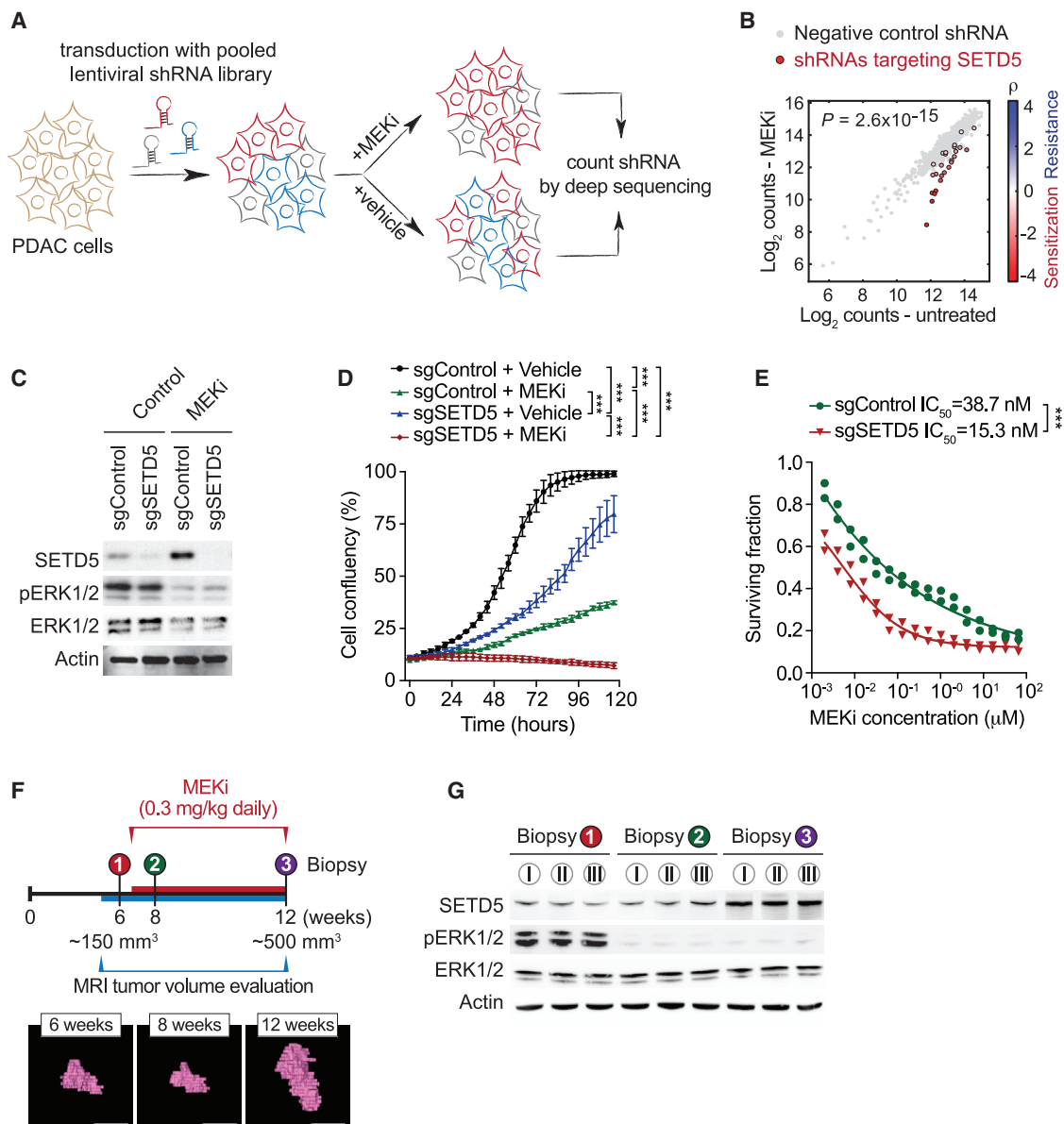


**Figure 1. Identification of SETD5 as a Candidate Regulator of PDAC Cell Resistance to MEKi**

(A) Schematic of the screen to identify methyltransferases conferring sensitivity to the MEKi trametinib. MiaPaCa2 pancreatic cancer cells infected with a pooled high-coverage shRNA library were split into two subpopulations and treated as indicated. The frequency of shRNA-encoding constructs in each subpopulation was determined by deep sequencing. See also [Table S1](#).

(B) shRNAs targeting SETD5 sensitize cells to MEKi. A quantitative resistance phenotype  $\rho$  was calculated for each shRNA based on the sequencing frequency in the two subpopulations. The graph compares the distribution of  $\rho$  for shRNAs targeting a gene of interest (shown here SETD5) to the  $\rho$  distribution for negative control shRNAs using the Mann-Whitney U test that yielded a p value for the gene.

(C) Western analysis with the indicated antibodies of whole-cell extracts (WCEs) from MiaPaCa2 cells  $\pm$  MEKi and depleted for SETD5 by Cas9/sgRNA (sgSETD5) or control (sgControl). Actin shown as a loading control.

(D) SETD5 knockdown synergizes with MEKi to attenuate cell proliferation. Confluency of MiaPaCa2 cells as in (C) treated for 120 h with MEKi (trametinib 15 nM) or vehicle control. Data are represented as mean  $\pm$  SEM of three technical replicates in two independent experiments. \* $p < 0.033$ , \*\* $p < 0.002$ , \*\*\* $p < 0.0001$  by two-way ANOVA with Tukey's testing for multiple comparisons.

(E) SETD5 depletion increases MiaPaCa2 cells sensitivity to MEKi. Cellular viability in response to trametinib at the indicated doses in MiaPaCa2 cells  $\pm$  SETD5. The calculated geometric mean half-maximum inhibitory concentration (IC<sub>50</sub>) values for MEKi are shown. Data represented as mean  $\pm$  SEM of three technical replicates in two independent experiments.

(F) Schematic of acquisition of pancreatic tissue biopsies from *Kras;p53* PDAC mouse model through abdominal laparotomy. The tumor biopsy cores were removed from mice before treatment (first biopsy, naive tumor, red) after initial treatment with MEKi (second biopsy, MEKi-responsive tumor, green) and upon

(legend continued on next page)

(Almoguera et al., 1988). However, besides recent promising data with KRAS(G12C)-specific inhibitors (a mutation found in <1% of PDAC) (Canon et al., 2019), drugging the KRAS mutations typically associated with PDAC has been unsuccessful (Stephen et al., 2014). As an alternative approach, drug discovery efforts have focused on targeting downstream KRAS effector pathways. In particular, drugs targeting the mitogen-activated protein kinase (MAPK) signaling cascade, a canonical pathway downstream of KRAS, have been clinically explored (Collisson et al., 2012; Manchado et al., 2016; Sun et al., 2017; Zhao and Adjei, 2014). MEK inhibition (MEKi)-based therapies have achieved FDA approval for some cancer types; however, clinical trials for PDAC have been less encouraging (Bodoky et al., 2012; Infante et al., 2014). The failure of MEKi in PDAC is likely due to adaptive signaling and the development of therapy resistance (Ponz-Sarvise et al., 2019). Thus, understanding the mechanisms underlying resistance acquisition in PDAC to targeted therapies is likely to lead to improved treatment modalities (Sun et al., 2017). In this context, pathways implicated in promoting MEKi resistance in PDAC include cellular programs that regulate oxidative phosphorylation and mitochondrial function, autophagy, lysosome activity, and compensatory induction of other pathways, such as phosphoinositide 3-kinase (PI3K) signaling, receptor tyrosine kinase signaling pathways (e.g., ERBB and FGFR1), and YAP1-regulated pathways (Bryant et al., 2019; Kapoor et al., 2014; Kinsey et al., 2019b; Manchado et al., 2016; Perera et al., 2015; Ponz-Sarvise et al., 2019; Shao et al., 2014; Viale et al., 2014). While treatment regimens using dual inhibition of MEK and certain resistance pathways (e.g., PI3K and EGFR) have to date been ineffective (Chung et al., 2017; Ko et al., 2016), ongoing trials co-targeting autophagy and oxidative phosphorylation are pending (Kinsey et al., 2019a; Molina et al., 2018). However, whether there are underlying clinically actionable epigenetic-based mechanisms regulating general resistance programs is not known.

The chromatin-associated protein SETD5 contains a catalytic methyltransferase SET domain and is thus annotated as a candidate protein lysine methyltransferase (KMT) (Husmann and Gozani, 2019). However, whether SETD5 is an active enzyme is unclear. The *SETD5* gene is commonly mutated in patients with intellectual disabilities and autism spectrum disorders (Deliu et al., 2018; Grozeva et al., 2014). SETD5 knockout mice die early in development due to cardiovascular defects and other abnormalities and SETD5 deletion in embryonic stem cells impaired proliferation and differentiation with altered gene expression (Deliu et al., 2018; Osipovich et al., 2016; Sessa et al., 2019). *Setd5* haploinsufficiency also leads to aberrant gene expression in neuronal tissue and is associated with cognitive and behavioral defects in mice (Deliu et al., 2018; Sessa et al., 2019). Finally, independent *Sleeping Beauty* transposon mutagenesis-based *in vivo* screens identified *SETD5* as a common insertion site that cooperates with KRAS to accelerate pancreatic carcinogenesis (Mann et al., 2012; Perez-Man-

cera et al., 2012). However, functions for SETD5 in cancer are largely unexplored.

## RESULTS

### Identification of SETD5 as a Candidate Regulator of PDAC Cell Resistance to MEKi

To explore possible connections between chromatin regulation, protein methylation, and the development of targeted MEKi therapy resistance in Ras-driven pancreatic cancer, we performed a high-content small hairpin RNA (shRNA) screen (Kampmann et al., 2014). The pancreatic cancer cell line MiaPaCa2, which harbors mutant KRAS (Sulahian et al., 2019), was transduced with a pooled high-coverage library containing 25 independent shRNAs directed against each of 95 known and putative human methyltransferase genes, including the vast majority of known KMTs present in the human genome (see schematic Figure 1A). After transduction, cells were treated with the MEKi trametinib or vehicle control and differences in shRNA abundance after 12 days were used to identify candidate genes influencing the drug response (Figures 1A and 1B) (Sulahian et al., 2019). Notably, out of the 2,375 shRNAs in the library, the ones that rendered cells most sensitive to trametinib targeted the candidate histone KMT *SETD5* (Figure 1B; Table S1). The direct depletion of SETD5 in MiaPaCa2 cells (Figure 1C) attenuated cellular proliferation, although to a lesser degree than trametinib treatment (Figure 1D). Combining SETD5 depletion with trametinib treatment effectively inhibited cell proliferation (Figure 1D), with SETD5 depletion decreasing the half-maximum inhibitory concentration of trametinib in MiaPaCa2 and five additional human PDAC cell lines by roughly 2.5-fold (Figures 1E and S1A–S1E). Consistent with these results, computational analysis of publicly available gene expression data suggests that *SETD5* is overexpressed in pancreatic cancer (Figure S1F). Furthermore, SETD5 immunohistological signal is high in human PDAC samples relative to healthy tissue and this signal negatively correlates with patient survival (Figures S1G and S1H). Based on these data and previous studies (Mann et al., 2012; Perez-Mancera et al., 2012) we postulated a role for SETD5 in PDAC pathology.

We generated conditional *Setd5<sup>LoxP/LoxP</sup>* knockout mice to test the role of SETD5 in cancer *in vivo*. *Setd5<sup>LoxP/LoxP</sup>* mice develop normally, are viable, and fertile (data not shown). Deletion of *Setd5* in the pancreas using the pancreas-specific Cre-recombinase-expressing strain *Ptf1a<sup>Cre/+</sup>* (Kawaguchi et al., 2002) (Figure S2A) resulted in no apparent developmental consequences (data not shown). To investigate the role of SETD5 in KRAS-driven PDAC development, we used the *Ptf1a<sup>+Cre</sup>; Kras<sup>+/LSL-G12D</sup>; p53<sup>LoxP/LoxP</sup>* (*Kras;p53*) mutant model in which morbid PDAC develops with 100% penetrance 6–8 weeks after birth (Bardeesy et al., 2006; Hingorani et al., 2005). In this aggressive malignancy model, *Setd5* deletion resulted in a modest extension in median survival relative to control (Figures S2B and S2C; data not shown). These data suggest a more

tumor relapse with increased volume (third biopsy, MEKi-resistant tumor, purple). Representative magnetic resonance imaging (MRI) scans to analyze tumor volume in *Kras;p53* mutant mice are shown. Scale bars, 10 mm.

(G) SETD5 expression increases in PDAC tumors upon the development of MEKi resistance. Western analysis with the indicated antibodies of PDAC tissue biopsies from *Kras;p53* mouse model as described in (F). Three independent and representative samples are shown for each biopsy stage. See also Figure S1.

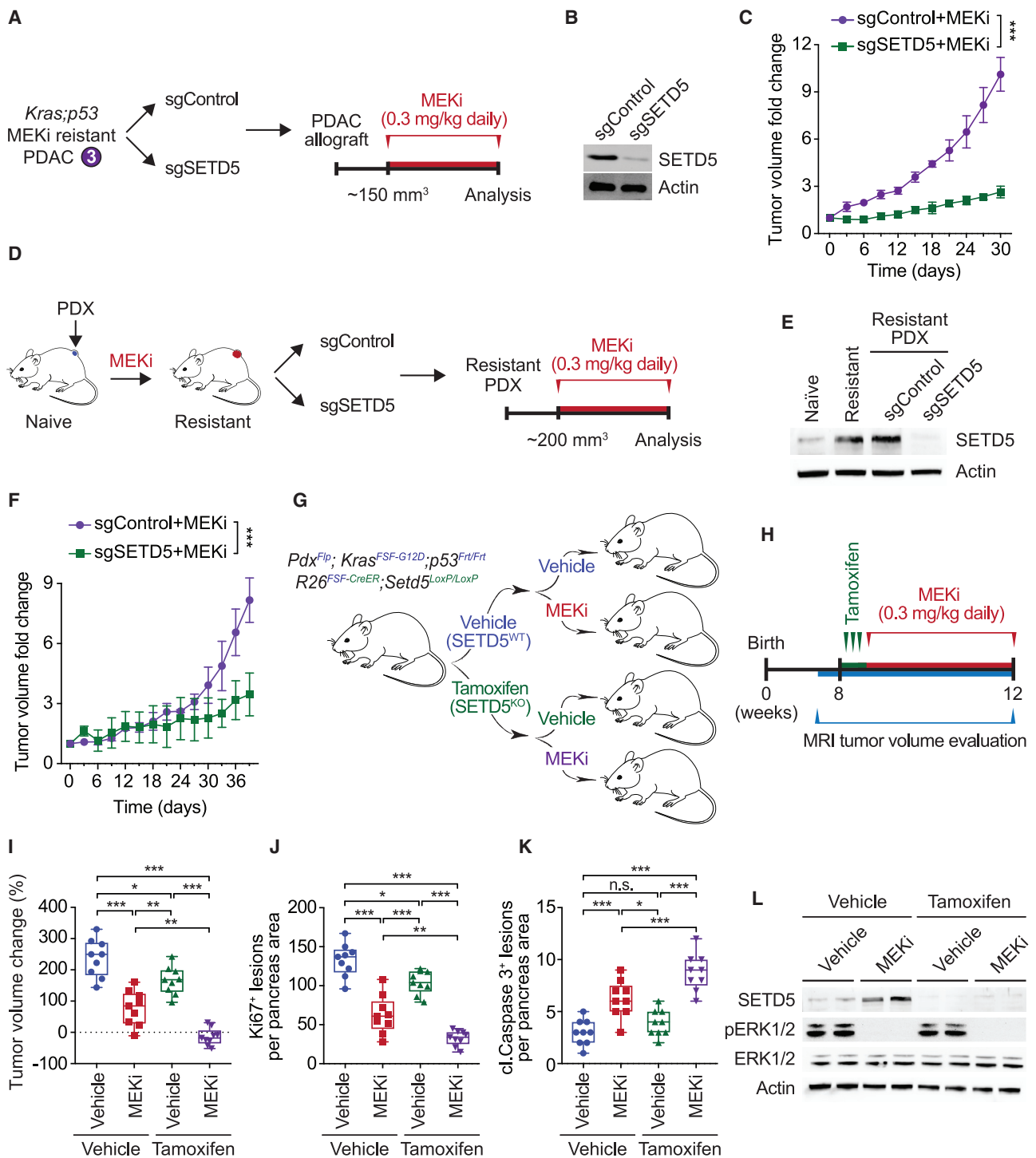


**Figure 2. SETD5 Depletion Re-sensitizes Resistant PDAC to Trametinib in PDX and Mouse Models In Vivo**

(A) Schematic of generation of PDAC allografts in syngeneic mice established from MEKi-resistant tumor biopsies (as in Figure 1F)  $\pm$  SETD5. Trametinib treatment schedule (MEKi, 0.3 mg/kg by intraperitoneal injection once daily) is shown.

(B) Western blots with the indicated antibodies of a representative sample for each condition described in (A) are shown. Actin is shown as a loading control.

(C) SETD5 depletion re-sensitizes PDAC allografts to MEKi. Quantification of mouse allograft tumor volume growth in syngeneic mice ( $n = 8$  mice, for each treatment group). \* $p < 0.033$ , \*\* $p < 0.002$ , \*\*\* $p < 0.0001$  by two-way ANOVA with Tukey's testing for multiple comparisons. Data are represented as mean  $\pm$  SEM.

(D) Schematic to generate MEKi-resistant primary human PDAC for PDX studies. Patient tumor samples were grafted subcutaneously to immunocompromised NSG mice. Once tumor volume reached  $200 \text{ mm}^3$ , mice were treated with trametinib 0.3 mg/kg by intraperitoneal injection once daily until tumor growth relapsed

(legend continued on next page)

specialized role for SETD5 in tumor response to therapy rather than broadly regulating tumor development.

To directly explore a role for SETD5 *in vivo* in tumor responses to RAS-pathway modulation, we obtained serial biopsies of PDAC tissue from *Kras;p53* mice: one sample before trametinib treatment, and two additional samples taken early and late during the course of the treatment protocol (Figure 1F). Tumor size was monitored by magnetic resonance imaging (MRI) (Liu et al., 2019) to optimize consistent biopsy acquisition of (1) naive (untreated), (2) trametinib-responsive, or (3) trametinib-resistant cancer tissues (Figure 1F). Serial biopsies were obtained by laparotomy (Sastru and Olive, 2014) to mitigate potential tumor tissue heterogeneity. Inhibition of ERK1/2 phosphorylation was observed at time points 2 and 3, indicating that trametinib remained effective despite progression of resistant tumors (Figure 1G); consistent with PDAC resistance mechanisms not acting via MAPK signaling reactivation (Kapoor et al., 2014; Shao et al., 2014). Notably, SETD5 expression is higher in the trametinib-refractory tumor samples compared with the trametinib-responsive and naive PDAC samples (Figure 1G). A similar increase in SETD5 expression is observed in PDAC biopsies upon prolonged exposure to selumetinib, an independent MEKi (Banerji et al., 2010) (Figures S2D and S2E). Moreover, the expression of SETD5 mRNA and protein increases in cells derived from naive murine PDAC tumors (hereto referred to as KPC<sub>N</sub> cells) cultured to develop resistance to different MEK inhibitors relative to control-treated cells (Figures S2F and S2G). Thus, increased SETD5 expression correlates with the development of resistance to a variety of MEK inhibitors both in cells and *in vivo* in a widely used PDAC mouse model.

### SETD5 Depletion Re-sensitizes Resistant PDAC to Trametinib in PDX and Mouse Models *In Vivo*

Cell lines were established from trametinib-resistant PDAC tumors (hereto referred to as KPC<sub>R</sub> cells) to test *in vivo* responsiveness of trametinib-resistant allografts to MEKi ± SETD5 (Figures 2A and 2B). The control allograft tumors are resistant to trametinib and expand rapidly in the presence of drug, whereas SETD5-depletion restores sensitivity to trametinib as allograft tumor

growth is impaired (Figure 2C). A patient-derived xenograft (PDX)-based model was next developed to explore the development of MEKi resistance in human PDAC (schematic, Figure 2D). Growing PDAC PDX tumors of approximately 200 mm<sup>3</sup> were exposed to trametinib until tumor expansion recommenced (~5 weeks), indicating drug resistance. Cells isolated from the trametinib-resistant PDX tumor ± SETD5 (Figure 2E) were then re-tested in xenograft tumor studies in the presence of trametinib. As expected, xenografts from relapsed trametinib-resistant tumors grow robustly despite trametinib; however, MEKi treatment impaired growth of SET5-knockdown tumors (Figure 2F).

To address if maintenance of trametinib resistance in PDAC tumors *in vivo* actively requires SETD5 expression, a dual-recombinase approach was used to delete *Setd5* in established tumors (Schonhuber et al., 2014). PDAC tumors were formed using *Pdx1<sup>Flp</sup>;Kras<sup>FSF-G12D</sup>;p53<sup>Frt/Frt</sup>;R26<sup>FSF-CreER</sup>;Setd5<sup>LoxP/LoxP</sup>* mice, in which *Pdx1*-driven expression of Flp-recombinase causes pancreas-specific expression of oncogenic KRAS, deletion of p53, and expression of tamoxifen-inducible Cre (CreER) (schematic, Figure 2G). *Setd5* was deleted in tumors that reached ~150 mm<sup>3</sup> by treating mice with tamoxifen to activate CreER, which is expressed exclusively in the Flp-recombined epithelial pancreatic cells (*Rosa26<sup>FSF-CreER</sup>*) (Figures 2H and S2H). Tumors were then treated with trametinib or vehicle (control) and tumor volume change evaluated by MRI (Figure 2H). The single intervention of trametinib treatment or SETD5 deletion in established PDAC each modestly slowed but did not eliminate tumor growth (Figures 2I–2K and S2I). Notably, combining administration of tamoxifen (to knockout *Setd5*) with trametinib halted tumor growth and caused some tumors to regress in size (Figures 2I–K and S2I). Analyses of tumor biopsy lysates showed that SETD5 protein was not expressed in tamoxifen-treated mice and that trametinib inhibited ERK1/2 phosphorylation (Figure 2L).

### SETD5 Lacks Intrinsic Histone Lysine Methyltransferase Activity

While SET domain proteins are frequently active KMTs, the SET domain of SETD5 lacks key conserved residues that bind to the

(~5 weeks), indicating drug resistance. Resistant cells were modified to express Cas9/sgRNA targeting *SETD5* (sgSETD5) or control (sgControl) and tested for xenograft growth with treatment as shown.

(E) Western blots with the indicated antibodies of PDX samples in different stages described in (D). A representative sample for each condition is shown. Actin is shown as a loading control.

(F) SETD5 depletion restores refractory PDAC PDX tumor sensitivity to MEKi. Tumor volume quantification of MEKi-resistant patient-derived PDAC xenografts described in (D) in immunocompromised mice ( $n = 8$  mice, for each treatment group). \* $p < 0.033$ , \*\* $p < 0.002$ , \*\*\* $p < 0.0001$  by two-way ANOVA with Tukey's testing for multiple comparisons. Data are represented as mean ± SEM.

(G) Schematic of dual-recombinase (Flp/Frt, Cre/LoxP) system to acutely delete *SETD5* *in vivo* in aggressive PDAC. Activation of *Kras<sup>FSF-G12D</sup>* and deletion of *p53<sup>Frt/Frt</sup>* alleles in mouse pancreata (*Pdx1<sup>Flp</sup>*) results in development of malignant PDAC. Time-specific tamoxifen-mediated *Rosa26<sup>FSF-CreERT2</sup>* activation allows for recombination of the conditional *Setd5<sup>LoxP/LoxP</sup>* allele with loss of SETD5 expression (SETD5<sup>KO</sup>) in established PDAC. Control animals that received vehicle express wild-type SETD5<sup>WT</sup>. Subsequently mice were treated with placebo (vehicle) or trametinib (MEKi, 0.3 mg/kg, intraperitoneal injection once daily).

(H) Treatment schedule for administration of tamoxifen, MEKi or placebo (vehicle) in the system described in (G).

(I) Deletion of SETD5 in established PDAC cooperates with MEKi to suppress tumor growth. Quantification of PDAC volume change based on MRI scans (detailed procedure in the STAR Methods) in mice described in (G and H) ( $n = 9$  mice for each experimental group). Boxes, 25th to 75th percentiles; whiskers, minimum to maximum; center line, median; \* $p < 0.033$ , \*\* $p < 0.002$ , \*\*\* $p < 0.0001$  by two-way ANOVA with Tukey's testing for multiple comparisons. Scale bars, 100 μm.

(J and K) (J) Quantification of proliferation (Ki67<sup>+</sup> cells), and (K) cleaved caspase-3 (cl.Caspase3<sup>+</sup> cells) a marker of apoptosis in samples as in (I). Boxes, 25th to 75th percentile; whiskers, minimum to maximum; center line, median; arrowheads, positive cleaved caspase-3 cells; \* $p < 0.033$ , \*\* $p < 0.002$ , \*\*\* $p < 0.0001$  by two-way ANOVA with Tukey's testing for multiple comparisons. Data are represented as mean ± SEM. Scale bars, 100 μm.

(L) Western blots with the indicated antibodies of the indicated pancreatic tissue lysates. Two independent and representative samples are shown for each genotype. Actin is shown as a loading control.

See also Figure S2.

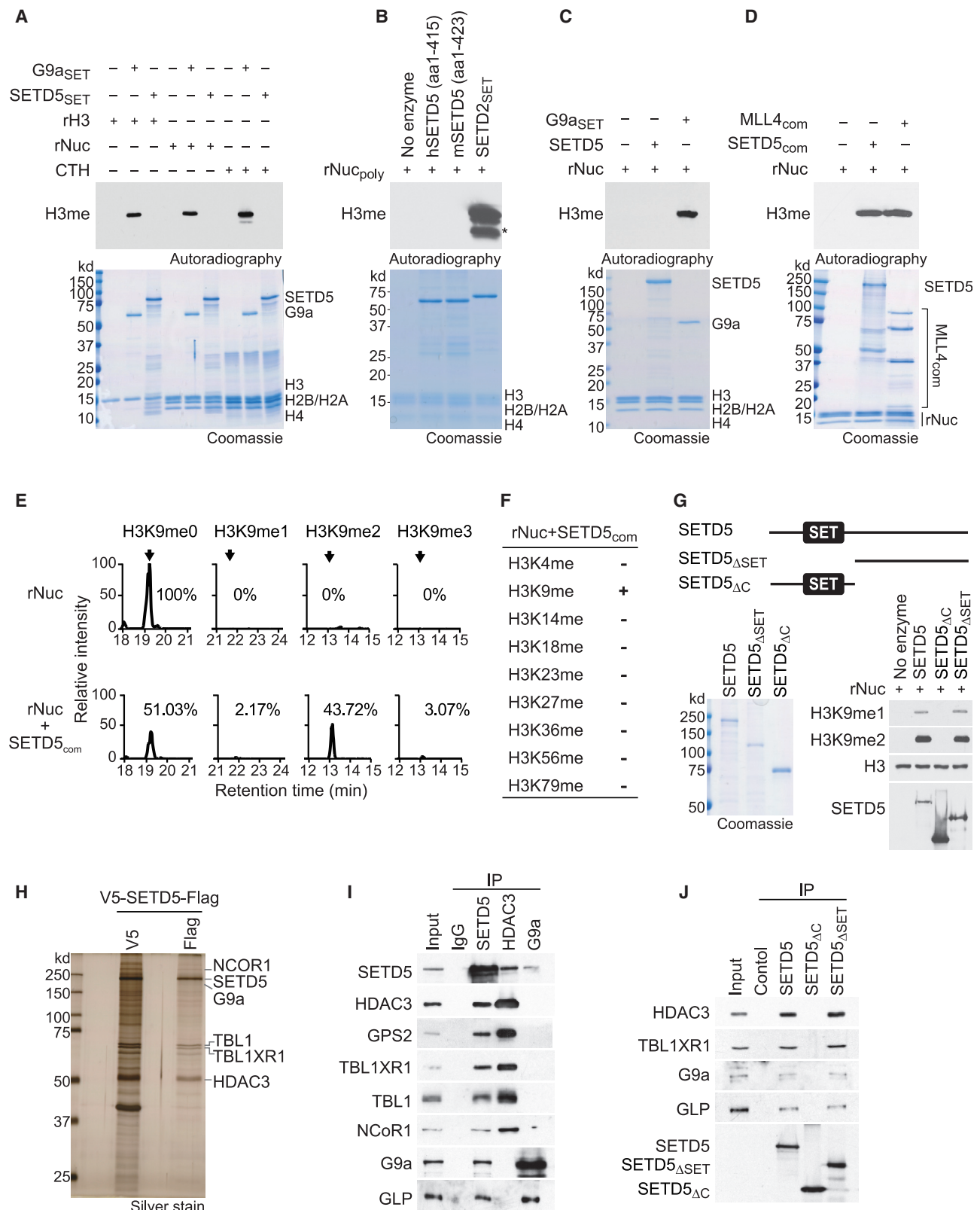


**Figure 3. SETD5 Has No Intrinsic Histone Lysine Methyltransferase Activity but Is Present in a Complex that Methylates H3K9**

(A) SETD5 does not methylate histones or nucleosomes. *In vitro* methylation assays with recombinant SETD5<sub>SET</sub> (GST-SETD5 residues 1–520) or positive control G9a<sub>SET</sub> (GST-G9a SET domain) on recombinant histone H3 (rH3), purified calf thymus histones (CTH), or recombinant nucleosomes (rNuc) substrates as

(legend continued on next page)

methyl donor S-adenosyl methionine and are present on all known active SET enzymes (Figure S3A) (Mas et al., 2016). Surprisingly, SETD5 was recently reported to be a robust H3K36 trimethylase (Sessa et al., 2019). However, the recombinant SET domain of SETD5 did not methylate recombinant histone H3, recombinant nucleosome, or purified histones (Figure 3A). In contrast, the positive control catalytic domain of the H3K9 KMT G9a methylated all three histone substrates (Figure 3A). We did not detect methylation on any histone residue, including H3K36, using the same SETD5 derivative (murine SETD5 amino acids 1–423) and reaction conditions reported in (Sessa et al., 2019) (Figures 3B and S3B). In contrast, H3K36 was methylated by SETD2, the principle human enzyme that generates physiologic H3K36me3 (Husmann and Gozani, 2019) (Figures 3B and S3B). Finally, in contrast to several positive controls (Figures S3C–S3F), full-length recombinant SETD5 did not methylate histones (Figure 3C).

Some KMTs are active only in the context of a macromolecular complex (i.e., MLL1–4) (Husmann and Gozani, 2019); indeed, like the positive control MLL4 complex, tandem-tag affinity purified SETD5 (hereto referred to as SETD5<sub>com</sub>) from 293T cells methylated nucleosomes on H3 (Figure 3D). Tandem mass spectrometry analysis of the SETD5<sub>com</sub>-catalyzed reaction identified primarily H3K9 dimethylation (Figures 3E and S3G). Methylation was not detected on any other lysine residue of H3, including H3K36 (Figures 3F and S3H). Notably, the SET domain of SETD5 is dispensable for catalyzing H3K9 methylation, as a complex purified with a C-terminal SETD5 derivative lacking the SET domain (SETD5<sub>ΔSET</sub>) methylates H3K9, and a complex purified with an N-terminal SETD5 derivative containing the SET domain but missing the C terminus (SETD5<sub>ΔC</sub>) lacks methylation activity (Figure 3G). We note that SETD5 did not methylate any of over 9,000 proteins present on a protein array (Mazur et al., 2014) and it had no activity on fractionated pancreatic can-

cer cell lysates, suggesting that SETD5 does not methylate a non-histone protein (Figures S3I and S3J; data not shown). Thus, SETD5 does not methylate H3K36 and indeed lacks intrinsic histone methylation activity (see Discussion). These data also suggest that an H3K9-specific KMT associates with SETD5.

### SETD5 Forms a Distinct Co-repressor Complex with NCoR1/HDAC3 and G9a/GLP

Analysis of SETD5<sub>com</sub> by mass spectrometry identified components of the NCoR1-HDAC3 complex, which is known to interact with SETD5 (Osipovich et al., 2016), and the H3K9 KMTs G9a and GLP (Tachibana et al., 2001) but no other KMTs (Figure 3H; Table S2; data not shown). The interactions between SETD5 and the NCoR1-HDAC3 complex and with G9a/GLP were also observed in immunoprecipitation (IP)-western analyses (Figure 3I). In reverse IPs, HDAC3 and G9a each separately immunoprecipitated SETD5; however, G9a and GLP were not in the HDAC3 IP, and components of the NCoR1-HDAC3 complex were not detected in the G9a IP (Figure 3I). These data suggest that SETD5 abundance is low compared with that of the NCoR1-HDAC3 complex and G9a/GLP as all three components are all only present in the SETD5 IP. Furthermore, the observed interactions of SETD5 with two repressive histone-modifying activities (histone deacetylation and H3K9 methylation) suggests that SETD5 scaffolds a distinct co-repressor complex. Finally, SETD5 and SETD5<sub>ΔSET</sub>, but not SETD5<sub>ΔC</sub>, interact with HDAC3 and G9a/GLP (Figure 3J). Thus, the C terminus region of SETD5 is necessary for H3K9 methylation and mediates the interaction with HDAC3, G9a/GLP.

We postulated that G9a and GLP, two KMTs that generate H3K9me1/2 and interact with SETD5, are responsible for the methylation activity associated with SETD5<sub>com</sub>. To test this idea, SETD5<sub>com</sub> was purified from control 293T cells or 293T

indicated. Top panel, [<sup>3</sup>H]S-adenosyl methionine is the methyl donor and methylation visualized by autoradiography and indicated as H3me. Bottom panel, Coomassie stain of proteins in the reaction.

(B) SETD5 does not methylate poly-nucleosomes, whereas SETD2 does. *In vitro* methylation assays as in (A) with hSETD5 (amino acids [aa]: 1–415) (human SETD5 residues 1–415), mSETD5 (aa: 1–423) (murine SETD5 residues 1–423 as in Sessa et al., 2019), and positive control SETD2<sub>SET</sub> (GST-SETD2 SET domain) on rNuc<sub>poly</sub> (H3.3-containing recombinant poly-nucleosomes as in Sessa et al., 2019). Top panel, autoradiogram of methylation assay. Bottom panel, Coomassie stain of proteins in the reaction. Asterisk indicates cleaved H3 breakdown product.

(C) Full-length SETD5 does not methylate nucleosomes. *In vitro* methylation assays as in (A) with full-length SETD5 on rNuc as indicated. Top panel, autoradiogram of methylation assay. Bottom panel, Coomassie stain of proteins in the reaction.

(D) Methylation of H3 by the SETD5 complex. *In vitro* methylation assay as in (A) on recombinant nucleosomes with tandem-affinity-purified SETD5 complex (SETD5<sub>com</sub>) from 293T cells. MLL4 complex (MLL4<sub>com</sub>) used as a positive control. Top panel, autoradiogram of methylation assay. Bottom panel, Coomassie stain of proteins in the reaction as indicated.

(E) SETD5<sub>com</sub> primarily di-methylates H3K9. Selected ion chromatograms for non-, mono-, di-, and tri-methyl H3K9 peptides from trypsin digestion of SETD5<sub>com</sub> methylation reactions on recombinant nucleosomes. High-pressure liquid chromatography elution profiles show a 10-ppm mass window around expected peptide masses, peptide sequence KSTGGKAPR, K9 is underlined; m/z are 535.3037 (H3K9me0), 542.3115 (H3K9me1), 521.3062 (H3K9me2), and 528.3140 (H3K9me3). Arrows indicate elution peaks of non-, mono-, di-, and tri-methylated H3K9 peptides in the profiles and percent methyl state is indicated. See also Figure S3G.

(F) SETD5<sub>com</sub> methylates H3K9 but not any other H3 lysine residue. Summary of H3 lysine methylation states detected in (E) by tandem mass spectrometry. See also Figure S3H.

(G) The SETD5 SET domain is dispensable for SETD5<sub>com</sub> H3K9 methylation activity. Methylation assays as in (D) with the indicated V5-SETD5-Flag derivatives. Top panel, schematic of SETD5 constructs with the position of the SET domains shown: SETD5, full-length SETD5; SETD5<sub>ΔSET</sub>, N-terminal truncation; SETD5<sub>ΔC</sub>, C-terminal truncation. Left panel, Coomassie stain of proteins in the reaction, Right panel, western analysis with H3K9 methylation detected using the indicated antibodies. SETD5 constructs were detected with anti-Flag.

(H) SETD5 co-purifies with the NCoR1-HDAC3 complex and G9a. Silver stain of SETD5<sub>com</sub> after first and second purification steps. The identity of associated proteins as indicated on the right was determined by mass spectrometry. See also Table S3.

(I) SETD5 interacts with the NCoR1-HDAC3 complex, G9a, and GLP in 293T cells. Co-immunoprecipitation (coIP) experiments in 293T cells expressing Flag-SETD5 and using the indicated antibodies for the IPs (anti-Flag for SETD5) and western analyses. Input, nuclear extract.

(J) CoIP experiments as in (I) with Flag-tagged wild-type SETD5 or the indicated derivatives as in (G). Input, 293T nuclear extract.

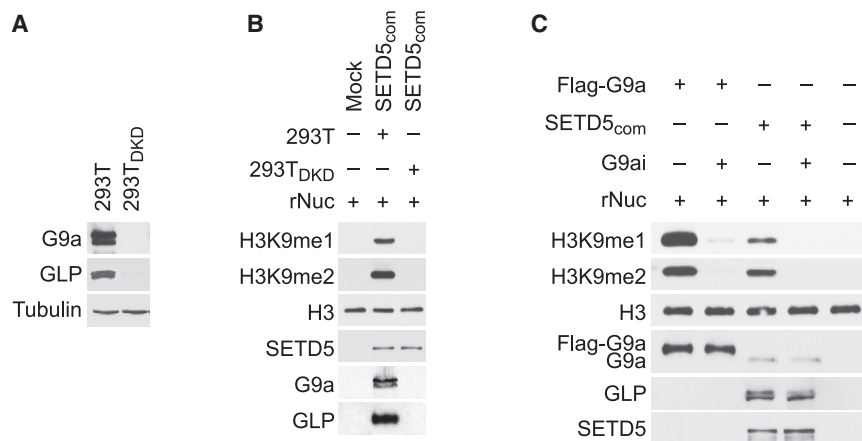


**Figure 4. G9a/GLP Mediate SETD5<sub>com</sub> Methylation Activity**

(A) Generation of G9a/GLP-depleted 293T cells. Western analysis with the indicated antibodies of control (293T) or G9a/GLP co-depleted 293T cell lysates (293T<sub>DKD</sub>). Tubulin is shown as a loading control.

(B) Methylation of H3K9 by SETD5<sub>com</sub> requires G9a and GLP. Western analysis with the indicated antibodies of *in vitro* methylation assay as in Figure 3D using SETD5<sub>com</sub> purified from 293T or 293T<sub>DKD</sub> cells.

(C) Methylation of H3K9 by SETD5<sub>com</sub> is inhibited by the G9a/GLP inhibitor (UNC0638, G9ai). Western analysis with the indicated antibodies of *in vitro* methylation assay on recombinant nucleosomes with G9a and SETD5<sub>com</sub> ± UNC0638 (2 μM).

cells in which G9a and GLP were co-depleted (293T<sub>DKD</sub>; Figure 4A). As expected, SETD5<sub>com</sub> purified from control cells methylated H3K9; however, SETD5<sub>com</sub> purified from 293T<sub>DKD</sub> cells does not methylate H3K9 (Figure 4B). Furthermore, *in vitro* methylation assays in the presence of the selective G9a/GLP inhibitory compound UNC0638 (Vedadi et al., 2011) abrogated the activity of the positive control full-length G9a and of SETD5<sub>com</sub> (Figure 4C). Together, these data suggest that H3K9 methylation by SETD5<sub>com</sub> is mediated by the KMTs G9a/GLP.

The association of SETD5 with the NCoR1-HDAC3 co-repressor complex suggests a model in which SETD5 coordinates placement of repressive methylation at H3K9me by G9a/GLP with removal of activating histone acetylation marks by HDAC3. To test this hypothesis, deacetylase assays using SETD5<sub>com</sub> from control or HDAC3-depleted cells (Figure 5A) was performed on HeLa-purified nucleosomes, which contain a large array of existing histone modifications. As shown in Figure 5B, H3K9 acetylation (H3K9ac) was removed by SETD5<sub>com</sub> in an HDAC3-dependent manner. Moreover, the selective HDAC3 inhibitor RGFP966 (Xu et al., 2009) blocks H3K9ac deacetylation by SETD5<sub>com</sub>, whereas the HDAC8 inhibitor PCI-34051 does not (Balasubramanian et al., 2008) (Figure 5C). In contrast to H3K9ac, SETD5<sub>com</sub> does not deacetylate the reported HDAC3 substrates H4K5ac and H4K8ac (Figures 5B and 5C) (Vermeulen et al., 2004). To the best of our knowledge, the selectivity of HDAC3 on histones has not been comprehensively characterized. Therefore, we assembled an active recombinant HDAC3 complex (rHDAC3 and the DAD domain of NCoR1 [Guenther et al., 2001] [Figure 5D]) and performed *in vitro* deacetylation assays on HeLa-purified nucleosomes. The HDAC3 complex deacetylated a broad range of lysine-acetylated substrates on nucleosomes, including the published substrates H4K5ac and H4K8ac (Figure 5E). The difference in deacetylation activity on HeLa nucleosomes between SETD5<sub>com</sub> and rHDAC suggest that SETD5<sub>com</sub> imposes substrate selectivity upon HDAC3. To test this, a side-by-side comparison of SETD5<sub>com</sub> and rHDAC3 complex deacetylation activity was performed on a library of recombinant nucleosomes designed to harbor a single acetylation modification on 1 of 11 different lysine residues known to be modified on H3 and H4. In this system, the rHDAC3 complex deacetylated all of the lysine-acetylated nucleosomes besides

H3K36ac, whereas SETD5<sub>com</sub> only deacetylated H3K9ac and H3K27ac (Figures 5F–5H and S4A–S4I). Thus, the *in vitro* catalytic activity of HDAC3, in the context of the SETD5 complex, is restricted to acetylated H3K9 and H3K27, two residues that when methylated are markers of silenced chromatin (Husmann and Gozani, 2019).

### The SETD5 Complex Regulates H3K9 Modification and MEKi Resistance in PDAC Cells

SETD5 expression increases in cells and tumors upon the development of resistance to MEKi (see Figures 1G and S2D–S2H). The levels of SETD5 protein are also higher in KPC<sub>R</sub> cells (derived from trametinib-resistant murine PDAC tumors) compared with KPC<sub>N</sub> cells (derived from naive murine PDAC tumors) (Figure 6A). In contrast, the levels of SETD5-associated proteins, such as HDAC3 and G9a are equivalent in KPC<sub>N</sub> and KPC<sub>R</sub> lysates (Figure 6A). Like in 293T cells (see Figure 3), SETD5 interacts with the NCoR1-HDAC3 complex and G9a in KPC<sub>R</sub> cells (Figure 6B; we were unable to identify an antibody that reliably detected murine GLP). In addition, analysis of KPC<sub>R</sub> cell lysates by size-exclusion chromatography identified co-enrichment of SETD5, the NCoR1-HDAC3 complex, and G9a within the same high-molecular-weight fractions (Figure S5A). These data suggest that the rate-limiting component in the assembly of SETD5<sub>com</sub> is SETD5, whose expression increases in MEKi-resistant cells and tumors.

While SETD5 knockdown has no impact on proliferation of KPC<sub>N</sub> cells in culture (Figure 6C), depletion of SETD5 in KPC<sub>R</sub> cells inhibits proliferation (Figure 6D). In these cells, bulk levels of H3K9me2, H3K9ac, and H3K27ac are not affected by SETD5 knockdown (Figure 6E), suggesting that potential SETD5-dependent regulation of chromatin modifications is localized rather than general. Notably, no change in H3K36me3 levels was observed upon SETD5 depletion in KPC<sub>R</sub> cells (Figure 6E) or in several other cell types, including the ones used in (Sessa et al., 2019) (Figures S5B–S5E); whereas knockdown of SETD2, the only validated mammalian H3K36me3 KMT, does deplete H3K36me3 (Figures S5C–S5E; see Discussion). Finally, the RAS-pathway factor SHOC2 is a major regulator of PDAC cell sensitivity to MEKi (Sulahian et al., 2019) and depletion of SHOC2 sensitized KPC<sub>N</sub> cells to even low dose

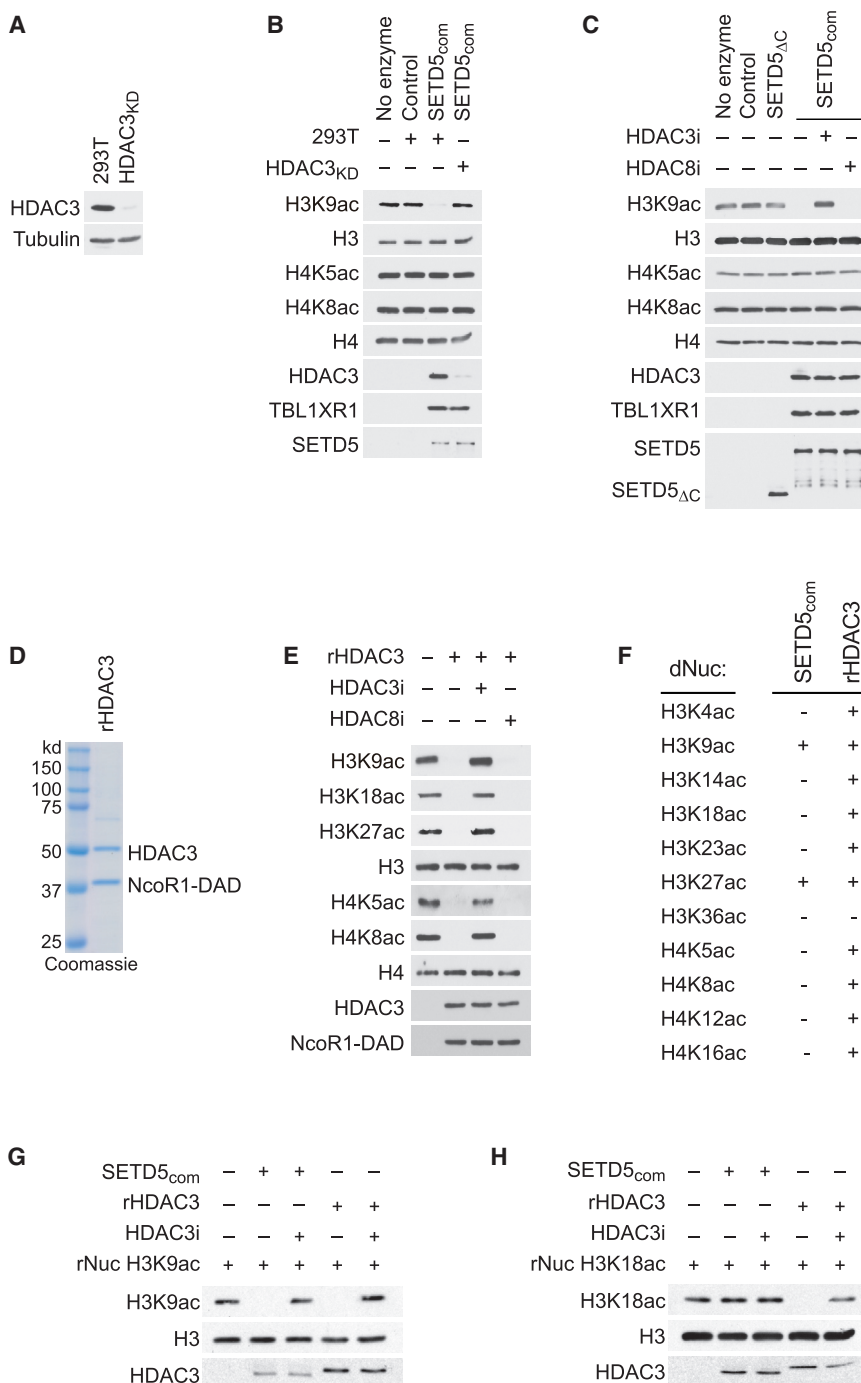


**Figure 5. HDAC3-Selective Deacetylation of H3K9Ac by SETD5<sub>com</sub>**

(A) Generation of HDAC3-depleted 293T cells. Western analysis with the indicated antibodies of control (293T) or HDAC3-depleted 293T cell lysates (HDAC3<sub>KD</sub>). Tubulin is shown as a loading control.

(B) SETD5<sub>com</sub> possess HDAC3-dependent lysine deacetylation activity. Western analysis with the indicated antibodies of *in vitro* histone deacetylation assay on HeLa-purified nucleosomes using SETD5<sub>com</sub> purified from 293T or HDAC3<sub>KD</sub> cells.

(C) HDAC3-dependent SETD5<sub>com</sub> lysine deacetylation activity is inhibited by a selective HDAC3 inhibitor. *In vitro* deacetylation assays as in (B) ± the selective HDAC3 inhibitor (RGF9966, 1 μM) or ± the selective HDAC8 inhibitor (PCI-34051, 1.5 μM). SETD5<sub>ΔC</sub> does not interact with HDAC3 (see Figure 3J) and serves as a negative control.

(D) Coomassie stain of active recombinant HDAC3 complex (contains HDAC3 and the DAD domain of NCoR1, labeled as rHDAC3) purified from *E. coli*.

(E) HDAC3 has broad deacetylation activity on histones. *In vitro* histone deacetylation assay on HeLa-purified nucleosomes with rHDAC3 complex analyzed by western blots with the indicated antibodies.

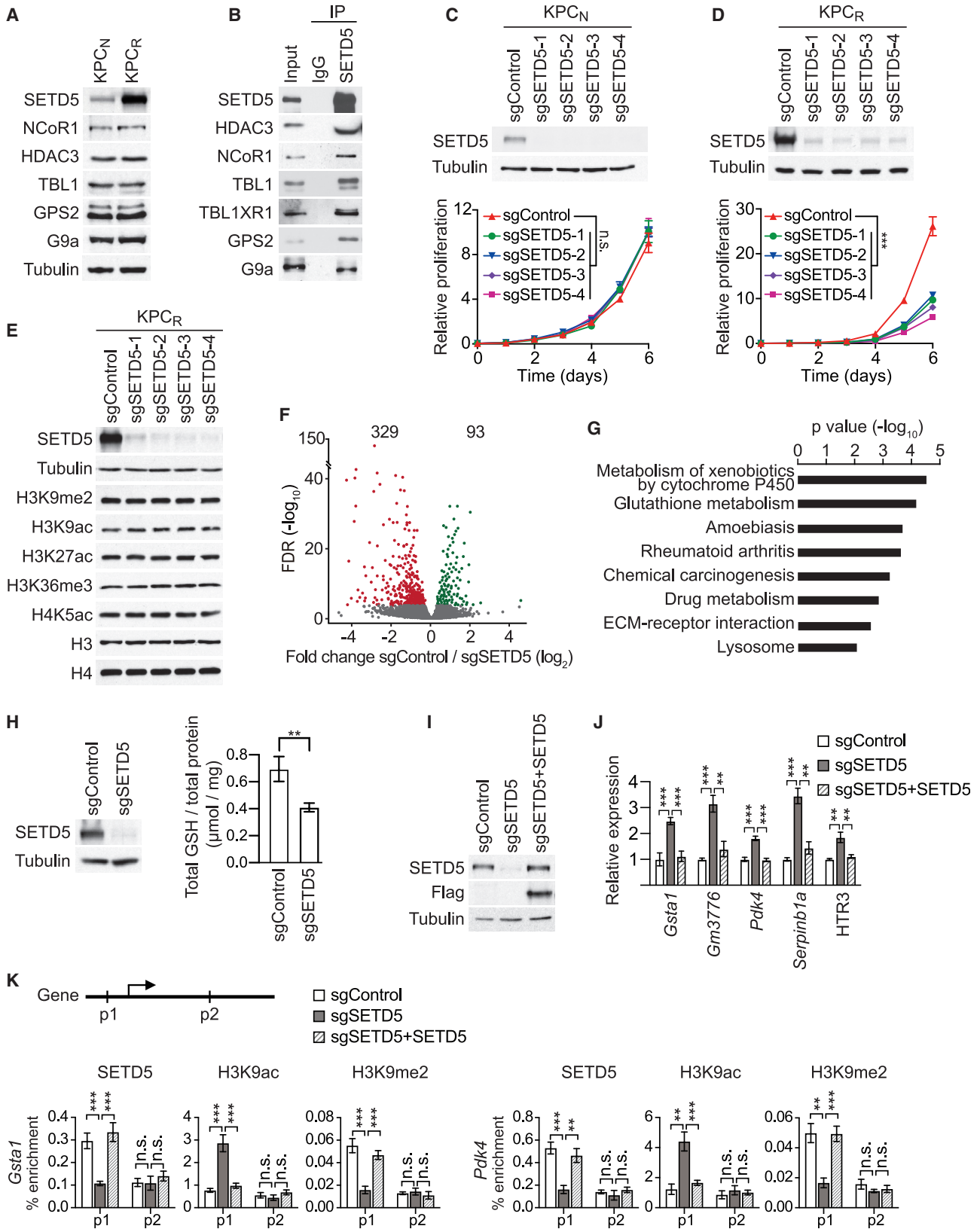
(F–H) HDAC3 selectively deacetylates H3K9Ac and H3K27Ac in the context of SETD5<sub>com</sub>. (F) Summary of deacetylation assays using SETD5<sub>com</sub> or rHDAC3 on a library of recombinant nucleosomes designed to harbor a single lysine acetylation as indicated. (G and H) Western analysis with the indicated antibodies of deacetylation assays on H3K9Ac rNuc (G) and H3K18Ac rNuc (H). Figure S4 shows the other nine modified nucleosomes summarized in (F).

chromosome P450 pathway and glutathione [GSH] metabolism) that confer drug resistance in cancer (Figure 6G; see below) (Bansal and Simon, 2018; Noll et al., 2016). For example, several genes in multiple top functional pathways are enzymes that metabolize GSH (Figures 6G and S6A). While GSH initially plays a role in preventing cancer development, elevation of GSH levels is a mechanism used by many malignancies to promote chemotherapy resistance (Bansal and Simon, 2018). In this context, depletion of SETD5 in KPC<sub>R</sub> cells decreases total

MEKi, but unlike SETD5, SHOC2 loss had no effect on KPC<sub>R</sub> viability (Figures S5F–S5H).

Comparison of the transcriptomes of KPC<sub>R</sub> cells grown in the presence of trametinib ± SETD5 show that SETD5 loss is associated with gene repression, with SETD5 knockdown increasing expression of 329 genes and decreasing expression of 93 genes (Figure 6F). These data are consistent with SETD5 being associated with a co-repressor complex and two canonical repressive histone-modifying activities. KEGG pathway analysis of the de-repressed genes identified key functional pathways (e.g., cyto-

cellular GSH levels (Figure 6H). Notably, treatment of the KPC<sub>R</sub>-SETD5 knockdown cells with N-acetylcysteine, which counteracts GSH depletion, partially rescues the inhibition of proliferation caused by SETD5 loss (Figures S6B and S6C). Also present in the de-repressed gene group is *Pdk4* (Figure S6A and Table S3); pyruvate dehydrogenase kinase 4 (PDK4) inhibits entry into the TCA cycle to oppose resistance to RAS-pathway signaling ablation in PDAC and targeted therapy in EGFR mutant lung cancer (Sun et al., 2014; Viale et al., 2014). The regulation of many key SETD5 target genes (e.g., *GSTT1* [GSH-metabolizing



(legend on next page)

enzyme], *PDK4*, and others) was observed in independent SETD5 knockdown cell lines (Figure S6A). Moreover, complementation of KPC<sub>R</sub>-SETD5 knockdown cells with sgRNA-resistant SETD5 restores repression of several genes (Figures 6I and 6J). These data suggest that SETD5 directly regulates an MEKi-resistance gene expression program in PDAC cells.

Next, chromatin immunoprecipitation assays were performed to test whether the SETD5-regulated genes are direct targets of SETD5<sub>com</sub>. SETD5 occupancy at the promoter of the target genes (*GSTA1*, *PKD4*, and *GM3776*) is eliminated in SETD5 knockdown cells, whereas SETD5 signaling within the coding sequence of these genes showed low signal irrespective of SETD5 expression (Figures 6K and S6B). Consistent with these results, at target gene promoters, H3K9ac levels increase and H3K9me2 levels decrease upon SETD5 knockdown, and this SETD5-dependent acetyl-methyl switch at H3K9 is not observed within the coding region (Figures 6K and S6B). Finally, adding back SETD5 reconstituted the repressive chromatin environment at target gene promoters (Figures 6K and S6B). Together, these data suggest a model in which SETD5—via coordinated deacetylation and methylation of H3K9 at chromatin targets—orchestrates a transcriptional repression program to promote PDAC resistance to MEKi.

### Small-Molecule Inhibitors of G9a and HDAC3 Re-sensitize Resistant PDAC to Trametinib Therapy

Our model predicts that blocking SETD5's associated histone-modifying activities could functionally mirror SETD5 knockdown and render refractory PDAC re-sensitized to MEKi. To test this idea, KPC<sub>R</sub> cells were treated with different combinations of trametinib with the selective inhibitors of G9a/GLP (UNC0638) and

HDAC3 (RGFP966) (Vedadi et al., 2011; Xu et al., 2009). The combination of all three drugs (hereto referred to as Triple<sup>Tx</sup>) significantly inhibited KPC<sub>R</sub> cell proliferation, whereas trametinib/UNC0638 or trametinib/RGFP966 had only a modest impact compared with trametinib alone (Figures 7A and S7A). Transcriptome profiling comparing KPC<sub>R</sub> cells treated with Triple<sup>Tx</sup> versus trametinib alone showed that Triple<sup>Tx</sup> increased expression of 452 genes and decreased expression of 320 genes (Figure S6C). Functional analysis of the upregulated genes included pathways similar to those seen with SETD5 depletion, including cytochrome P450 and glutathione metabolism pathways and individual genes, such as *Pdk4* (Figures S6D and S6E). Indeed, there was highly significant overlap in the upregulated gene sets elicited by Triple<sup>Tx</sup> and sgSETD5/MEKi conditions (Figure 7B; overlap of negatively regulated genes was limited and less significant, Figure S6F). KEGG analysis of the shared upregulated gene set showed enrichment in the same functional pathways as observed with the individual upregulated gene sets (Figure 7C, compare with Figures 6G and S6D). Gene set enrichment analysis of the de-repressed genes under both conditions (sgSETD5/MEKi and Triple<sup>Tx</sup>) showed strong overlap with several categories implicated in drug resistance (e.g., OXPPOS-related processes and glutathione metabolism), cancer cell phenotypes (e.g., apoptosis), and chromatin-silencing in pancreatic cancer (Figures 7D and S6G). These data suggest that the chromatin landscape at SETD5-target genes is regulated in a similar fashion by G9a/HDAC3 inhibition as with SETD5 depletion. Indeed, while Triple<sup>Tx</sup> had no impact on SETD5 chromatin occupancy at the promoters of *GSTA1* and *PDK4* genes, the treatment increased H3K9ac signal and decreased H3K9me2 signal (Figure 7E). Thus, the combined

### Figure 6. SETD5 Coordinates a Targeted Therapy Resistance Program in PDAC Cells

(A) Increased levels of SETD5 but not associated proteins in MEKi-resistant PDAC cells. Western analysis with the indicated antibodies of WCEs from KPC<sub>N</sub> cells (derived from naive murine PDAC) and KPC<sub>R</sub> cells (derived from trametinib-resistant murine PDAC).

(B) SETD5<sub>com</sub> interactions occur in KPC<sub>R</sub> cells. IPs of endogenous SETD5 complex (or IgG control) from nuclear extracts of KPC<sub>R</sub> followed by western analysis with the indicated antibodies. Input, nuclear extract.

(C and D) SETD5 depletion inhibits proliferation of KPC<sub>R</sub> cells but has no impact on KPC<sub>N</sub> cells. Western analysis (top panel) and proliferation assays (bottom panel) in KPC<sub>N</sub> (C) and KPC<sub>R</sub> (D) cell lines depleted for SETD5 with four independent sgRNAs (sgSETD51-4) or control (sgControl). KPC<sub>R</sub> cells are cultured in the presence of 0.2 μM trametinib. Error bars represent mean ± SD from three independent experiments. \*\*\*p < 0.001; n.s., not significant, two-tailed unpaired Student's t test.

(E) SETD5 depletion does not cause bulk chromatin modification changes. Western analysis of cells in (D) with the indicated antibodies.

(F) SETD5 is a transcriptional repressor. Volcano plot of RNA-seq comparison between KPC<sub>R</sub> cells grown in the presence of trametinib ± SETD5 (three biological replicates for each condition). SETD5 depletion caused increasing expression of 329 genes shown in red (fold change log<sub>2</sub> ≤ -0.5 and p < 0.05 by Wald test) and decreasing expression of 93 genes shown in green (fold change log<sub>2</sub> ≥ 0.5 and p < 0.05 by Wald test). False discovery rate (FDR) values are provided (detailed description in the STAR Methods).

(G) KEGG analysis of SETD5-repressed genes. The most significantly enriched KEGG terms associated with the 329 genes upregulated by SETD5 ablation in KPC<sub>R</sub> cancer cells are shown.

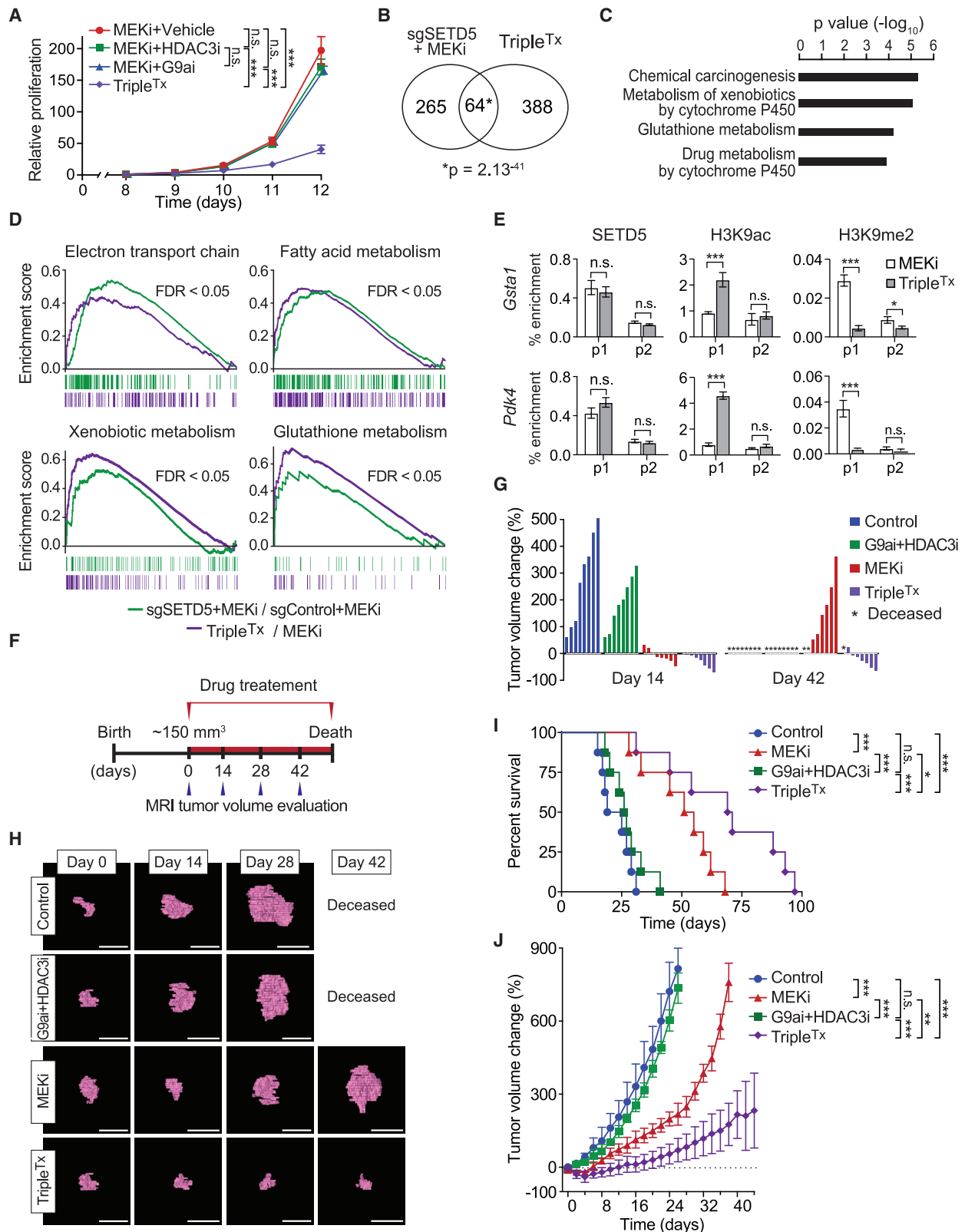
(H) Decreased total cellular glutathione (GSH) levels in SETD5 knockdown cells. Analysis of total cellular GSH levels in KPC<sub>R</sub> cells ± SETD5. Left panel, western analysis of WCE with indicated antibodies. Right panel, total GSH levels (see the STAR Methods). Error bars represent mean ± SD from three independent experiments, \*\*p < 0.01 by two-tailed unpaired Student's t test.

(I) Reconstitution of SETD5 knockdown cells with CRISPR-resistant SETD5. Western analysis of KPC<sub>R</sub> WCEs ± SETD5 and complemented with CRISPR-resistant SETD5.

(J) Reconstitution of SETD5-mediated target gene repression. Real-time qPCR analysis of the indicated mRNAs from cells in (I). Real-time qPCR data were normalized to *Actb* and are presented as fold change relative to the control. Error bars represent mean ± SD from three independent experiments. \*\*p < 0.01, \*\*\*p < 0.001 by two-tailed unpaired Student's t test.

(K) SETD5 directly regulates promoter chromatin of target genes. Top panel, schematic of general gene structure and site of primers used to study the *GSTA1* (left panel) and *PDK4* (right panel) gene loci. Real-time qPCR of chromatin immunoprecipitation (ChIP-qPCR) analysis of SETD5, H3K9ac, and H3K9me2 occupancy at the promoter (p1) and gene body (p2) of the *Gsta1* and *Pdk4* loci in control (sgControl), SETD5-deficient (sgSETD5) or reconstituted (sgSETD5 + SETD5) KPC<sub>R</sub> cells. The data are plotted as percent enrichment relative to input. Error bars represent mean ± SEM from three independent experiments, \*\*p < 0.01, \*\*\*p < 0.001; n.s., not significant, by two-tailed unpaired Student's t test.

See also Figure S6B.



(legend on next page)

action of selective G9a and HDAC3 inhibition may functionally phenocopy SETD5 depletion with respect to mitigating reprogramming of PDAC into a MEKi-resistant state.

The therapeutic efficacy on PDAC *in vivo* of Triple<sup>Tx</sup> was tested in the *Kras;p53* mouse model (Bardeesy et al., 2006). Treatment was initiated in tumors of ~150 mm<sup>3</sup> in size as ascertained by MRI and then biweekly tumor growth and survival was monitored (Figures 7F and S7B–S7E). Four treatment arms were used: (1) vehicle control, (2) G9a/HDAC3 inhibition, (3) trametinib, and (4) Triple<sup>Tx</sup>. At 2 weeks, G9a/HDAC3 inhibition modestly attenuated tumor growth compared with the vehicle control, whereas trametinib alone and triple therapy halted tumor growth or caused tumor regression (Figures 7G and 7H). By 6 weeks, all of the mice in the control and G9a/HDAC3 inhibition treatment arms were deceased (Figures 7G–7I). Tumors in the trametinib alone treatment arm showed significant growth by 6 weeks, indicating drug resistance emergence (Figures 7G–7I). In contrast, tumors in the Triple<sup>Tx</sup> regimen were smaller than when treatment was initiated (Figures 7G and 7H). Consistent with this, Triple<sup>Tx</sup> nearly tripled lifespan relative to the control group, with reduced tumor burden even at death (Figure 7I). Thus, combining drugs that inhibit G9a/GLP, HDAC3, and MEK1/2 results in a sustained potent antitumor response in an aggressive model of PDAC in mice.

To investigate the efficacy of the triple therapy in human pancreatic cancer, PDX studies using two independent primary PDAC patient samples were performed (Figures 7J and S7F). Once the xenograft tumors reached a volume of 200 mm<sup>3</sup>, treatment with the same four arms as above commenced and growth monitored until humane euthanasia was required. G9a/HDAC3 inhibition was not therapeutically effective with either PDX sample (Figures 7J and S7F). With trametinib treatment, tumors are initially sensitive but over time became resistant (Figures 7J and S7F). In contrast, Triple<sup>Tx</sup> significantly slowed tumor progression for the full duration of the treatment protocol, well after

the other treatment conditions had failed (Figures 7J and S7F). Taken together, these data suggest that inhibition of G9a and HDAC3 with small-molecule drugs renders PDAC tumors vulnerable to MEK inhibition, potentially due to blockade of an SETD5-orchestrated epigenetic resistance program.

## DISCUSSION

Here, we identify SETD5 as a chromatin-based master regulator of adaptive targeted therapy resistance in pancreatic cancer (Figure S7H). SETD5 belongs to the SET domain family of proteins, a family that contains many bona fide histone lysine methyltransferases (Husmann and Gozani, 2019). However, there are also many SET proteins with divergent catalytic activities (e.g., histidine methylation [Wilkinson et al., 2019]) or several that are not active enzymes (Husmann and Gozani, 2019). Here, we investigated SETD5 methylation activity *in vitro* on histone and nucleosomal substrates and failed to detect any intrinsic activity (Figures 3A–3C and S3B–S3F). These findings are consistent with previous studies in which SETD5 deletion in cells or in mice did not cause bulk histone lysine methylation changes (DeLiu et al., 2018; Mas et al., 2016; Osipovich et al., 2016). In contrast, Sessa et al. (2019) recently classified SETD5 as a robust H3K36 trimethylase in multiple contexts, and concluded that SETD5, not SETD2, is the main physiologic H3K36me3-generating enzyme in neuronal stem cells (NSCs) (see Figure 8E in Sessa et al., 2019). In our study, we failed to reproduce any of the reported key results on H3K36me3 from (Sessa et al., 2019), whereas our positive controls (i.e., SETD2) behaved as expected (Figures 3B and S3B–S3F). For example, SETD5 loss in NSCs did not alter H3K36 methylation (Figure S5E); in contrast, SETD2 knockdown did (Figure S5E). Thus, the preponderance of evidence does not support a role for SETD5 in the direct regulation of H3K36 methylation—in cancer or in an intellectual disability/neuronal development context.

### Figure 7. Pharmacological Blockade of G9a and HDAC3 Sustains Trametinib Therapy Inhibition of PDAC Tumor Growth

- (A) Combination pharmacologic blockade of MEK, G9a, and HDAC3 inhibits proliferation of MEKi-resistant PDAC cells. Proliferation assay in KPC<sub>R</sub> cells treated with MEKi (0.2 μM), MEKi (0.2 μM) + G9ai (0.6 μM), MEKi (0.2 μM) + HDAC3i (0.6 μM), or MEKi + G9ai (0.6 μM) + HDAC3i (0.6 μM) (Triple<sup>Tx</sup>). Error bars represent mean ± SD from three independent experiments. \*\*\*p < 0.001; n.s., not significant, by two-tailed unpaired Student's t test.
- (B) Significant overlap in the transcriptional changes triggered by SETD5 depletion and inhibition of G9a and HDAC3. Venn diagram showing the overlap of de-repressed gene sets from SETD5 depletion (see Figure 6F) and Triple<sup>Tx</sup>-treated KPC<sub>R</sub> cells. p value by hypergeometric test.
- (C) KEGG analysis of overlapping gene set in (B). The most significantly enriched KEGG terms associated with the genes de-repressed by SETD5 depletion and Triple<sup>Tx</sup> treatment in MEKi-resistant KPC<sub>R</sub> cancer cells are shown.
- (D) Gene set enrichment analysis analysis of RNA-seq data of MEKi-treated SETD5 knockdown (sgSETD5) versus control (sgControl) and Triple<sup>Tx</sup>-treated versus control (MEKi-treated) KPC<sub>R</sub> cells. FDR values are provided (detailed description in the STAR Methods).
- (E) ChIP-qPCR analysis as in Figure 6K of SETD5, H3K9ac, and H3K9me2 at the promoter or gene body of *Gsta1* and *Pdk4* (*p1* and *p2*) in Triple<sup>Tx</sup>- or MEKi-treated KPC<sub>R</sub> cells. The data are plotted as percent enrichment relative to input. Error bars represent mean ± SEM from three independent experiments, \*p < 0.05, \*\*\*p < 0.001; n.s., not significant, by two-tailed unpaired Student's t test.
- (F) Treatment schedule for administration of MEKi, G9ai + HDACi, MEKi + G9ai + HDACi combination (Triple<sup>Tx</sup>), or vehicle (control) via intraperitoneal injection once per day to *Kras;p53* mutant mice. Animals undergoing monotherapy also received placebo (vehicle) so that all arms of the trial received equal volume injections.
- (G) Waterfall plot of individual pancreatic tumor volume dynamics after 14 and 42 days of treatment. Note that a fraction of animals in the MEKi and in the G9ai + HDAC3i treatment arms presented with morbidity, necessitating euthanasia.
- (H) Representative MRI scan to analyze tumor volume in *Kras;p53* mutant mice treated with G9A, HDAC3, and MEK inhibitors. Scale bars, 1 cm.
- (I) Kaplan-Meier survival curves of *Kras;p53* mutant mice from enrollment time in control (vehicle) (n = 8, median survival = 22 days), G9ai + HDAC3i (n = 9, median survival = 26 days), MEKi (n = 8 median survival = 51 days), and Triple<sup>Tx</sup> (n = 8, median survival = 73 days) treatment groups. \*p < 0.05, \*\*\*p < 0.001; n.s., not significant, by log rank test for significance.
- (J) Tumor volume quantification of patient-derived PDAC xenografts in mice (n = 8 mice, for each treatment group). Mice undergoing monotherapy also received vehicle. \*p < 0.033, \*\*p < 0.002, \*\*\*p < 0.0001 by two-way ANOVA with Tukey's testing for multiple comparisons. Data are represented as mean ± SEM. See also Figure S7.

We also found that while HDAC3 normally deacetylates a broad spectrum of histone acetyl-lysine substrates, when partnered with SETD5, HDAC3 is converted from a relatively promiscuous enzyme into a selective one (Figure 5F). This suggests a model in which the SETD5-HDAC3-G9a co-repressor complex couples selective deacetylation of H3K9ac with methylation of this residue at target genes, such as *Pdk4*, the repression of which promotes tumor drug resistance. The mechanism proposed here of an H3K9 acetyl-methyl switch for gene expression regulation is established for other silencing activities, such as the CtBP co-repressor complex (Shi et al., 2003). HDAC3 also has activity on H3K27ac-nucleosomes, suggesting that the SETD5 complex may also regulate drug resistance programming by targeting chromatin modifications at enhancer regions.

PDAC is virtually always driven by oncogenic mutant KRAS. Thus, clinically actionable strategies that can restore the therapeutic efficacy of downstream KRAS pathway inhibitors have the potential to have considerable impact upon the treatment of PDAC (Sun et al., 2017). In our study we used selective inhibitors of G9a and HDAC3 to mirror SETD5 depletion in sustaining the therapeutic benefit of MEKi in different PDAC models. While less selective HDAC3 inhibitors are in various stages of clinical trials for a variety of indications, at present, an HDAC3-specific inhibitor, such as RGFP966 has not been evaluated for safety in patients. Similarly, tolerance for G9a/GLP inhibitors are yet to be tested in patients. In our pre-clinical experiments, the combination of RGFP966 and UNC0642 did not have any adverse effects, with no toxicity in mice, and indeed in the PDX model the treatment largely alleviated the onset of cachexia, an important co-morbidity that contributes to PDAC mortality (Figure S7G). These findings suggest that pharmacologic blockage of SETD5-associated activities has the potential of being translatable into a clinical setting. In summary, our study identifies a chromatin-based mechanism mediated by SETD5 in the establishment of PDAC resistance to FDA-approved medicines that target the MAPK pathway.

## STAR★METHODS

Detailed methods are provided in the online version of this paper and include the following:

- KEY RESOURCES TABLE
- RESOURCE AVAILABILITY
  - Lead Contact
  - Materials Availability
  - Data and Code Availability
- EXPERIMENTAL MODEL AND SUBJECT DETAILS
  - Mice
  - Cell Lines and Primary Cell Cultures
  - Patient-Derived Cancer Xenografts and Mouse Allografts
- METHOD DETAILS
  - Pancreatic Cancer Mouse Models
  - Magnetic Resonance imaging
  - Histology and Immunohistochemistry
  - Meta-Analysis of Gene Expression
  - Transfection and Viral Transduction
  - Plasmids

- Pooled shRNA Screen
- Immunoblot Analysis and Immunoprecipitation
- Generation of SETD5 Antibody
- Expression and Purification of Recombinant Proteins
- ProtoArray, Methylation and Deacetylation Assays
- Gel Filtration
- Mass Spectrometry
- Quantitative RT-PCR
- RNA-Sequencing and Data Analysis
- Chromatin Immunoprecipitation (ChIP)
- GSH Assay
- Cell Assays
- siRNA Transfection

## ● QUANTIFICATION AND STATISTICAL ANALYSIS

### SUPPLEMENTAL INFORMATION

Supplemental Information can be found online at <https://doi.org/10.1016/j.ccell.2020.04.014>.

### ACKNOWLEDGMENTS

We thank members of the Gozani and Mazur laboratories for critical reading of the manuscript. This work was supported in part by grants from the NIH to P.K.M. and O.G. (CA236949), M.C.B. (1DP2HD084069), M.J.M., M.A.C., S.A.H. and M.C.K. (2R44GM116584). J.S. and O.G. from the Lustgarten Foundation. A.M. by the MD Anderson Moonshot Program. P.K.M. by the Neuroendocrine Tumor Research Foundation, AACR, Lung Cancer Research Foundation, American Gastroenterological Association Research Foundation, DOD PRCRP Career Development Award (W81XWH1910761), University Cancer Foundation at MD Anderson Cancer Center, a CPRIT Scholar in Cancer Research (RR160078), and the Andrew Sabin Family Foundation Scholar. S.H. by a Deutsche Forschungsgemeinschaft Fellowship.

### AUTHOR CONTRIBUTIONS

Z.W. and S.H. contributed equally to this work. They were responsible for the experimental design, execution, data analysis, and manuscript preparation. Z.W., T.-M.L., and L.Z. performed mass spectrometry and J.E.E. provided instrument access. Z.Y. assisted Z.W. with NSCs. M.E.F. and N.M.F. assisted S.A.H. M.C. contributed to MRI analysis. S.M.L. performed bioinformatic meta-analyses. R.L. performed RNA-seq analysis. H.W. performed pathological analyses. A.M. and M.P.K. provided PDX samples. M.J.M., M.A.C., S.A.H., and M.-C.K. provided nucleosomes. M.C.B. helped with the shRNA screen. J.S. contributed to experimental design. O.G. and P.K.M. were equally responsible for supervision of research, data interpretation, and manuscript preparation.

### DECLARATIONS OF INTERESTS

O.G. is a co-founder of EpiCyphe and Athelas Therapeutics. M.C.K., M.J.M., M.A.C., and S.A.H. are employees and shareholders of EpiCyphe.

Received: December 30, 2019

Revised: March 11, 2020

Accepted: April 22, 2020

Published: May 21, 2020

### REFERENCES

- Almoguera, C., Shibata, D., Forrester, K., Martin, J., Arnheim, N., and Perucho, M. (1988). Most human carcinomas of the exocrine pancreas contain mutant c-K-ras genes. *Cell* 53, 549–554.
- Bailey, P., Chang, D.K., Nones, K., Johns, A.L., Patch, A.M., Gingras, M.C., Miller, D.K., Christ, A.N., Bruxner, T.J., Quinn, M.C., et al. (2016). Genomic analyses identify molecular subtypes of pancreatic cancer. *Nature* 531, 47–52.

- Balasubramanian, S., Ramos, J., Luo, W., Sirisawad, M., Verner, E., and Buggy, J.J. (2008). A novel histone deacetylase 8 (HDAC8)-specific inhibitor PCI-34051 induces apoptosis in T-cell lymphomas. *Leukemia* 22, 1026–1034.
- Banerji, U., Camidge, D.R., Verheul, H.M., Agarwal, R., Sarker, D., Kaye, S.B., Desai, I.M., Timmer-Bonte, J.N., Eckhardt, S.G., Lewis, K.D., et al. (2010). The first-in-human study of the hydrogen sulfate (Hyd-sulfate) capsule of the MEK1/2 inhibitor AZD6244 (ARRY-142886): a phase I open-label multicenter trial in patients with advanced cancer. *Clin. Cancer Res.* 16, 1613–1623.
- Bansal, A., and Simon, M.C. (2018). Glutathione metabolism in cancer progression and treatment resistance. *J. Cell Biol.* 217, 2291–2298.
- Bardeesy, N., Aguirre, A.J., Chu, G.C., Cheng, K.H., Lopez, L.V., Hezel, A.F., Feng, B., Brennan, C., Weissleder, R., Mahmood, U., et al. (2006). Both p16(Ink4a) and the p19(Arf)-p53 pathway constrain progression of pancreatic adenocarcinoma in the mouse. *Proc. Natl. Acad. Sci. U S A* 103, 5947–5952.
- Bassik, M.C., Kampmann, M., Lebbink, R.J., Wang, S., Hein, M.Y., Poser, I., Weibezahn, J., Horlbeck, M.A., Chen, S., Mann, M., et al. (2013). A systematic mammalian genetic interaction map reveals pathways underlying ricin susceptibility. *Cell* 152, 909–922.
- Bassik, M.C., Lebbink, R.J., Churchman, L.S., Ingolia, N.T., Patena, W., LeProust, E.M., Schuldiner, M., Weissman, J.S., and McManus, M.T. (2009). Rapid creation and quantitative monitoring of high coverage shRNA libraries. *Nat. Methods* 6, 443–445.
- Bodoky, G., Timcheva, C., Spigel, D.R., La Stella, P.J., Ciuleanu, T.E., Pover, G., and Tebbutt, N.C. (2012). A phase II open-label randomized study to assess the efficacy and safety of selumetinib (AZD6244 [ARRY-142886]) versus capecitabine in patients with advanced or metastatic pancreatic cancer who have failed first-line gemcitabine therapy. *Invest. New Drugs* 30, 1216–1223.
- Bryant, K.L., Stalneck, C.A., Zeitouni, D., Klomp, J.E., Peng, S., Tikunov, A.P., Gunda, V., Pierobon, M., Waters, A.M., George, S.D., et al. (2019). Combination of ERK and autophagy inhibition as a treatment approach for pancreatic cancer. *Nat. Med.* 25, 628–640.
- Canon, J., Rex, K., Saiki, A.Y., Mohr, C., Cooke, K., Bagal, D., Gaida, K., Holt, T., Knutson, C.G., Koppada, N., et al. (2019). The clinical KRAS(G12C) inhibitor AMG 510 drives anti-tumour immunity. *Nature* 575, 217–223.
- Chung, V., McDonough, S., Philip, P.A., Cardin, D., Wang-Gillam, A., Hui, L., Tejani, M.A., Seery, T.E., Dy, I.A., Al Baghdadi, T., et al. (2017). Effect of selumetinib and MK-2206 vs oxaliplatin and fluorouracil in patients with metastatic pancreatic cancer after prior therapy: SWOG S1115 study randomized clinical trial. *JAMA Oncol.* 3, 516–522.
- Collisson, E.A., Trejo, C.L., Silva, J.M., Gu, S., Korkola, J.E., Heiser, L.M., Charles, R.P., Rabinovich, B.A., Hann, B., Dankort, D., et al. (2012). A central role for RAF→MEK→ERK signaling in the genesis of pancreatic ductal adenocarcinoma. *Cancer Discov.* 2, 685–693.
- Cox, J., and Mann, M. (2008). MaxQuant enables high peptide identification rates, individualized p.p.b.-range mass accuracies and proteome-wide protein quantification. *Nat. Biotechnol.* 26, 1367–1372.
- Deliu, E., Arecco, N., Morandell, J., Dotter, C.P., Contreras, X., Girardot, C., Kasper, E.L., Kozlova, A., Kishi, K., Chiaradia, I., et al. (2018). Haploinsufficiency of the intellectual disability gene SETD5 disturbs developmental gene expression and cognition. *Nat. Neurosci.* 21, 1717–1727.
- Grozeva, D., Carss, K., Spasic-Boskovic, O., Parker, M.J., Archer, H., Firth, H.V., Park, S.M., Canham, N., Holder, S.E., Wilson, M., et al. (2014). De novo loss-of-function mutations in SETD5, encoding a methyltransferase in a 3p25 microdeletion syndrome critical region, cause intellectual disability. *Am. J. Hum. Genet.* 94, 618–624.
- Guenther, M.G., Barak, O., and Lazar, M.A. (2001). The SMRT and N-CoR corepressors are activating cofactors for histone deacetylase 3. *Mol. Cell Biol.* 21, 6091–6101.
- Hingorani, S.R., Petricoin, E.F., Maitra, A., Rajapakse, V., King, C., Jacobetz, M.A., Ross, S., Conrads, T.P., Veenstra, T.D., Hitt, B.A., et al. (2003). Preinvasive and invasive ductal pancreatic cancer and its early detection in the mouse. *Cancer Cell* 4, 437–450.
- Hingorani, S.R., Wang, L., Multani, A.S., Combs, C., Deramandt, T.B., Hruban, R.H., Rustgi, A.K., Chang, S., and Tuveson, D.A. (2005). Trp53R172H and KrasG12D cooperate to promote chromosomal instability and widely metastatic pancreatic ductal adenocarcinoma in mice. *Cancer Cell* 7, 469–483.
- Husmann, D., and Gozani, O. (2019). Histone lysine methyltransferases in biology and disease. *Nat. Struct. Mol. Biol.* 26, 880–889.
- Infante, J.R., Somer, B.G., Park, J.O., Li, C.P., Scheulen, M.E., Kasubhai, S.M., Oh, D.Y., Liu, Y., Redhu, S., Steplewski, K., et al. (2014). A randomised, double-blind, placebo-controlled trial of trametinib, an oral MEK inhibitor, in combination with gemcitabine for patients with untreated metastatic adenocarcinoma of the pancreas. *Eur. J. Cancer* 50, 2072–2081.
- Jonkers, J., Meuwissen, R., van der Gulden, H., Peterse, H., van der Valk, M., and Berns, A. (2001). Synergistic tumor suppressor activity of BRCA2 and p53 in a conditional mouse model for breast cancer. *Nat. Genet.* 29, 418–425.
- Kampmann, M., Bassik, M.C., and Weissman, J.S. (2014). Functional genomics platform for pooled screening and generation of mammalian genetic interaction maps. *Nat. Protoc.* 9, 1825–1847.
- Kapoor, A., Yao, W., Ying, H., Hua, S., Liewen, A., Wang, Q., Zhong, Y., Wu, C.J., Sadanandam, A., Hu, B., et al. (2014). Yap1 activation enables bypass of oncogenic Kras addiction in pancreatic cancer. *Cell* 158, 185–197.
- Kawaguchi, Y., Cooper, B., Gannon, M., Ray, M., MacDonald, R.J., and Wright, C.V. (2002). The role of the transcriptional regulator Ptf1a in converting intestinal to pancreatic progenitors. *Nat. Genet.* 32, 128–134.
- Khatri, P., Roedder, S., Kimura, N., De Vusser, K., Morgan, A.A., Gong, Y., Fischbein, M.P., Robbins, R.C., Naesens, M., Butte, A.J., et al. (2013). A common rejection module (CRM) for acute rejection across multiple organs identifies novel therapeutics for organ transplantation. *J. Exp. Med.* 210, 2205–2221.
- Kim, D., Langmead, B., and Salzberg, S.L. (2015). HISAT: a fast spliced aligner with low memory requirements. *Nat. Methods* 12, 357–360.
- Kim, M.P., Evans, D.B., Wang, H., Abbruzzese, J.L., Fleming, J.B., and Gallick, G.E. (2009). Generation of orthotopic and heterotopic human pancreatic cancer xenografts in immunodeficient mice. *Nat. Protoc.* 4, 1670–1680.
- Kinsey, C.G., Camolotto, S.A., Boespflug, A.M., Guillen, K.P., Foth, M., Truong, A., Schuman, S.S., Shea, J.E., Seipp, M.T., Yap, J.T., et al. (2019a). Protective autophagy elicited by RAF→MEK→ERK inhibition suggests a treatment strategy for RAS-driven cancers. *Nat. Med.* 25, 620–627.
- Kinsey, C.G., Camolotto, S.A., Boespflug, A.M., Guillen, K.P., Foth, M., Truong, A., Schuman, S.S., Shea, J.E., Seipp, M.T., Yap, J.T., et al. (2019b). Publisher correction: protective autophagy elicited by RAF→MEK→ERK inhibition suggests a treatment strategy for RAS-driven cancers. *Nat. Med.* 25, 861.
- Ko, A.H., Bekaii-Saab, T., Van Ziffle, J., Mirzoeva, O.M., Joseph, N.M., Talasz, A., Kuhn, P., Tempero, M.A., Collisson, E.A., Kelley, R.K., et al. (2016). A multicenter, open-label phase II clinical trial of combined MEK plus EGFR inhibition for chemotherapy-refractory advanced pancreatic adenocarcinoma. *Clin. Cancer Res.* 22, 61–68.
- Langmead, B., and Salzberg, S.L. (2012). Fast gapped-read alignment with Bowtie 2. *Nat. Methods* 9, 357–359.
- Lee, C.L., Moding, E.J., Huang, X., Li, Y., Woodlief, L.Z., Rodrigues, R.C., Ma, Y., and Kirsch, D.G. (2012). Generation of primary tumors with Flp recombinase in FRT-flanked p53 mice. *Dis. Model. Mech.* 5, 397–402.
- Liu, S., Hausmann, S., Carlson, S.M., Fuentes, M.E., Francis, J.W., Pillai, R., Lofgren, S.M., Hulea, L., Tandoc, K., Lu, J., et al. (2019). METTL13 methylation of eEF1A increases translational output to promote tumorigenesis. *Cell* 176, 491–504.e1.
- Love, M.I., Huber, W., and Anders, S. (2014). Moderated estimation of fold change and dispersion for RNA-seq data with DESeq2. *Genome Biol.* 15, 550.
- Manchado, E., Weissmueller, S., Morris, J.P.t., Chen, C.C., Wullenkord, R., Lujambio, A., de Stanchina, E., Poirier, J.T., Gainor, J.F., Corcoran, R.B., et al. (2016). A combinatorial strategy for treating KRAS-mutant lung cancer. *Nature* 534, 647–651.
- Mann, K.M., Ward, J.M., Yew, C.C., Kovoichich, A., Dawson, D.W., Black, M.A., Brett, B.T., Sheetz, T.E., Dupuy, A.J., Australian Pancreatic Cancer

- Genome, I., et al. (2012). Sleeping Beauty mutagenesis reveals cooperating mutations and pathways in pancreatic adenocarcinoma. *Proc. Natl. Acad. Sci. U S A* 109, 5934–5941.
- Mas, Y.M.S., Barbon, M., Teyssier, C., Demene, H., Carvalho, J.E., Bird, L.E., Lebedev, A., Fattori, J., Schubert, M., Dumas, C., et al. (2016). The human mixed lineage leukemia 5 (MLL5), a sequentially and structurally divergent SET domain-containing protein with no intrinsic catalytic activity. *PLoS One* 11, e0165139.
- Mazur, P.K., Reynoird, N., Khatri, P., Jansen, P.W., Wilkinson, A.W., Liu, S., Barbash, O., Van Aller, G.S., Huddleston, M., Dhanak, D., et al. (2014). SMYD3 links lysine methylation of MAP3K2 to Ras-driven cancer. *Nature* 510, 283–287.
- Molina, J.R., Sun, Y., Protopopova, M., Gera, S., Bandi, M., Bristow, C., McAfoos, T., Morlacchi, P., Ackroyd, J., Agip, A.A., et al. (2018). An inhibitor of oxidative phosphorylation exploits cancer vulnerability. *Nat. Med.* 24, 1036–1046.
- Nguyen, D. (2013). Quantifying chromogen intensity in immunohistochemistry via reciprocal intensity. *Nature Protocol Exchange*. <https://doi.org/10.1038/protex.2013.097>.
- Noll, E.M., Eisen, C., Stenzinger, A., Espinet, E., Muckenhuber, A., Klein, C., Vogel, V., Klaus, B., Nadler, W., Rosli, C., et al. (2016). CYP3A5 mediates basal and acquired therapy resistance in different subtypes of pancreatic ductal adenocarcinoma. *Nat. Med.* 22, 278–287.
- Osipovich, A.B., Gangula, R., Vianna, P.G., and Magnuson, M.A. (2016). Setd5 is essential for mammalian development and the co-transcriptional regulation of histone acetylation. *Development* 143, 4595–4607.
- Perera, R.M., Stoykova, S., Nicolay, B.N., Ross, K.N., Fitamant, J., Boukhali, M., Lengrand, J., Deshpande, V., Selig, M.K., Ferrone, C.R., et al. (2015). Transcriptional control of autophagy-lysosome function drives pancreatic cancer metabolism. *Nature* 524, 361–365.
- Perez-Mancera, P.A., Rust, A.G., van der Weyden, L., Kristiansen, G., Li, A., Sarver, A.L., Silverstein, K.A., Grutzmann, R., Aust, D., Rummele, P., et al. (2012). The deubiquitinase USP9X suppresses pancreatic ductal adenocarcinoma. *Nature* 486, 266–270.
- Ponz-Sarvise, M., Corbo, V., Tiriach, H., Engle, D.D., Frese, K.K., Oni, T.E., Hwang, C.I., Ohlund, D., Chio, I.I.C., Baker, L.A., et al. (2019). Identification of resistance pathways specific to malignancy using organoid models of pancreatic cancer. *Clin. Cancer Res.* 25, 6742–6755.
- Quinlan, A.R., and Hall, I.M. (2010). BEDTools: a flexible suite of utilities for comparing genomic features. *Bioinformatics* 26, 841–842.
- Ramirez, F., Ryan, D.P., Gruning, B., Bhardwaj, V., Kilpert, F., Richter, A.S., Heyne, S., Dundar, F., and Manke, T. (2016). deepTools2: a next generation web server for deep-sequencing data analysis. *Nucleic Acids Res.* 44, W160–W165.
- Rawla, P., Sunkara, T., and Gaduputi, V. (2019). Epidemiology of pancreatic cancer: global trends, etiology and risk factors. *World J. Oncol.* 10, 10–27.
- Ryan, D.P., Hong, T.S., and Bardeesy, N. (2014). Pancreatic adenocarcinoma. *N. Engl. J. Med.* 371, 1039–1049.
- Sastra, S.A., and Olive, K.P. (2014). Acquisition of mouse tumor biopsies through abdominal laparotomy. *Cold Spring Harb. Protoc.* 2014, 47–56.
- Schonhuber, N., Seidler, B., Schuck, K., Veltkamp, C., Schachtler, C., Zukowska, M., Eser, S., Feyerabend, T.B., Paul, M.C., Eser, P., et al. (2014). A next-generation dual-recombinase system for time- and host-specific targeting of pancreatic cancer. *Nat. Med.* 20, 1340–1347.
- Sessa, A., Fagnocchi, L., Mastrototaro, G., Massimino, L., Zaghi, M., Indrigo, M., Cattaneo, S., Martini, D., Gabellini, C., Pucci, C., et al. (2019). SETD5 regulates chromatin methylation state and preserves global transcriptional fidelity during brain development and neuronal wiring. *Neuron* 104, 271–289.e3.
- Shao, D.D., Xue, W., Krall, E.B., Bhutkar, A., Piccioni, F., Wang, X., Schinzel, A.C., Sood, S., Rosenbluh, J., Kim, J.W., et al. (2014). KRAS and YAP1 converge to regulate EMT and tumor survival. *Cell* 158, 171–184.
- Shi, X., Hong, T., Walter, K.L., Ewalt, M., Michishita, E., Hung, T., Carney, D., Pena, P., Lan, F., Kaadige, M.R., et al. (2006). ING2 PHD domain links histone H3 lysine 4 methylation to active gene repression. *Nature* 442, 96–99.
- Shi, Y., Sawada, J., Sui, G., Affar el, B., Whetstone, J.R., Lan, F., Ogawa, H., Luke, M.P., Nakatani, Y., and Shi, Y. (2003). Coordinated histone modifications mediated by a CtBP co-repressor complex. *Nature* 422, 735–738.
- Sidoli, S., Bhanu, N.V., Karch, K.R., Wang, X., and Garcia, B.A. (2016). Complete workflow for analysis of histone post-translational modifications using bottom-up mass spectrometry: from histone extraction to data analysis. *J. Vis. Exp.* <https://doi.org/10.3791/54112>.
- Sidoli, S., and Garcia, B.A. (2017). Characterization of individual histone post-translational modifications and their combinatorial patterns by mass spectrometry-based proteomics strategies. *Methods Mol. Biol.* 1528, 121–148.
- Siegel, R.L., Miller, K.D., and Jemal, A. (2019). Cancer statistics, 2019. *CA Cancer J. Clin.* 69, 7–34.
- Skarnes, W.C., Rosen, B., West, A.P., Koutourakis, M., Bushell, W., Iyer, V., Mujica, A.O., Thomas, M., Harrow, J., Cox, T., et al. (2011). A conditional knockout resource for the genome-wide study of mouse gene function. *Nature* 474, 337–342.
- Stephen, A.G., Esposito, D., Bagni, R.K., and McCormick, F. (2014). Dragging ras back in the ring. *Cancer Cell* 25, 272–281.
- Subramanian, A., Kuehn, H., Gould, J., Tamayo, P., and Mesirov, J.P. (2007). GSEA-P: a desktop application for gene set enrichment analysis. *Bioinformatics* 23, 3251–3253.
- Sulahian, R., Kwon, J.J., Walsh, K.H., Paillet, E., Bosse, T.L., Thaker, M., Almanza, D., Dempster, J.M., Pan, J., Piccioni, F., et al. (2019). Synthetic lethal interaction of SHOC2 depletion with MEK inhibition in RAS-driven cancers. *Cell Rep.* 29, 118–134.e8.
- Sun, C., Fang, Y., Yin, J., Chen, J., Ju, Z., Zhang, D., Chen, X., Vellano, C.P., Jeong, K.J., Ng, P.K., et al. (2017). Rational combination therapy with PARP and MEK inhibitors capitalizes on therapeutic liabilities in RAS mutant cancers. *Sci. Transl. Med.* 9, <https://doi.org/10.1126/scitranslmed.aal5148>.
- Sun, Y., Daemen, A., Hatzivassiliou, G., Arnott, D., Wilson, C., Zhuang, G., Gao, M., Liu, P., Boudreau, A., Johnson, L., et al. (2014). Metabolic and transcriptional profiling reveals pyruvate dehydrogenase kinase 4 as a mediator of epithelial-mesenchymal transition and drug resistance in tumor cells. *Cancer Metab.* 2, 20.
- Tachibana, M., Sugimoto, K., Fukushima, T., and Shinkai, Y. (2001). Set domain-containing protein, G9a, is a novel lysine-preferring mammalian histone methyltransferase with hyperactivity and specific selectivity to lysines 9 and 27 of histone H3. *J. Biol. Chem.* 276, 25309–25317.
- Vedadi, M., Barsyte-Lovejoy, D., Liu, F., Rival-Gervier, S., Allai-Hassani, A., Labrie, V., Wigle, T.J., Dimaggio, P.A., Wasney, G.A., Siarheyeva, A., et al. (2011). A chemical probe selectively inhibits G9a and GLP methyltransferase activity in cells. *Nat. Chem. Biol.* 7, 566–574.
- Vermeulen, M., Carrozza, M.J., Lasonder, E., Workman, J.L., Logie, C., and Stunnenberg, H.G. (2004). In vitro targeting reveals intrinsic histone tail specificity of the Sin3/histone deacetylase and N-CoR/SMRT corepressor complexes. *Mol. Cell. Biol.* 24, 2364–2372.
- Viale, A., Pettazzoni, P., Lyssiotis, C.A., Ying, H., Sanchez, N., Marchesini, M., Carugo, A., Green, T., Seth, S., Giuliani, V., et al. (2014). Oncogene ablation-resistant pancreatic cancer cells depend on mitochondrial function. *Nature* 514, 628–632.
- Wilkinson, A.W., Diep, J., Dai, S., Liu, S., Ooi, Y.S., Song, D., Li, T.M., Horton, J.R., Zhang, X., Liu, C., et al. (2019). SETD3 is an actin histidine methyltransferase that prevents primary dystocia. *Nature* 565, 372–376.
- Xu, C., Soragni, E., Chou, C.J., Herman, D., Plasterer, H.L., Rusche, J.R., and Gottesfeld, J.M. (2009). Chemical probes identify a role for histone deacetylase 3 in Friedreich’s ataxia gene silencing. *Chem. Biol.* 16, 980–989.
- Zhao, Y., and Adjei, A.A. (2014). The clinical development of MEK inhibitors. *Nat. Rev. Clin. Oncol.* 11, 385–400.

## STAR★METHODS

## KEY RESOURCES TABLE

REAGENT OR RESOURCE	SOURCE	IDENTIFIER
Antibodies		
Actin	Cell Signaling Technologies	Cat# 8457; RRID: AB_10950489
Cleaved Caspase 3	Cell Signaling Technologies	Cat# 9664; RRID: AB_2070042
ERK1/2	Cell Signaling Technologies	Cat# 4695; RRID: AB_390779
Phospho-ERK1/2	Cell Signaling Technologies	Cat# 4376; RRID: AB_331772
SHOC2	Cell Signaling Technologies	Cat# 53600; RRID: AB_2799440
Tubulin	Millipore	Cat# 05-661; RRID: AB_309885
Ki67	BD Bioscience	Cat# 550609; RRID: AB_393778
anti-Mouse HRP	Cell Signaling Technologies	Cat# 7076; RRID: AB_330924
anti-Rabbit HRP	Cell Signaling Technologies	Cat# 7074; RRID: AB_2099233
Peroxidase-conjugated Mouse Anti-Rabbit IgG, light chain specific	Jackson ImmunoResearch	Cat# 211-032-171; RRID: AB_2339149
AffiniPure Goat Anti-Mouse IgG, light chain specific	Jackson ImmunoResearch	Cat# 115-005-174; RRID: AB_2338460
Peroxidase-conjugated streptavidin	Jackson ImmunoResearch	Cat# 016-030-084; RRID: AB_2337238
CD45-Biotin	eBiosciences	Cat# 13-0451-81; RRID: AB_466445
CD31-Biotin	eBiosciences	Cat# 13-0319-80; RRID: AB_466422
Ter119-Biotin	eBiosciences	Cat# 13-5921-81; RRID: AB_466796
Biotin Micro Beads	Miltenyi Biotec	Cat# 130-042-401
SETD5	This paper	N/A
Histone H3	EpiCypher	Cat# 13-0001
Histone H3.3	RevMab	Cat# 31-1058-00; RRID: AB_2716425
Histone H4	EMD Millipore Corporation	Cat# 05-858; RRID: AB_390138
H3K4me1	Cell Signaling Technologies	Cat# 5326; RRID: AB_10695148
H3K4me2	Cell Signaling Technologies	Cat# 9725; RRID: AB_10205451
H3K4me3	Epicyphe	Cat# 13-0028
H3K9me1	Cell Signaling Technologies	Cat# 14186; RRID: AB_2798416
H3K9me2	Thermo Fisher Scientific	Cat# 710815; RRID: AB_2608303
H3K27me1	Epicyphe	Cat# 13-0015
H3K27me2	Cell Signaling Technologies	Cat# 9728; RRID: AB_1281338
H3K27me3	Cell Signaling Technologies	Cat# 9733; RRID: AB_2616029
H3K36me1	Abclonal	Cat# A2364; RRID: AB_2764324
H3K36me2	Thermo Fisher Scientific	Cat# 701767; RRID: AB_2633024
H3K36me3	Thermo Fisher Scientific	Cat# MA5-24687; RRID: AB_2661912
H3K4ac	Abclonal	Cat# A16078; RRID: AB_2763519
H3K9ac	Epicyphe	Cat# 13-0033
H3K14ac	Abclonal	Cat# A7254; RRID: AB_2737401
H3K18ac	Abclonal	Cat# A7257; RRID: AB_2767801
H3K27ac	Cell Signaling Technologies	Cat# 8173; RRID: AB_10949503
H3K36ac	Active motif	Cat# 39379; RRID: AB_2614977
H4K5ac	Abcam	Cat# ab51997; RRID: AB_2264109
H4K8ac	Abcam	Cat# ab45166; RRID: AB_732937
H4K12ac	Abcam	Cat# ab46983; RRID: AB_873859
H4K16ac	Abclonal	Cat# A5280; RRID: AB_2766099
H3K9me2	Thermo Fisher Scientific	Cat# 710815; RRID: AB_2608303

(Continued on next page)

**Continued**

REAGENT OR RESOURCE	SOURCE	IDENTIFIER
TBL1XR1	Abclonal	Cat# A7834; RRID: AB_2772539
TBL1XR1	Bethyl	Cat# A300-408A; RRID: AB_420967
G9a	Santa Cruz Biotechnology	Cat# sc-515726
G9a	Bethyl	Cat# A300-933A; RRID: AB_2097663
GLP	Bethyl	Cat# A301-642A; RRID: AB_1210961
HDAC3	Millipore	Cat# 17-10238; RRID: AB_11205568
HDAC3	Abcam	Cat# ab32369; RRID: AB_732780
NCoR1	Bethyl	Cat# A301-145A; RRID: AB_873085
TBL1	Abcam	Cat# ab24548; RRID: AB_2199904
TBL1	Santa Cruz Biotechnology	Cat# sc-137006; RRID: AB_2199796
GPS2	Abcam	Cat# ab153986
GST	(Shi et al., 2006)	N/A
FLAG	Sigma-Aldrich	Cat# F1804; RRID: AB_262044
Anti-FLAG M2 Affinity Gel	Sigma-Aldrich	Cat# A2220; RRID: AB_10063035
Anti-V5 Agarose Affinity Gel	Sigma-Aldrich	Cat# A7345; RRID: AB_10062721
<b>Bacterial and Virus Strains</b>		
DH5	Thermo Fisher Scientific	Cat# K4520-1
BL21	Thermo Fisher Scientific	Cat# C6070-03
Sf9	Thermo Fisher Scientific	Cat# 12659017
<b>Biological Sample</b>		
Human PDAC Tissue Array	MD Anderson Pathology	N/A
<b>Chemicals, Peptides, and Recombinant Proteins</b>		
RPMI 1640 Medium	Corning	Cat# MT10017CV
DMEM Medium	Corning	Cat# MT10040CV
Fetal bovine serum	Thermo Fisher Scientific	Cat# 10500056
PBS	Corning	Cat# MT21031CV
HBSS	Thermo Fisher Scientific	Cat# 14025076
Cysteine	Sigma-Aldrich	Cat# 30089
Trypsin-EDTA 0.25%	Corning	Cat# MT25053CI
Geneticin	Thermo Fisher Scientific	Cat# 10131027
Blasticidin S	Thermo Fisher Scientific	Cat# R21001
Puromycin	Thermo Fisher Scientific	Cat# A1113802
Hygromycin B	Corning	Cat# 30240CR
G418 Sulfate	Corning	Cat# MT30234CI
MACS separation columns	Miltenyi Biotech	Cat# 130-042-401
Complete Protease Inhibitor Cocktail	Sigma-Aldrich	Cat# 4693159001
Phosphatase Inhibitor Cocktail	Thermo Fisher Scientific	Cat# 78420
Hydrogen Peroxide	Thermo Fisher Scientific	Cat# H325-500
Sequencing Grade Modified Trypsin	Promega	Cat# V5113
Glu-C	Promega	Cat# V1651
TRIzol Reagent	Invitrogen	Cat# 15596018
Forane (Isoflurane)	AbbVie	Cat# B506
Papain	Worthington	Cat# LS003119
Bovine Serum Albumin (BSA)	Thermo Fisher Scientific	Cat# BP9703100
L-Reduced glutathione	Sigma-Aldrich	Cat# G4251-25G
S-adenosyl-methionine	New England Biolabs	Cat# B9003S
S-Adenosyl-L-[methyl- <sup>3</sup> H] methionine	American Radiolabeled Chemicals	Cat# ART0288
AMI-1	Sigma-Aldrich	Cat# 539209
TransIT-293	Mirus Bio	Cat# MIR-2706

(Continued on next page)

**Continued**

REAGENT OR RESOURCE	SOURCE	IDENTIFIER
NP-40	Sigma-Aldrich	Cat# I8896
Phenylmethylsulfonyl fluoride (PMSF)	Sigma-Aldrich	Cat# P7626
cOmplete, EDTA-free protease inhibitor	Sigma-Aldrich	Cat# 5056489001
Glucose	Sigma-Aldrich	Cat# G8270
Poly-L-lysine(PLL)	Sigma-Aldrich	Cat# P2636
Neurobasal™ Medium	Thermo Fisher Scientific	Cat# 21103049
B-27™ Supplement (50X)	Thermo Fisher Scientific	Cat# 17504044
SUPERase In RNase Inhibitor	Thermo Fisher Scientific	Cat# AM2694
RNasin Ribonuclease Inhibitors	Promega	Cat# N2511
UNC0638	Sigma-Aldrich	Cat# U4885
UNC0642	Selleckchem	Cat# S7230
RGFP966	Selleckchem	Cat# S7229
Pimasertib (AS-703026)	Selleckchem	Cat# S1475
Binimetinib	Selleckchem	Cat# S7007
Selumetinib	Selleckchem	Cat# S1008
SCH772984	Selleckchem	Cat# S7101
Trametinib (GSK1120212)	Selleckchem	Cat# S2673
Tamoxifen	Sigma-Aldrich	Cat# T5648
HeLa Mononucleosomes	Epiccypher	Cat# 16-0002
Recombinant nucleosome	Epiccypher	Cat# 16-0006
Recombinant Polynucleosomes (H3.3)	Active motif	Cat# 31468
3X FLAG Peptide	Sigma-Aldrich	Cat# F4799
CTH (Histones from calf thymus)	Sigma-Aldrich	Cat# 9064-47-5
H3K4ac dNuc	Epiccypher	Cat# 16-0342
H3K9ac dNuc	Epiccypher	Cat# 16-0314
H3K14ac dNuc	Epiccypher	Cat# 16-0343
H3K18ac dNuc	Epiccypher	Cat# 16-0372
H3K23ac dNuc	Epiccypher	Cat# 16-0364
H3K27ac dNuc	Epiccypher	Cat# 16-0365
H3K36ac dNuc	Epiccypher	Cat# 16-0378
H4K5ac dNuc	Epiccypher	Cat# 16-0352
H4K8ac dNuc	Epiccypher	Cat# 16-0353
H4K12ac dNuc	Epiccypher	Cat# 16-0312
H4K16ac dNuc	Epiccypher	Cat# 16-0354
DMSO	Sigma-Aldrich	Cat# D5879
(2-Hydroxypropyl)-β-cyclodextrin	Sigma-Aldrich	Cat# C0926
Corn oil	Sigma-Aldrich	Cat# C8267
PreScission Protease	This paper	N/A
Metaphosphoric acid	Sigma-Aldrich	Cat# 239275
16% Formaldehyde (w/v)	Sigma-Aldrich	Cat# F8775
N-acetyl-L-Cysteine (NAC)	Sigma-Aldrich	Cat#A7250
PVDF membrane (0.2 μm)	BioRad	Cat# 1620177
PVDF membrane (0.45 μm)	Millipore	Cat# IPVH00010
Glutathione Sepharose 4B	Sigma-Aldrich	Cat# GE17-0756-01
<b>Critical Commercial Assays</b>		
RNeasy Mini Kit	Qiagen	Cat# 74106
ZymoPURE Plasmid Miniprep Kit	Zymo	Cat# D4211
ZymoPURE II Plasmid Maxiprep Kit	Zymo	Cat# D4203
DNA PCR Purification Kit	Qiagen	Cat# 28106

(Continued on next page)

<b>Continued</b>		
REAGENT OR RESOURCE	SOURCE	IDENTIFIER
DAB Substrate Kit	Abcam	Cat# ab64238
Vectastain ABC kit	Vector Laboratories	Cat# PK-6100
BCA Protein Assay Kit	Pierce	Cat# 23227
ECL Substrate	Amersham	Cat# RPN2106
PCR Mycoplasma Test Kit I/C	PromoKine	Cat# PK-CA91-1096
InstantBlue Protein Stain	Expedeon	Cat# ISB1L
SilverQuest Silver Staining Kit	Thermo Fisher Scientific	Cat# LC6070
Site-directed mutagenesis kit	Agilent	Cat# 200523
MACS LS column	Miltenyi Biotec	Cat# 130-042-401
Glutathione Assay Kit	Cayman	Cat# 703002
Superscript First-strand Synthesis kit	Invitrogen	Cat# 18091050
SMARTer Stranded RNA-seq kit	Takara	Cat# 634839
Dynabeads mRNA purification kit	Thermo	Cat# 61006
PowerUP™SYBR™Green	Thermo Fisher Scientific	Cat# A25742
Cellfectin <sup>®</sup> II Reagent	Invitrogen	Cat# 10362
InstantBlue Protein Stain ISB1L	Fisher / Expedeon	Cat# 07-300-150
RNAimax Transfection Reagent	Thermo Fisher Scientific	Cat#13778030
ON-TARGETplus Mouse Shoc2 siRNA	Dharmacon	Cat# LQ-059319-01-0002
ON-TARGETplus Non-targeting Control	Dharmacon	Cat# D-001810-10-05
Deposited Data		
RNA-seq	This paper	NCBI GEO: <a href="#">GSE142046</a>
Experimental Models: Cell Lines		
Human: 293T/17	ATCC	Cat# CRL-11268
Human: MiaPaCa2	ATCC	Cat# CRL-1420
Human: PSN1	ATCC	Cat# CRL-3211
Human: CaPan1	ATCC	Cat# CRL-HTB-79
Human: Panc1 —	ATCC	Cat# CRL-1469
Human: YAPC	DSMZ	Cat# ACC-382
Human: DANG	DSMZ	Cat# ACC-249
Human: KP4	RIKEN	Cat# RCB-1005
Mouse: KPC ( <i>Kras;p53;Ptf1a<sup>Cre</sup></i> )	This paper	N/A
Experimental Models: Organisms/Strains		
Mouse: <i>Kras<sup>LSL-G12D</sup></i>	( <a href="#">Hingorani et al., 2003</a> )	Strain# JAX 008179
Mouse: <i>p53<sup>LoxP/LoxP</sup></i>	( <a href="#">Jonkers et al., 2001</a> )	Strain# JAX 008462
Mouse: <i>Ptf1a<sup>Cre</sup></i>	( <a href="#">Kawaguchi et al., 2002</a> )	MGI# 2387812
Mouse: <i>Setd5<sup>LoxP/LoxP</sup></i>	( <a href="#">Skarnes et al., 2011</a> )	Cat# VG17502
Mouse: <i>Kras<sup>FSF-G12D</sup></i>	( <a href="#">Schonhuber et al., 2014</a> )	MGI:5616879
Mouse: <i>p53<sup>Frt/Frt</sup></i>	( <a href="#">Lee et al., 2012</a> )	Strain# JAX 017767
Mouse: <i>Pdx1<sup>Flp</sup></i>	( <a href="#">Schonhuber et al., 2014</a> )	MGI# 5616872
Mouse: <i>ROSA26<sup>FSF-CreER</sup></i>	( <a href="#">Schonhuber et al., 2014</a> )	MGI# 5616874
Mouse: <i>NOD.SCID-IL2Rg<sup>-/-</sup></i> (NSG)	The Jackson Laboratories	Strain# 005557
Oligonucleotides		
sgRNA non-targeting (control) 5'-CTTCGAAATGTCGGTTCGGT-3'	This paper	N/A
sgRNA SETD5-1 human and mouse 5'-TTTGTGCAGCCCTGAATCTG-3'	This paper	N/A
sgRNA SETD5-2 human and mouse 5'-GCAGTGCAACAGAAAGCT-3'	This paper	N/A

(Continued on next page)

**Continued**

REAGENT OR RESOURCE	SOURCE	IDENTIFIER
sgRNA SETD5-3 human and mouse 5'-CGGAAGCAGGACAACATATC-3'	This paper	N/A
sgRNA SETD5-4 human and mouse 5'-ACGCTCTTCTCATTAACTGC-3'	This paper	N/A
sgRNA SETD2-1 mouse 5'-AATGAACTGGGATTCCGACG-3'	This paper	N/A
sgRNA SETD2-2 mouse 5'-GGAAGAAGAACAATCCCAC-3'	This paper	N/A
sgRNA HDAC3-1 human5'-CAGACC ACCAGCCCAGTTAA-3'	This paper	N/A
sgRNA HDAC3-2 human5'-GTTGAA GGCATTAAAGACTCT-3'	This paper	N/A
sgRNA G9a human 5'-GCGCCCCCATCTCAGCGG-3'	This paper	N/A
sgRNA GLP human 5'-GCGCAAGGGTCAACCCCC-3'	This paper	N/A
RT-qPCR SETD5 forward 5'-GAGAAAGAAACGGCGGGATC-3'	This paper	N/A
RT-qPCR SETD5 reverse 5'-TTTCTGCAGCTACATCCCCA-3'	This paper	N/A
RT-qPCR GSTA1 forward 5'-AAGAGAAGCCAAGACTGCCT-3'	This paper	N/A
RT-qPCR GSTA1 reverse 5'-TTCTTCACATTGGGGAGGCT-3'	This paper	N/A
RT-qPCR GSTA2 forward 5'-GAGCTTGATGCCAGCCTTCTGA-3'	This paper	N/A
RT-qPCR GSTA2 reverse 5'-TTCTCTGGCTGCCAGGATGTAG-3'	This paper	N/A
RT-qPCR GM3776 forward 5'-AGGTGTTGAAGAGCCATGGA-3'	This paper	N/A
RT-qPCR GM3776 reverse 5'-GGCTGCTGATTCTGCTCTTG-3'	This paper	N/A
RT-qPCR PDK4 forward 5'-TGGCTGTTTTGGTTATGGC-3'	This paper	N/A
RT-qPCR PDK4 reverse 5'-GTTCTTCGGTCCCTGCTTG-3'	This paper	N/A
RT-qPCR WNT7a forward 5'-TTCGGGAAGGAGCTCAAAGT-3'	This paper	N/A
RT-qPCR WNT7a reverse 5'-ATTCTGCTTGATCTCCCGGG-3'	This paper	N/A
RT-qPCR HTR3 forward 5'-AGTCCGCGGTACAAGTTCAA-3'	This paper	N/A
RT-qPCR HTR3 reverse 5'-ACCGGCTTCTGACATGATGA-3'	This paper	N/A
RT-qPCR Osgin1 forward 5'-ACAGACTTTGGAGGCAGCAT-3'	This paper	N/A
RT-qPCR Osgin1 reverse 5'-TTTCTTCCGCATCCAGTCTT-3'	This paper	N/A
RT-qPCR CD93 forward 5'-ATCAGTACAGCCCAACACCA-3'	This paper	N/A
RT-qPCR CD93 reverse 5'-ATACCTGCCTATCCCAAGCC-3'	This paper	N/A
RT-qPCR Serpinb1a forward 5'-TGTAAGTGGAGCCAGACCTG-3'	This paper	N/A

(Continued on next page)

<i>Continued</i>		
REAGENT OR RESOURCE	SOURCE	IDENTIFIER
RT-qPCR Serpinb1a reverse: 5'-GGAAGCGTGAATGGATGTCC-3'	This paper	N/A
RT-qPCR GSTT1 forward 5'-CCTGTGTGAGAGTGTGGCTA-3'	This paper	N/A
RT-qPCR GSTT1 reverse 5'-GCTCACCAAGGAAAACAGGG-3'	This paper	N/A
RT-qPCR GSTT2 forward 5'-GTGCCCAAGTCCACGAATAC-3'	This paper	N/A
RT-qPCR GSTT2 reverse 5'-TCCAGAGACATGAGATCCGC-3'	This paper	N/A
RT-qPCR CDH6 forward 5'-CTGAGCCGTTGAAAAGGAG-3'	This paper	N/A
RT-qPCR CDH6 reverse 5'-TAATGAAGAGATCGCCCGCT-3'	This paper	N/A
RT-qPCR MIA2 forward 5'-CCGAGTCTTAGCCCTGAGAG-3'	This paper	N/A
RT-qPCR MIA2 reverse 5'-ATCTCGACTGCATCTCTGGG-3'	This paper	N/A
RT-qPCR CDH17 forward 5'-TAAGACCAACCCTCCAGCTG-3'	This paper	N/A
RT-qPCR CDH17 reverse 5'-CCATGAGAATCCAAGGCTGC-3'	This paper	N/A
RT-qPCR NDN forward 5'-CTAACTTTGCAGCCGAGGTC-3'	This paper	N/A
RT-qPCR NDN reverse 5'-GCTGCAGGATTTTAGGGTCA-3'	This paper	N/A
ChIP-qPCR GSTA1-p1 forward 5'-ACCCACAGAGAAGTGCAGA-3'	This paper	N/A
ChIP-qPCR GSTA1-p1 reverse 5'-CTCTCAAATTCGCTGCCTC-3'	This paper	N/A
ChIP-qPCR GSTA1-p2 forward 5'-AAGAGAAGCCAAGACTGCCT-3'	This paper	N/A
ChIP-qPCR GSTA1-p2 reverse 5'-TCCCAGAAACTCAGTGCCC-3'	This paper	N/A
ChIP-qPCR PDK4-p1 forward 5'-CTCCTCCCTCTACCCTTTG-3'	This paper	N/A
ChIP-qPCR PDK4-p1 reverse 5'-GGCTCTGGGACTCTGAACTT-3'	This paper	N/A
ChIP-qPCR PDK4-p2 forward 5'-AGTGGTTCGGTGTCTGAGAG-3'	This paper	N/A
ChIP-qPCR PDK4-p2 reverse 5'-GATAGAAGCTGCTGACCCCT-3'	This paper	N/A
ChIP-qPCR GM3776-p1 forward 5'-GCTGAATCTGGTTTGGTGCA-3'	This paper	N/A
ChIP-qPCR GM3776-p1 reverse: 5'-ACGGTCTAGGGGTGAAAAGG-3'	This paper	N/A
ChIP-qPCR GM3776-p2 forward 5'-CAGCCGCTCCTACAATTCC-3'	This paper	N/A
ChIP-qPCR GM3776-p2 reverse 5'-CATGGGCACTTGGTCAAACA-3'	This paper	N/A
Recombinant DNA		
Plasmid: Setd5 <sup>tm1a</sup>	EuMMCR	Cat# PGS00019_A_B10
Plasmid: pLentiCRISPRv2	Feng Zhang Lab	Cat# Addgene #52961

(Continued on next page)

**Continued**

REAGENT OR RESOURCE	SOURCE	IDENTIFIER
Plasmid: pLentiCRISPRv2 hygro	Brett Stringer Lab	Cat# Addgene #98291
Plasmid: psPAX2	Trono Lab	Cat# Addgene #12260
Plasmid: pMD2.G	Trono Lab	Cat# Addgene #12259
Plasmid: pCMV-dR8.2 dvpr	Bob Weinberg Lab	Cat# Addgene #8455
Plasmid: pCMV-VSV-G	Bob Weinberg Lab	Cat# Addgene #8454
Plasmid: pUMVC	Bob Weinberg Lab	Cat# Addgene #8449
Plasmid: pBABE-neo	Bob Weinberg Lab	Cat# Addgene #1767
Plasmid: pWZL Blast GFP	Bob Weinberg Lab	Cat# Addgene #12269
Plasmid: pGEX-6P-1	GE Healthcare	Cat# 28-9546-48
Plasmid: pcDNA3.1(+)	Thermo Fisher Scientific	Cat# V7020
Plasmid: pENTR3C	Thermo Fisher Scientific	Cat# A10465
Plasmid: pLenti6.2 V5 DEST	Thermo Fisher Scientific	Cat# V36820
Plasmid: pLenti CMV Hygro DEST (w117-1)	Campeau and Kaufman lab	Cat# Addgene 17454
Plasmid: pQCXIH	Clontech	Cat# 631516
Plasmid: pet28a	Novagen	Cat# 69864-3
Plasmid: pFastbac1	Invitrogen	Cat# 10359-016
<b>Software and Algorithms</b>		
Prism 7	GraphPad	<a href="https://www.graphpad.com/">https://www.graphpad.com/</a> ; RRID:SCR_002798
Excel for Mac 2016	Microsoft	<a href="https://www.microsoft.com/en-us/">https://www.microsoft.com/en-us/</a> ; RRID:SCR_016137
PreciPoint M8 ViewPoint	PreciPoint	<a href="http://www.precipoint.com/microscopy-software/viewpoint/">http://www.precipoint.com/microscopy-software/viewpoint/</a>
ImageJ – Fiji package	Freeware	<a href="http://fiji.sc/">http://fiji.sc/</a> ; RRID:SCR_002285
Origin Pro 8	Microcal	<a href="https://www.originlab.com/">https://www.originlab.com/</a> RRID:SCR_002815
Horos	GNU Lesser General Public License, Version 3.0	<a href="https://www.horosproject.org/">https://www.horosproject.org/</a>
Gene Set Enrichment Analysis (GSEA)	(Subramanian et al., 2007)	<a href="http://software.broadinstitute.org/gsea/index.jsp">http://software.broadinstitute.org/gsea/index.jsp</a> RRID: SCR_003199
Bowtie2	(Langmead and Salzberg, 2012)	<a href="http://bowtie-bio.sourceforge.net/bowtie2/">http://bowtie-bio.sourceforge.net/bowtie2/</a>
Samtools	(Xu et al., 2009)	<a href="http://samtools.sourceforge.net/">http://samtools.sourceforge.net/</a>
HISAT2	(Kim et al., 2015)	<a href="https://ccb.jhu.edu/software/hisat2/index.shtml">https://ccb.jhu.edu/software/hisat2/index.shtml</a>
DESeq2	(Love et al., 2014)	<a href="http://bioconductor.org/packages/release/bioc/html/DESeq2.html">http://bioconductor.org/packages/release/bioc/html/DESeq2.html</a>
BEDTools	(Quinlan and Hall, 2010)	<a href="https://github.com/arq5x/bedtools2">https://github.com/arq5x/bedtools2</a>
DeepTools	(Ramirez et al., 2016)	<a href="https://deeptools.readthedocs.io/en/develop/">https://deeptools.readthedocs.io/en/develop/</a>
Trim_galore	Babraham Bioinformatics	RRID:SCR_011847
MaxQuant (v. 1.5.8.4)	(Cox and Mann, 2008)	<a href="http://www.coxdocs.org/doku.php?id=maxquant:start">http://www.coxdocs.org/doku.php?id=maxquant:start</a>
<b>Other</b>		
Superose 6 Increase 10/300GL column	Fisher / GE Healthcare	Cat# 29091596
ProtoArray® Human Protein Microarray	Thermo Fisher Scientific	Cat# PAH0525101
Orbitrap Elite	Thermo Fisher Scientific	N/A
Dionex Ultimate 3000 system	Thermo Fisher Scientific	N/A
Xcalibur Qual Browser	Thermo Fisher Scientific	N/A
Biospec USR70/30	Bruker	N/A

**RESOURCE AVAILABILITY**

**Lead Contact**

Further information and requests for resources and reagents should be directed to and will be fulfilled by the Lead Contact, Pawel K. Mazur ([pkmazur@mdanderson.org](mailto:pkmazur@mdanderson.org)).

### Materials Availability

Plasmids and antibodies generated in this study will be available upon request.

### Data and Code Availability

The accession number for the RNA-seq datasets reported in this paper is paper is NCBI GEO: [GSE142046](https://www.ncbi.nlm.nih.gov/geo/query/acc.cgi?acc=GSE142046). This study did not generate any unpublished code, software, or algorithm.

## EXPERIMENTAL MODEL AND SUBJECT DETAILS

### Mice

*Ptf1a<sup>+/-Cre</sup>*, *Pdx1<sup>Flp</sup>*, *Kras<sup>+/-LSL-G12D</sup>*, *Kras<sup>+/-FSF-G12D</sup>*, *p53<sup>LoxP/LoxP</sup>*, *p53<sup>Frt/Frt</sup>*, *Rosa26<sup>FSF-CreER</sup>* mice have been described before (Hingorani et al., 2003; Jonkers et al., 2001; Kawaguchi et al., 2002; Lee et al., 2012) (Schonhuber et al., 2014). Conditional *Setd5<sup>LoxP/LoxP</sup>* gene (NCBI Reference Sequence: NM\_144877.1) knockout mice were generated in this study using a targeting vector obtained from KOMP repository (PGS00019\_A\_B10) (Skarnes et al., 2011). The targeting vector includes the Neo cassette flanked by Frt sites and exons 3 to 6 sequence were flanked by LoxP sites. The linearized vector was subsequently delivered to ES cells (C57BL/6) via electroporation, followed by drug selection, PCR screening, and Southern blot confirmation. Correctly targeted ES clones were selected for blastocyst microinjection, followed by founder mice production. Founders were confirmed as germline-transmitted via cross-breeding with wild-type animals. In conjunction with germ line transmission of the mutant allele the self-excising Neo cassette was deleted. Mice were in a mixed C57BL/6;129/Sv background, and we systematically used littermates as controls in all the experiments. Immunocompromised NSG mice (*NOD.SCID-IL2Rg<sup>-/-</sup>*) were utilized for transplantation studies. All experiments were performed on balanced cohorts of male and female mice as our initial data did not indicate significant differences in disease progression or response to treatment between females or males. All animals were numbered and experiments were conducted in a blinded fashion. After data collection, genotypes were revealed and animals assigned to groups for analysis. For treatment experiments mice were randomized. None of the mice with the appropriate genotype were excluded from this study or used in any other experiments. Mice had not undergone prior treatment or procedures. All mice were fed a standard chow diet *ad libitum* and housed in pathogen-free facility with standard controlled temperature, humidity, and light-dark cycle (12 h) conditions with no more than 5 mice per cage under the supervision of veterinarians, in an AALAC-accredited animal facility at the University of Texas M.D. Anderson Cancer Center. All animal procedures were reviewed and approved by the MDACC Institutional Animal Care and Use Committee (IACUC 00001636, PI: Mazur).

### Cell Lines and Primary Cell Cultures

293T (female, embryonic kidney) cells were grown in DMEM medium supplemented with 10% fetal calf serum. MiaPaCa2 (male, 65 years old, pancreatic cancer), PSN1 (male, age not reported, pancreatic cancer), Panc1 (male, 56 years old, pancreatic cancer) and CaPan1 (male, 40 years old, pancreatic cancer), YAPC (male, 43 years old, pancreatic cancer), KP4 (male, 5-0 years old, pancreatic cancer), DANG (female, 68 years old, pancreatic cancer) cells were cultured in DMEM supplemented with 10% fetal bovine serum, glutamine, and 100 U/mL penicillin/streptomycin. Neural Stem Cells (NSCs) were derived from telencephalic cortex of embryos at E14.5. Embryonic cortices were dissociated, fragmented in Hank's Balanced Salt Solution with 1% Penicillin/Streptomycin and digested with papain (10 U/ml) and cysteine (1 mM) in HBSS with 0.5 mM EDTA. Primary cultures of mouse embryonic hippocampal neurons were prepared from E17.5 C57BL/6 wildtype mice according to the methods as described in (Sessa et al., 2019). All cells were cultured at 37°C in a humidified incubator with 5% CO<sub>2</sub>. Cell lines were authenticated by short tandem repeat profiling and tested negative for mycoplasma (PromoKine).

### Patient-Derived Cancer Xenografts and Mouse Allografts

Surgically resected tumor specimens were obtained from patients with histologically confirmed pancreatic cancer blinded for age and gender. All surgically resected tumors were collected after written patient consent and in accordance with the institutional review board-approved protocols of the University of Texas M.D. Anderson Cancer Center (PA19-0435, PI: Mazur). Patient-derived xenograft tumors were generated by transplanting small tumor fragments isolated directly from surgical specimens subcutaneously into mice as we established previously (Kim et al., 2009). In each case we first propagated the sample in NSG mice. For reconstitution assays, collected PDX tumors were minced using a razor blade and digested in collagenase digestion buffer at 37°C for 1 hour. Cells were passed through 100 μm and 40 μm cell strainers and centrifuged for 1200 rpm for 8 min. Cells were incubated in RBC lysis buffer for 2 min and then resuspended in 6 mL of media and spun through 0.5 mL of serum layered on the bottom of the tube to remove cellular debris. Contaminating human or mouse hematopoietic and endothelial cells (CD45, Ter119, CD31) are depleted using biotin conjugated anti-mouse CD45, CD31 and Ter119 antibodies and separated on a MACS LS column using anti biotin microbeads. Next, the cells were collected, mixed with matrigel (1:1) and transplanted to the flanks of NSG mice. When tumors became palpable, they were calipered every 3 days to monitor growth kinetics. Tumor volume was calculated using the formula: Volume = (*width*)<sup>2</sup> x *length* / 2 where *length* represents the largest tumor diameter and *width* represents the perpendicular tumor diameter.

## METHOD DETAILS

## Pancreatic Cancer Mouse Models

For pancreatic cancer development studies we used *Ptf1a*<sup>+Cre</sup>; *Kras*<sup>+LSL-G12D</sup>; *p53*<sup>LoxP/LoxP</sup> (*Kras*; *p53*) and *Ptf1a*<sup>+Cre</sup>; *Kras*<sup>+LSL-G12D</sup>; *p53*<sup>LoxP/LoxP</sup>; *Setd5*<sup>loxP/loxP</sup> (*Kras*; *p53*; *Setd5*) mice, which develop aggressive disease. Mice were followed for signs of disease progression. At the end of the experiment, tumors were processed for biochemical, histological and immunohistochemical analysis. Histopathological analysis was conducted on de-identified slides based on the classification consensus (Bailey et al., 2016).

For the two-stage tumorigenesis studies sequential genetic manipulation of the murine pancreas was accomplished through a combined Flp/Frt and Cre/LoxP system as previously reported (Schonhuber et al., 2014). Briefly, *Pdx*<sup>Flp</sup>; *Kras*<sup>FSF-G12D</sup>; *p53*<sup>Frt/Frt</sup>; *Rosa26*<sup>FSF-CreER</sup>; *Setd5*<sup>LoxP/LoxP</sup> mutant mice develop pancreatic cancer with high penetrance. Mice were monitored by Magnetic resonance imaging (MRI), as described below for tumor development. At the age of 8 weeks mice received Tamoxifen (1 mg in 100  $\mu$ l corn oil) per intraperitoneal injections on 3 consecutive days when tumor volumes had reached approximately 150 mm<sup>3</sup>. Control animals underwent the same procedure but received vehicle only treatment. Successful recombination of *Setd5*<sup>LoxP/LoxP</sup> was confirmed by PCR on DNA isolated from tumor biopsies and loss of SETD5 expression was verified by immunoblotting of whole cell lysate of tumor biopsies. For therapy studies mice were treated as indicated with Trametinib (0.3 mg/kg daily, IP), Selumetinib (50 mg/kg daily, IP), SCH727284 (25 mg/kg daily, IP), UNC0642 (G9a/GLP inhibitor, 5 mg/kg daily, IP), RGFP966 (HDAC3 inhibitor, 10 mg/kg daily, IP) or vehicle 10% (2-hydroxypropyl)- $\beta$ -cyclodextrin. Animals undergoing monotherapy also received placebo (vehicle).

## Magnetic Resonance imaging

Magnetic Resonance Imaging (MRI) experiments were performed on *Pdx*<sup>Flp</sup>; *Kras*<sup>FSF-G12D</sup>; *p53*<sup>Frt/Frt</sup>; *Rosa26*<sup>FSF-CreER</sup>; *Setd5*<sup>LoxP/LoxP</sup> and *Kras*; *p53* mutant mice at indicated age. Before imaging, mice were anesthetized by continuous gaseous infusion of 2% isoflurane for at least 10 min using a veterinary anesthesia system. During imaging, the dose was kept at 2% isoflurane, animal temperature was maintained and continuously monitored, respiratory and ECG monitoring were performed using an MRI-compatible physiological monitoring system and eyes were protected with an eye ointment. MRI was performed using the Biospec USR70/30, a small animal experimental MR imaging system based on an actively-shielded 7 T magnet with a 30 cm bore and cryo-refrigeration. The system is equipped with 6 cm inner-diameter gradients that deliver a maximum gradient field of 950 mT m<sup>-1</sup>. A 3.5 cm inner-diameter linear birdcage coil transmits and receives the MR signal. For image acquisition, T2-weighted, respiratory gated, multi-slice imaging will be performed with respiration held to under 25 breaths per minute to minimize motion artefacts in the abdomen. The rapid acquisition with relaxation enhancement (RARE) T2-weighted pulse sequence was modified to include an effective  $T_e$  (time of echo) of 38 ms, echo train length 9.5 ms, and number of averages equal to 4 in both the coronal and axial planes with a total TR (time repetition) of 2000 ms. A three-orientation (axial, sagittal, and coronal) scout image using a fast, low-angle single shot sequence was obtained to localize the mouse pancreas. Between 18 and 20 coronal and axial slices were acquired per mouse with a slice thickness of 0.7 mm and slice spacing of 1 mm to cover the entire pancreas. In plane, pixel sizes of 0.156 mm  $\times$  0.156 mm with a matrix size of 256  $\times$  192 and field of view (FOV) of 40 mm  $\times$  30 mm was chosen to minimize in plane partial volume effects, maintain a FOV sufficient to cover the abdomen, while also providing sufficient throughput for the experiment. MR images were analyzed using an open source Horos processing software. Pancreas tumor burden was measured by tracing the outer border of the region of suspected lesions on each slice after image intensities were normalized. Analysis was conducted on de-identified images. Tumor volume ( $V$ ) was assessed, using three-dimensional volumetric measurements according to the modified Simpson rule. In all contiguous transverse images, the area of tumor ( $A$ ) in each slice was multiplied by the slice profile (0.7 mm slice thickness plus 1 mm intersection gap), and total tumor volume was automatically calculated by summation of the adjacent volume according to the formula:

$$V = T_s \times \left( \sum_{i=1}^n A_i \right)$$

where  $T_s$  is the thickness of each slice,  $i$  is the individual slice number and  $n$  is the total number of slices.

## Histology and Immunohistochemistry

Tissue specimens were fixed in 4% buffered formalin for 24 hours and stored in 70% ethanol until paraffin embedding. 3  $\mu$ m sections were stained with hematoxylin and eosin (HE) or used for immunohistochemical studies. Human tissue sections were collected in accordance with the institutional review board-approved protocols of the University of Texas M.D. Anderson Cancer Center (PA19-0435, PI: Mazur). Immunohistochemistry (IHC) was performed on formalin-fixed, paraffin embedded mouse and human tissue sections using a biotin-avidin method as described before (Mazur et al., 2014). The following antibodies were used (at the indicated dilutions): cleaved caspase 3 (1:100), Ki67 (1:1,000) and SETD5 (1:100). Sections were developed with DAB and counterstained with hematoxylin. Pictures were taken using a PreciPoint M8 microscope equipped with the PointView software. Analysis of the tumor area and IHC analysis was done using ImageJ software. Quantification of SETD5 IHC chromogen intensity was performed by measuring the reciprocal intensity of the chromogen stain as previously described (Nguyen, 2013). Briefly, standard RGB color images acquired from bright field microscopy have a maximum intensity of value 250 (represented by white, unstained areas) as

measured by the standard intensity function in the open source ImageJ Fiji software. We subtracted the intensity of a stained tissue sample from 250, thereby deriving a reciprocal intensity that is directly proportional to the amount of chromogen present.

### Meta-Analysis of Gene Expression

Meta-analysis of public PDAC data sets. We downloaded raw data for gene expression studies (7 pancreatic cancer) from the NCBI GEO and EBI ArrayExpress. After re-annotating the probes, each data set was normalized separately using gcRMA. We applied two meta-analysis approaches to the normalized data. The meta-analysis approach was previously described (Khatri et al., 2013). Briefly, the first approach combines effect sizes from each data set into a meta-effect size to estimate the amount of change in expression across all data sets. For each gene in each data set, an effect size was computed using Hedges' adjusted  $g$ . If multiple probes mapped to a gene, the effect size for each gene was summarized using the fixed effect inverse-variance model. We combined study-specific effect sizes to obtain the pooled effect size and its standard error using the random effects inverse-variance technique. We computed  $z$ -statistics as a ratio of the pooled effect size to its standard error for each gene and compared the result to a standard normal distribution to obtain nominal  $p$  values that were corrected for multiple hypotheses testing using false discovery rate (FDR). We used a second non-parametric meta-analysis that combines  $p$  values from individual experiments to identify genes with a large effect size in all data sets. Briefly, we calculated a  $t$ -statistic for each gene in each study. After computing one-tail  $p$  values for each gene, they were corrected for multiple hypotheses using FDR. Next, we used Fisher's sum of logs method, which sums the logarithm of corrected  $p$  values across all data sets for each gene and compares the sum against a chi-square distribution with  $2k$  degrees of freedom, where  $k$  is the number of data sets used in the analysis.

### Transfection and Viral Transduction

Transient expression was performed using TransIT-293 following the manufacturer's protocol. For CRISPR/Cas9 knockouts, virus particles were produced by co-transfection of 293T cells with the pLentiCRISPR v2 (with puromycin selection) construct expressing indicated sgRNAs, pMD2.G and psPAX2 in a ratio of 5:2:3 by mass. 48 hours after transfection, target cells were transduced with 0.45  $\mu\text{m}$  filtered viral supernatant and 8  $\mu\text{g}/\text{mL}$  polybrene. Cells were selected 24 hours after media replacement with 2  $\mu\text{g}/\text{mL}$  puromycin or 250  $\mu\text{g}/\text{mL}$  hygromycin B. For SETD5 reconstitution, virus particles were produced by co-transfection of 293T cells with the pLenti CMV Hygro DEST (w117-1) expressing human SETD5, pMD2.G and psPAX2 in a ratio of 5:2:3 by mass. 48 hours after transfection, target cells were transduced with 0.45  $\mu\text{m}$  filtered viral supernatant and 8  $\mu\text{g}/\text{mL}$  polybrene. Cells were selected 24 hours after media replacement with 250  $\mu\text{g}/\text{mL}$  hygromycin B, after one week selection, the cells expressing human SETD5 (with sgRNA tolerance synonymous mutation) were transduced with sgControl and sgSETD5 virus (sgSETD5-2). Cells were selected 24 hours after media replacement with 2  $\mu\text{g}/\text{mL}$  puromycin. After 5 days selection, cells were harvested for western blot, RNA purification or ChIP.

### Plasmids

Full length human SETD5 (NP\_001073986.1), SETD5 $\Delta$ SET (aa 511-1442), SETD5 $\Delta$ C (aa 1-520) were cloned into pQCXIH vector with V5 tag at N-terminal with PreScission Protease cutting site and FLAG tag at C-terminal for sequential immunoprecipitation. Stable cells were generated using pLenti CMV Hygro DEST(w117-1); pLentiCRISPRv2 was used for CRISPR/Cas9 knockouts in cell lines. For bacterial expression, human SETD5 $\Delta$ C, human SETD5 (aa 1-415), murine SETD5 (aa 1-423) (NP\_766593), SETD2-SET (aa 1418-1714) (NP\_054878.5), G9a (aa 913-1193) (NP\_006700.3), NSD2 (aa 942-1240) (NP\_579877.1) and MLL4 (aa 2551-2715) (NP\_055542.1) were cloned into pGEX-6P-1, ASH2L (NP\_001098684), RBBP5 (NP\_005048), WDR5 (NP\_060058.1), DPY30 (NP\_115963) were cloned into pet28a; for Sf9 insect cell expression, human Flag-SETD5, PRC2 complex (Flag-EZH2 (NP\_001190176.1), EED (NP\_003788.2), SUZ12 (NP\_056170), RbAp46 (NP\_002884.1) and RbAp48 (NP\_005601.2)), Flag-HDAC3 (NP\_003874.2) and GST-NCoR1-DAD domain (aa 397-503) (NP\_006302) were cloned into pFastbac1.

### Pooled shRNA Screen

We have generated lentiviral shRNA sub-library (Bassik et al., 2009, 2013) containing 25 independent shRNAs directed against one of 95 known and putative human methyltransferase genes, including the vast majority of known protein lysine methyltransferase (KMTs) present in the human genome (shRNA targeting sequences are listed in Table S1). In addition, the library contains 1,000 negative control shRNAs that have the same overall base composition as the other shRNAs, but do not match the sequence of any human transcript. MiaPaCa2 cells were transduced with the lentivirus pool containing shRNAs as described previously (Bassik et al., 2009, 2013). Infected cells were expanded and split into two flasks. In one flask, cells were grown in the presence of 10 nM Trametinib (MEKi) for 12 days, while in the other flask, cells were grown in vehicle (DSMO). Untreated cells were diluted to a density of 500,000 cells/ml each day. MEKi-treated cells were diluted to a density of 500,000 cells/ml as needed. After the cell culture period, untreated and MEKi-treated cells were collected. Genomic DNA was isolated, and shRNA encoding-constructs were counted by deep sequencing as described previously (Bassik et al., 2009, 2013) and frequencies of shRNA-encoding cassettes were determined by next-generation sequencing (Illumina HiSeq). The MEKi resistance screen was carried out in two independent replicates. The MEKi resistance  $\rho$  conferred by an individual shRNA was calculated as described previously (Bassik et al., 2013). The set of  $\rho$  values of all shRNAs for a given gene were compared to the set of  $\rho$  values for the negative control shRNAs, and the significance by Mann-Whitney U test for enrichment (resistance) or depletion (sensitivity) was calculated (see also Table S1).

### Immunoblot Analysis and Immunoprecipitation

For western blot analysis, cells were lysed in RIPA buffer with 1 mM PMSF and protease inhibitor cocktail. Protein concentration was determined using the Pierce Coomassie Plus Assay. Protein samples were resolved by SDS-PAGE and transferred to a PVDF membrane (0.45  $\mu\text{m}$ ). The following antibodies were used (at the indicated dilutions): ERK1/2 (1:2,000), phospho-ERK1/2 (1:5,000), SETD5 (1:1,000, this paper), SETD2 (1:1,000), SHOC2 (1:1,000), G9a (1:1,000), GLP (1:1,000), HDAC3 (1:1,000), NCoR1 (1:1,000), TBL1 (1:1,000), TBL1XR1 (1:1,000), GPS2 (1:1,000), GST (1:5,000), Flag (1:1,000), Actin (1:10,000), Tubulin (1:2,000), H3 (1:5,000), H3.3 (1:1,000), H4 (1:3,000), H3K9ac (1:2,000), H3K36me1 (1:5,000), H4K5ac (1:2,000), H4K8ac (1:2,000), all the other histone modification antibodies (1:1,000). Secondary antibodies were used at 1:5,000 or 1:10,000 dilution. Protein bands were visualized using ECL detection reagent.

For immunoprecipitation, nuclear extracts were incubated with specific antibody overnight at 4°C, antibodies for immunoprecipitation were used at the indicated amount: 5  $\mu\text{g}$  SETD5 (lab generated), 3  $\mu\text{g}$  HDAC3 (Abcam), 5  $\mu\text{g}$  G9a (Bethyl). Extracts were then incubated with protein A Sepharose beads for 3 hours at 4°C; For tandem-affinity purification (TAP), nuclear extracts were incubated with 50  $\mu\text{l}$  Anti-V5 Agarose affinity gel for 5 hours, after washing, proteins were cleaved from beads using 5  $\mu\text{g}$  PreScission Protease for 3 hours, cleaved proteins were incubated with 20  $\mu\text{l}$  Anti-FLAG M2 affinity gel for another 5 hours and eluted using 0.25 mM 3XFLAG peptides for 1 hour at 4°C. Proteins were resolved by SDS-PAGE, transferred to PVDF membrane and analyzed by western blot.

### Generation of SETD5 Antibody

Human SETD5 (aa 1-131, NP\_001073986.1) was cloned into pGEX-6P-1 and expressed in BL21 *E. coli*. SETD5 protein fragment was purified using GST Glutathione Sepharose 4B resin and cleaved from the beads using PreScission Protease. The purified protein fragment was used to immunize rabbits using standard methods (performed by Genemed Synthesis, Inc.)

### Expression and Purification of Recombinant Proteins

GST fusion proteins were expressed in BL21 *E. coli* by overnight culture at 20°C in LB medium (10 g/L tryptone, 5 g/L yeast extract, and 10 g/L NaCl) supplemented with 0.1 mM IPTG, purified using Glutathione Sepharose 4B and eluted in 10 mM reduced glutathione or cut from beads using PreScission Protease. Insect expression was done according to manufacturer's protocol Bac-to-Bac Baculovirus Expression System. Next, the cell lysates were incubated with Anti-FLAG M2 affinity gel for 5 hours, after washing, proteins were cleaved from beads using 5  $\mu\text{g}$  PreScission Protease for 3 hours. For HDAC3/NCoR1-DAD purification, the complex was cleaved from beads using PreScission Protease for 3 hours, cleaved proteins were incubated with Glutathione Sepharose 4B for 2 hours and eluted in 10 mM reduced glutathione. The proteins purified were snap frozen and stored in -80°C or used in *in vitro* reaction assays directly. Protein concentrations were measured using Coomassie assay.

### ProtoArray, Methylation and Deacetylation Assays

*In vitro* methylation assays were performed similar to as described in (Mazur et al., 2014) by combining 0.5-2  $\mu\text{g}$  recombinant enzymes or 2  $\mu\text{g}$  SETD5 complex and 1-2  $\mu\text{g}$  substrates (bulk histones, recombinant H3, recombinant nucleosomes) in a methyltransferase buffer (50 mM Tris pH 8.0, 20 mM KCl, 5 mM MgCl<sub>2</sub>, and 10% glycerol) supplemented with 0.1 mM S-adenosyl-methionine (SAM) or 2  $\mu\text{Ci}$  of tritiated AdoMet. The reaction mixtures were incubated overnight at 30°C. Reactions were analyzed by SDS-PAGE, followed by autoradiography, Coomassie stain, western blot or mass spectrometry. *In vitro* methylation assays with SETD2<sup>SET</sup>, human SETD5 (aa 1-415) and murine SETD5 (aa 1-423) were performed using the reaction buffer (50 mM Tris pH 8.8, 5 mM MgCl<sub>2</sub>, 4 mM DTT) supplemented with 50  $\mu\text{M}$  S-adenosyl-methionine (SAM) or 2  $\mu\text{Ci}$  of tritiated AdoMet. The reactions using enzymes purified from insect cells and 293T cells were supplied with AMI-1 (40  $\mu\text{g}/\text{mL}$ ) to inhibit activity of protein arginine N-methyltransferases potentially interfering with the experiment. For *in vitro* deacetylation assay 0.1  $\mu\text{g}$  recombinant HDAC3/NCoR1-DAD complex or 1  $\mu\text{g}$  SETD5 complex and 1  $\mu\text{g}$  of HeLa nucleosomes or 0.2  $\mu\text{g}$  of synthesized nucleosomes were incubated in a histone deacetylase reaction buffer (50 mM Tris pH 8.0, 137 mM NaCl, 2.7 mM KCl, 1 mM MgCl<sub>2</sub>) at 27°C for 5 hours. Reactions were analyzed by SDS-PAGE, followed by western blot.

### Gel Filtration

Gel filtration chromatography was performed using Superose 6 Increase 10/300GL prepacked column. Nuclear extracts (1 mL) were loaded on the equilibrated column and eluted with buffer (10 mM Tris-HCl pH 8.0, 150 mM NaCl, 1 mM EDTA) at flow rate of 0.25 ml/min, collecting fractions, 0.4 mL each tube. Fractions were analyzed by SDS-PAGE, followed by western blot.

### Mass Spectrometry

Recombinant nucleosomes were separated by SDS-PAGE (15%) and stained using InstantBlue Protein Stain without methanol. Histone H3 gel bands were cut into small pieces and subjected to chemical derivatization with propionic anhydride using the same protocol as previously described (Sidoli et al., 2016; Sidoli and Garcia, 2017). Peptides were separated by high pressure liquid chromatography (HPLC) using Dionex Ultimate 3000 LC-system and analyzed with an Orbitrap Elite mass spectrometer. Full MS spectra were acquired in the Orbitrap mass analyzer and MS/MS spectra were obtained by selection of top 20 ions followed by collision induced dissociation (CID) analysis of fragment ions in the ion trap. Methylation states of histones were manually inspected.

Selected ion chromatograms for peptides spanning H3K9 were extracted using Xcalibur Qual Browser. The settings were as follows: Peptide H3 9-17(KSTGGKAPR), m/z 535.3037(me0), 542.3115(me1), 521.3062 (me2) and 528.3140(me3), 10p.p.m.

For SETD5 complex protein identification V5-SETD5-Flag tandem-affinity purified (TAP) material was separated by 10% SDS-PAGE and silver stained. Protein bands were excised from the gel and analyzed by mass spectrometry. Liquid chromatography-tandem mass spectrometry (LC-MS/MS) was performed using an Orbitrap Elite and data were analyzed using MaxQuant software.

### Quantitative RT-PCR

For quantitative RT-PCR, RNA was extracted using TRIzol Reagent according to the manufacturer's instructions, cDNA synthesis was obtained using the Superscript First-strand Synthesis kit. RT-qPCR was performed in triplicate with custom designed oligos using standard methods.

### RNA-Sequencing and Data Analysis

Total RNA was extracted from KPC<sub>R</sub> cells (n = 3) (sgControl + Trametinib 0.2  $\mu$ M, sgSETD5 + Trametinib 0.2  $\mu$ M, or DMSO + Trametinib 0.2  $\mu$ M, UNC0638 0.6  $\mu$ M + RGFP966 0.6  $\mu$ M + Trametinib 0.2  $\mu$ M) using Trizol reagent. Total RNA was subjected to polyA selection using Dynabeads mRNA purification kit. 20 ng polyA RNA was utilized for library generation using SMARTer Stranded RNA-seq kit. The RNA-seq libraries were sequenced using Illumina HiSeq 3000 platform (pair end 150 bp analysis). RNA-seq data processing, low-quality and adapter-containing reads were trimmed using *Trim-galore* software package under paired-end mode, any reads shorter than 50 bp were removed. The remaining trimmed sequences were mapped to the reference genome (mm10) with hisat2 under default settings. We used htseq-count to count the mapped reads number on every mm10 Refseq transcript. Differential gene expression analysis was performed with DESeq2 software. Genes with p value  $\leq$  0.05, log<sub>2</sub> fold change  $\geq$  0.5 were defined as up-regulated genes, and genes with p value  $\leq$  0.05 log<sub>2</sub> fold change  $\leq$  -0.5 were defined as down-regulated genes. Enrichment analysis was performed for KEGG pathways. Gene set enrichment analysis (GSEA) was performed using the Broad Institute of the Massachusetts Institute of Technology and Harvard University software. For both gene sets, we used the default parameters of the GSEA software package; the genes set permutation was used. In brief, the normalized enrichment score provides the degree to which a gene set is overrepresented at the top or bottom of a ranked list of genes. The false discovery rate q value (FDR) is the estimated probability that a gene set with a given NES represents a false positive finding, an FDR cutoff of 0.05 was used for all analysis.

### Chromatin Immunoprecipitation (ChIP)

Cells were fixed with 1% formaldehyde for 10 min at room temperature before termination with 0.125 M glycine. Cells were then lysed in ChIP buffer (0.3% SDS, 300 mM NaCl, 1 mM EDTA, and 50 mM Tris-HCl pH 8.0), and cross-linked chromatin was sonicated to obtain DNA fragments around 250 bp. After sonication, dilute the 0.3% SDS to 0.1% SDS with ChIP dilution buffer (300 mM NaCl, 1 mM EDTA, and 50 mM Tris-HCl pH 8.0). Immunoprecipitations were performed using the diluted samples that were incubated at 4°C for 3 hours with following antibodies: SETD5 (3  $\mu$ g, this paper), H3K9ac (2  $\mu$ g), H3K9me2 (3  $\mu$ g). Next, 10-15  $\mu$ L protein A/G beads were added and incubated at 4°C for 5 hours. Then beads were treated with binding buffer (0.1% SDS, 300 mM NaCl, 10 mM EDTA, and 50 mM Tris-HCl pH 8.0) 4 times, wash buffer (1 mM EDTA, 50 mM Tris-HCl pH 8.0) twice, LiCl buffer (20 mM Tris, pH 7.4, 1 mM EDTA, 250 mM LiCl, 0.5% NP-40, 0.5% Na-deoxycholate) once and TE buffer (10 mM Tris pH 8.0, 1 mM EDTA) once. DNA was eluted from beads using elution buffer (50 mM Tris pH 8.0, 10 mM EDTA, 1% SDS) and de-crosslinked at 65°C for 4 hours. DNA was recovered by PCR Purification Kit. RT-qPCR analyses were performed on immunoprecipitated DNA using specific primers. The results were presented as relative fold enrichment over the input.

### GSH Assay

Reduced cellular glutathione (GSH) was determined enzymatically using a Glutathione assay kit according to manufacturer's protocol. Briefly,  $1 \times 10^7$  KPC<sub>R</sub> cells were washed with PBS, incubated with 500  $\mu$ L MES reagent and sonicated for 1 min and then centrifuged at 13,500 rpm for 15 min at room temperature. Next, the samples were deproteinated by adding 500  $\mu$ L of 10% metaphosphoric acid reagent and centrifuged at 13,500 rpm for 3 min at room temperature. Next, the supernatant was treated with 50  $\mu$ L TEAM reagent. Total glutathione concentration was determined kinetically by measuring the formation of 5-thio-2-nitrobenzoic acid from 5, 5'-dithionitrobenzoic acid in the presence of NADPH and glutathione reductase fluorometrically at 405 nm.

### Cell Assays

To analyze cell proliferation cancer cells were seeded at  $2 \times 10^5$  cells/mL in triplicate in 6-well plates. Cell counts were acquired by Countess II FL automated cell counter at indicated days. After each counting, the cells were maintained at a density between  $2-4 \times 10^5$  cells/mL. Trypan blue was used to stain non-viable cells. Cell numbers were expressed relative to  $1 \times 10^5$  cells/mL. For analysis of cell response to MEKi we used the InCuCyte live cell imaging system. Cells were seeded at a concentration of 4,000 cells per well in 96-well plate and allowed to attach overnight. Next, MEKi at specified concentration was added and cells were analyzed every 4 hours for confluency.

To analyze SETD5 expression upon MEKi treatment mouse KPC<sub>N</sub> cells were treated with MEK1/2 inhibitors at low concentration of Binimetinib (10 nM), Pimasertib (10 nM), Selumetinib (10 nM) and Trametinib (5 nM) for the first week, then concentration was

gradually increased to Binimetinib (0.6  $\mu$ M), Pimasertib (1  $\mu$ M), Selumetinib (0.5  $\mu$ M) and Trametinib (0.2  $\mu$ M) over the 4 weeks. After inhibitor treatment, total protein and RNA were isolated from the cells and analyzed by western blot and quantitative RT-qPCR.

#### siRNA Transfection

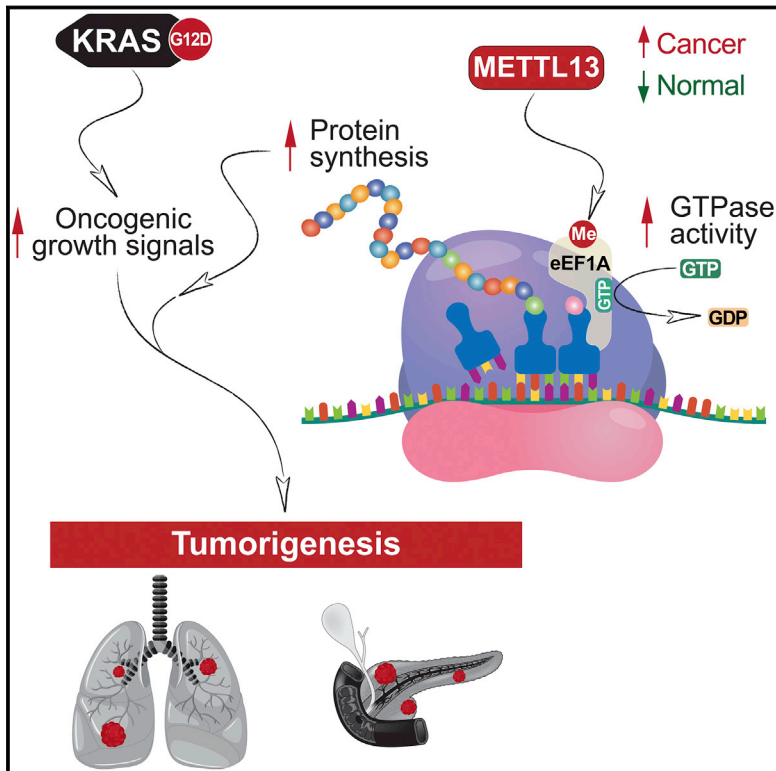
To perform SHOC2 depletion  $5 \times 10^5$  KPC<sub>R</sub> and KPC<sub>N</sub> cells were transfected with 30 pmol siRNA oligo mix utilizing RNAimax transfection reagent for 48 hours according to manufacturer's protocol. Following 48 hours post-transfection, cells were utilized to perform proliferation assay and western blot analysis.

#### QUANTIFICATION AND STATISTICAL ANALYSIS

Please refer to the Figure Legends or the Experimental Details for description of sample size (n) and statistical details. All values for n are for individual mice or individual sample. Sample sizes were chosen based on previous experience with given experiments. Cell culture assays have been performed in triplicates and in two independent experiments, unless stated otherwise. Differences were analyzed by log-rank, two-tailed unpaired Student's t test, Mann-Whitney U test, two-way ANOVA with Tukey's testing for multiple comparisons using Prism 7 (GraphPad), p values  $\leq 0.05$  were considered significant.

# METTL13 Methylation of eEF1A Increases Translational Output to Promote Tumorigenesis

## Graphical Abstract



## Authors

Shuo Liu, Simone Hausmann,  
Scott Moore Carlson, ...,  
Capucine Van Rechem,  
Pawel Karol Mazur, Or Gozani

## Correspondence

pkmazur@mdanderson.org (P.K.M.),  
ogozani@stanford.edu (O.G.)

## In Brief

Ras-driven cancers ramp up protein synthesis by increasing the GTPase activity of a translation elongation factor through a mechanism that involves METTL13-catalyzed eEF1A dimethylation

## Highlights

- METTL13 is the physiologic eEF1A lysine 55 dimethyltransferase
- METTL13 dimethylation of eEF1A stimulates protein synthesis in cancer cells
- The METTL13-eEF1A methylation axis fuels Ras-driven tumorigenesis *in vivo*
- METTL13 depletion sensitizes cancer cells to PI3K and mTOR pathway inhibitors



# METTL13 Methylation of eEF1A Increases Translational Output to Promote Tumorigenesis

Shuo Liu,<sup>1,13</sup> Simone Hausmann,<sup>2,13</sup> Scott Moore Carlson,<sup>1</sup> Mary Esmeralda Fuentes,<sup>2</sup> Joel William Francis,<sup>1</sup> Renjitha Pillai,<sup>3</sup> Shane Michael Lofgren,<sup>2</sup> Laura Hulea,<sup>4</sup> Kristofferson Tandoc,<sup>4</sup> Jiuwei Lu,<sup>5</sup> Ami Li,<sup>6</sup> Nicholas Dang Nguyen,<sup>2</sup> Marcello Caporicci,<sup>2</sup> Michael Paul Kim,<sup>7</sup> Anirban Maitra,<sup>8</sup> Huamin Wang,<sup>8,9</sup> Ignacio Ivan Wistuba,<sup>8,10</sup> John Anthony Porco, Jr.,<sup>11</sup> Michael Cory Bassik,<sup>6</sup> Joshua Eric Elias,<sup>12</sup> Jikui Song,<sup>5</sup> Ivan Topisirovic,<sup>4</sup> Capucine Van Rechem,<sup>3</sup> Pawel Karol Mazur,<sup>2,\*</sup> and Or Gozani<sup>1,14,\*</sup>

<sup>1</sup>Department of Biology, Stanford University, Stanford, CA 94305, USA

<sup>2</sup>Department of Experimental Radiation Oncology, The University of Texas MD Anderson Cancer Center, Houston, TX 77030, USA

<sup>3</sup>Department of Pathology, Stanford University School of Medicine, Stanford, CA 94305, USA

<sup>4</sup>Lady Davis Institute and Gerald Bronfman Department of Oncology, McGill University, Montreal, QC H3T 1E2, Canada

<sup>5</sup>Department of Biochemistry, University of California, Riverside, Riverside, CA 92521, USA

<sup>6</sup>Department of Genetics, Stanford University School of Medicine, Stanford, CA 94305, USA

<sup>7</sup>Department of Surgical Oncology, The University of Texas MD Anderson Cancer Center, Houston, TX 77030, USA

<sup>8</sup>Department of Translational Molecular Pathology, The University of Texas MD Anderson Cancer Center, Houston, TX 77030, USA

<sup>9</sup>Department of Pathology, The University of Texas MD Anderson Cancer Center, Houston, TX 77030, USA

<sup>10</sup>Department of Thoracic/Head and Neck Medical Oncology, The University of Texas MD Anderson Cancer Center, Houston, TX 77030, USA

<sup>11</sup>Department of Chemistry, Boston University, Boston, MA 02215, USA

<sup>12</sup>Department of Chemical and Systems Biology, Stanford University School of Medicine, Stanford, CA 94305, USA

<sup>13</sup>These authors contributed equally

<sup>14</sup>Lead Contact

\*Correspondence: [pkmazur@mdanderson.org](mailto:pkmazur@mdanderson.org) (P.K.M.), [ogozani@stanford.edu](mailto:ogozani@stanford.edu) (O.G.)

<https://doi.org/10.1016/j.cell.2018.11.038>

## SUMMARY

Increased protein synthesis plays an etiologic role in diverse cancers. Here, we demonstrate that METTL13 (methyltransferase-like 13) dimethylation of eEF1A (eukaryotic elongation factor 1A) lysine 55 (eEF1AK55me<sub>2</sub>) is utilized by Ras-driven cancers to increase translational output and promote tumorigenesis *in vivo*. METTL13-catalyzed eEF1A methylation increases eEF1A's intrinsic GTPase activity *in vitro* and protein production in cells. METTL13 and eEF1AK55me<sub>2</sub> levels are upregulated in cancer and negatively correlate with pancreatic and lung cancer patient survival. METTL13 deletion and eEF1AK55me<sub>2</sub> loss dramatically reduce Ras-driven neoplastic growth in mouse models and in patient-derived xenografts (PDXs) from primary pancreatic and lung tumors. Finally, METTL13 depletion renders PDX tumors hypersensitive to drugs that target growth-signaling pathways. Together, our work uncovers a mechanism by which lethal cancers become dependent on the METTL13-eEF1AK55me<sub>2</sub> axis to meet their elevated protein synthesis requirement and suggests that METTL13 inhibition may constitute a targetable vulnerability of tumors driven by aberrant Ras signaling.

## INTRODUCTION

Lysine methylation is the addition of one, two, or three methyl groups to the  $\epsilon$ -nitrogen of a lysine side chain, forming mono-, di-, and tri-methylated derivatives (referred to here as me<sub>1</sub>, me<sub>2</sub>, and me<sub>3</sub>, respectively). The chemical addition of methyl moieties to lysine residues is catalyzed by lysine methyltransferases (KMTs). Biological functions for lysine methylation is best characterized on histone proteins and the regulation of epigenetics and chromatin biology (Chi et al., 2010). Beyond histones, there is a growing appreciation that a number of non-histone proteins (e.g., p53, RB, RelA) are modulated by lysine methylation (Carlson and Gozani, 2016). In the human proteome, there are predicted to be greater than 100 KMTs that belong to one of two protein methylase families: SET (Su(var)3-9, Enhancer-of-zeste, Trithorax) domain enzymes and 7 $\beta$ S (seven- $\beta$  strand) enzymes (Clarke, 2013). All of the validated histone KMTs reside within the SET domain family with the exception of the H3K79 KMT hDOT1L, which belongs to the 7 $\beta$ S family. Several additional SET and 7 $\beta$ S enzymes methylate non-histone proteins to influence different nuclear and cytoplasmic activities; however, the biological function, catalytic activity, and substrate specificity for the majority of the large family of 7 $\beta$ S KMTs remain to be elucidated (Carlson and Gozani, 2016).

The GTPase eEF1A (eukaryotic elongation factor 1 alpha) is an evolutionarily conserved and fundamental non-ribosomal component of the translational machinery and one of the most abundant proteins found in eukaryotic proteomes (Schuller and Green, 2018). Methylation of eEF1A occurs at several lysine



residues, many of which are conserved from yeast to humans (Hamey and Wilkins, 2018; Jakobsson et al., 2018a). Further, it has been suggested that, akin to the extensive role histone methylation plays in chromatin regulation, eEF1A methylation may likewise regulate distinct eEF1A-mediated biology, including translation elongation. In humans, there are two eEF1A paralogs, eEF1A1 and eEF1A2, which are 90% identical and 98% similar. The expression of eEF1A1 is ubiquitous, while eEF1A2 expression is limited largely to post-mitotic cells (e.g., neurons and cardiomyocytes) (Lee and Surh, 2009). However, eEF1A2 expression is re-activated in cancers, and eEF1A1 levels are generally higher in neoplastic relative to normal tissues (Lee and Surh, 2009). Furthermore, cancers that are driven by PI3K-AKT activation show increased sensitivity to eEF1A inhibitors (Lee and Surh, 2009). Connections between mRNA translation and cancer are well established, whereby it is postulated that alterations in the components of the translation apparatus, including eEF1A1/2 overexpression, may be required to fuel neoplastic growth downstream of oncogenic RAS-MAPK and PI3K-AKT signaling, which frequently drive lethal neoplasms including lung and pancreatic cancer (Bhat et al., 2015; Robichaud et al., 2018; Truitt and Ruggero, 2016).

Lung cancer is the most common cause of global cancer-related mortality, leading to over a million deaths each year, and lung adenocarcinoma (LAC) is the most common histological type. Most LAC cases are due to oncogenic KRAS and/or additional mutations that are to date unfortunately not clinically actionable. Pancreatic cancer is also a lethal malignancy. More than 75% of patients die within the first twelve months of diagnosis; the 5-year survival rate is below 5%. Pancreatic ductal adenocarcinoma (PDAC) is the most prevalent pancreatic cancer subtype. It typically presents at an advanced stage and is refractory to most treatment modalities. The vast majority of PDAC cases express oncogenic mutant KRAS (Almoguera et al., 1988). Due to the lethality of LAC and PDAC, the fundamental role of the KRAS pathway, and the difficulty in directly inhibiting KRAS, drug discovery efforts have turned to inhibiting downstream kinase targets (e.g., RAF, MEK1/2, and ERK1/2) and Ras-activated pathways (e.g., PI3K). While compounds that inhibit these kinases have shown promise in cell-culture and animal experiments, clinical studies have been less encouraging due to toxicity and the development of therapy resistance (Infante et al., 2014). Thus, there is great interest in identifying factors that cooperate with the canonical KRAS pathway to drive cancer with the hope that a therapeutic strategy hitting multiple pathways will hinder resistance development, while also mitigating toxicity by lowering the overall dose needed for each medicine.

In this work, we find that di-methylation of eEF1A at lysine 55 (eEF1AK55me2) is a high stoichiometry species that is upregulated in pancreatic and lung cancers and associated with poor clinical outcomes. In a genetic screen, we identify the orphan protein METTL13 as the physiologic enzyme specifically tasked with generating eEF1AK55me2. Notably, METTL13 expression is also upregulated in cancer wherein it negatively correlates with patient survival. We demonstrate that METTL13, via eEF1AK55 methylation, regulates protein synthesis in cancer cells. Further, METTL13 depletion inhibits proliferation of several cancer cell lines and significantly reduces tumorigenesis *in vivo* in Ras-

driven pancreatic and lung cancer mouse models and in patient-derived xenograft (PDX) models from human pancreatic and lung cancers. Finally, we show that METTL13 depletion markedly sensitizes cancer cells and xenograft tumors to drugs that target growth-signaling pathways. Together, our data support a model in which regulation of translation elongation by the METTL13-eEF1AK55me2 axis serves as a mechanism utilized by malignancies to adapt to their increased translational requirements.

## RESULTS

### Identification of the Orphan Gene METTL13 as a Candidate eEF1A Lysine 55 Dimethyltransferase

The methylation of eEF1A is conserved from yeast to humans, suggesting that, akin to histone methylation, a modification network may regulate specific eEF1A functions (Hamey and Wilkins, 2018; Jakobsson et al., 2018a). While several conserved enzymes that methylate different residues on eEF1A have been identified, the KMT responsible for generating methylation of eEF1A at lysine 55 (eEF1AK55me), a modification that is present in humans but not detected in yeast, is not known (Figure 1A). We analyzed methylation of eEF1A purified from seven cell lines by liquid chromatography-tandem mass spectrometry (LC-MS/MS) and found that >98% of eEF1A1/2 molecules harbor di-methylation at K55, with a small fraction of K55 being unmodified or bearing mono-methylation (Figures 1B, S1A, and S1B). Next, we raised state-specific eEF1AK55me1-3 antibodies and found that each antibody selectively recognized its own state of methylation on eEF1A peptides (Figures 1C and S1C). In addition, the anti-eEF1AK55me2 antibody selectively recognized eEF1AK55me2 peptides, as it did not bind to 19 different peptides from other proteins that harbor a dimethyl lysine (Figure S1D).

To discover the enzyme that generates the eEF1AK55me2 mark, we used a gene-editing coupled biochemical screening strategy (see schematic, Figure 1D). 107 known and putative KMTs in the human genome were identified and a focused CRISPR-Cas9 knockout collection was generated consisting of 3 independent small guide RNAs (sgRNA) per KMT gene and one control sgRNA for a total of 322 sgRNAs (Table S1). The collection was used to generate 322 individual U2OS cell lines, each expressing a single sgRNA from the collection. Lysates were prepared from each individual cell line to generate a collection of 322 unique lysates, which were systematically probed with the eEF1AK55me2 antibody to determine gene(s) whose deletion results in loss of the eEF1A methylation signal (Figure 1D; for control lysate, see Figure S1E). Strikingly, out of the 107 potential KMTs that were targeted by sgRNAs, abrogating *METTL13* expression was the only intervention that reduced eEF1AK55me2 signal (Figures S1E and S1F). Notably, two sgRNAs (*METTL13*-b and -c) reduced *METTL13* protein levels, which was paralleled by a decrease in eEF1AK55me2 signal, whereas cells expressing the *METTL13*-a sgRNA retained *METTL13* expression and failed to reduce eEF1AK55me2 signal (Figure 1E). These results suggest that out of 107 potential KMTs in the human genome, only *METTL13*, an uncharacterized member of the 7βS family, regulates eEF1AK55 dimethylation in U2OS cells.

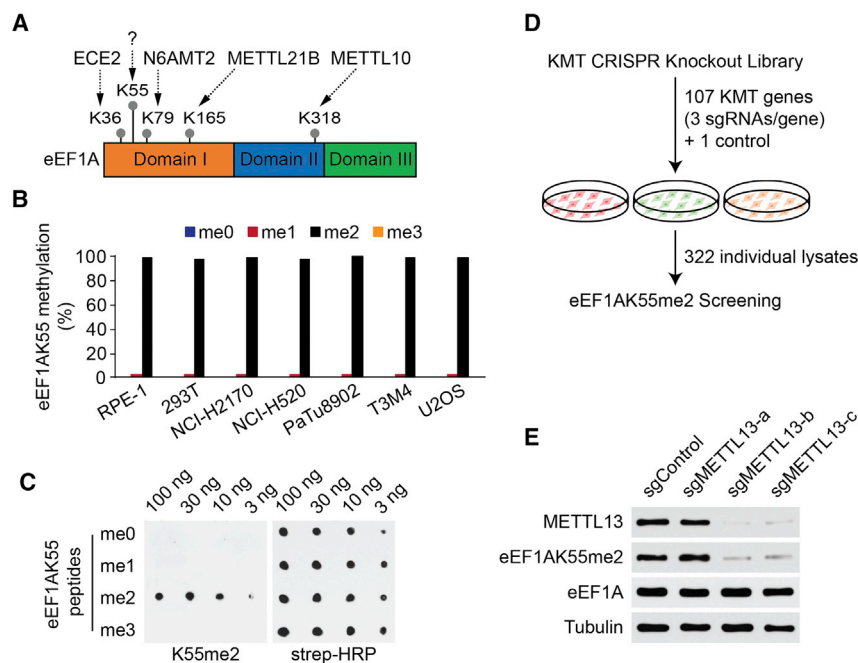


**Figure 1. Identification of METTL13 as a Candidate eEF1A Lysine 55 Methyltransferase**

(A) Schematic of human eEF1A with the indicated major lysine methylation sites and protein domains. Methylated lysine residues are indicated by gray dots. Arrows connect the enzyme responsible for methylation with the indicated lysine residue. The ? indicates that the enzyme for generating K55 methylation is unknown.

(B) eEF1AK55 is primarily di-methylated in human cell lines. Quantitative analysis of endogenous eEF1AK55 methylation levels in the indicated cell lines by mass spectrometry is shown.

(C) Specific recognition of eEF1AK55me2 peptides by the anti-eEF1AK55me2 antibody. Dot-blot analysis with  $\alpha$ eEF1AK55me2 antibody (K55me2) using the indicated biotinylated peptides is shown. Blots probed with horseradish peroxidase (HRP)-conjugated streptavidin (strep-HRP) are shown as loading controls.

(D) Schematic of gene-editing-coupled biochemical screening strategy to discover candidate lysine methyltransferase (KMT)/s responsible for eEF1AK55 methylation. See Table S1 for a list of the 322 sgRNAs.

(E) Identification of METTL13 as a putative eEF1AK55 methyltransferase. Western analysis with

the indicated antibodies of U2OS whole-cell lysates expressing CRISPR-Cas9 and three independent sgRNAs targeting METTL13 (as in Figure S1F) and the control sgRNA (as in Figure S1E) are shown. Total eEF1A levels do not change, and tubulin is shown as a loading control. See also Figure S1 and Table S1.

### The Principal Physiologic Activity of METTL13 Is Generation of eEF1AK55me2

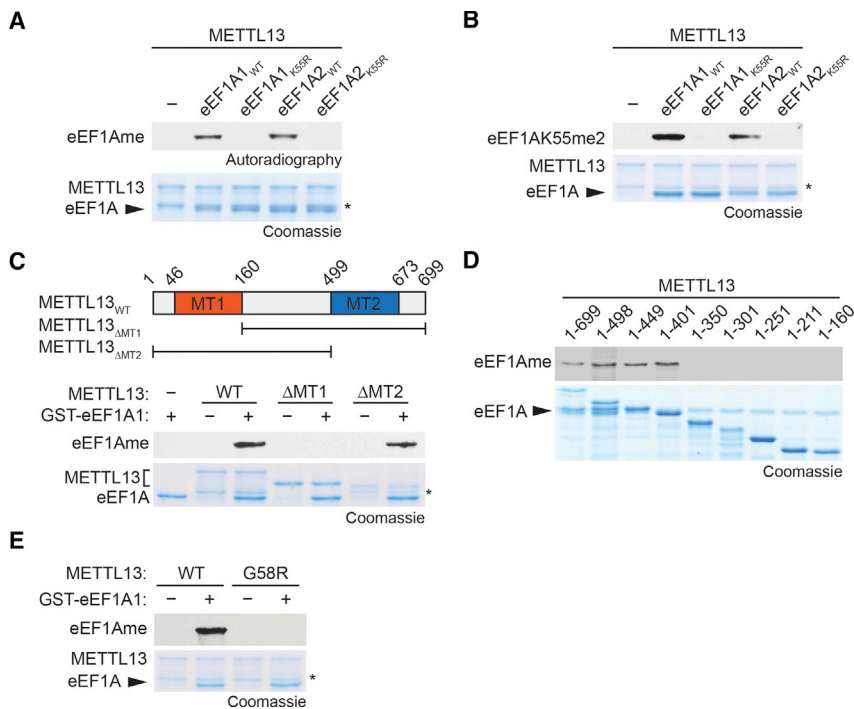
In *in vitro* methylation assays using recombinant proteins with  $^3$ H-SAM (*S*-adenosyl-methionine) as the methyl donor, METTL13 methylated GST-eEF1A1 and GST-eEF1A2, but not eEF1A1/2 proteins harboring a K55R substitution (Figure 2A). We also performed *in vitro* methylation reactions with non-radio-labeled SAM and observed METTL13 mono- and di-methylation (but not tri-methylation) of eEF1A1/2 at K55 by western blotting (Figure 2B) and LC-MS/MS (Figures S2A and S2B).

METTL13 contains two putative methyltransferase (MTase) domains, one at the N terminus and one at the C terminus (top panel, Figure 2C). The N-terminal MTase 1 domain is necessary for METTL13 methylation of GST-eEF1AK55, whereas the C-terminal domain is dispensable for this activity (Figure 2C). Structure-function analysis identified residues 1–401 of METTL13 as sufficient for eEF1AK55 methylation activity, as further C-terminal deletions were not tolerated (Figure 2D). Using a combination of structural modeling (Figure S2C) and sequence homology to other 7 $\beta$ S KMTs (Figure S2D), we identified several specific substitutions that abrogated METTL13's catalytic activity (Figure S2D), including G58R, which is predicted to interfere with SAM binding (Figures 2E and S2C).

In addition to U2OS cells (see Figure 1E), we found that depletion of METTL13 by two independent sgRNAs (targeting exon-intron junctions and named METTL13-1 and METTL13-2) resulted in loss of eEF1AK55me2 in six additional cell lines as determined by western blotting (Figure 3A; LC-MS/MS shown in Figure S3A). Complementation of METTL13-depleted NCI-H2170 cells with CRISPR-resistant wild-type METTL13, but not

the catalytic-dead METTL13<sub>G58R</sub>, restored eEF1AK55me2 levels (Figure 3B). Collectively, these results identify METTL13 as a bona fide KMT that methylates eEF1A at K55 *in vitro* and is required for maintenance of physiologic levels of eEF1AK55me2 in cells in a catalytic activity-dependent manner.

eEF1A is one of the more abundant proteins in the human proteome and K55me2 is a high-stoichiometry event (Hamey and Wilkins, 2018; Jakobsson et al., 2018a) (Figure 1B). Based on our screen (Figure S1F) and cellular depletion studies (Figure 3A), our data argue that METTL13 is the principal enzyme tasked with generating physiologic eEF1AK55me2. This raises the question of whether the converse is true: is eEF1AK55 the only METTL13 substrate or one of many relevant substrates? Histones are heavily methylated and there are many enzymes that function as histone KMTs (Murn and Shi, 2017). However, *in vitro*, METTL13 does not methylate the four core histones (H3, H2A, H2B, and H4) or nucleosomes (Figure 3C). In addition, METTL13 does not methylate any proteins present in the 40S and 60S ribosomal subunits and 80S ribosomes that lack eEF1A (Figures 3D and S3B). To investigate METTL13 catalytic specificity in a physiologic and unbiased setting, we used quantitative proteomics to compare the methylome of the PDAC cell line T3M4  $\pm$  METTL13 (Figure 3E). Of the >1,000 methylation events detected in the analysis, eEF1AK55 methylation (me1 and me2) were the only modifications quantitatively altered upon METTL13 depletion; no changes were observed in histone methylation or for other eEF1A methylated residues (Figure 3E; Table S2). Structural modeling of the METTL13 catalytic core showed a distinct substrate recognition domain (Figure S2C), which is reminiscent of PrmA, a bacterial KMT that achieves substrate specificity



(E) Identification of METTL13 catalytic mutant. *In vitro* methylation assay on GST-eEF1A1 with wild-type METTL13 or METTL13 G58R mutant. Top panel, autoradiogram of methylation assay. Bottom panel, Coomassie stain of proteins in the reaction. See also Figure S2.

through a conformation-specific enzyme-substrate interaction (Demirci et al., 2007). Indeed, METTL13 requires full-length eEF1A and is not active on an eEF1A peptide spanning K55 of eEF1A (Figure S3C), suggesting that it employs a three-dimensional topological substrate recognition mechanism similar to that of PmMA. Taken together, these results indicate that the principal physiologic catalytic activity of METTL13 is eEF1AK55 methylation (see Discussion).

### METTL13 and eEF1AK55me2 Are Highly Expressed in Pancreatic Cancer and Promote Proliferation of Pancreatic Cancer Cells

A meta-analysis of six publicly available human PDAC datasets showed consistent upregulation of *METTL13* mRNA levels and a significant negative correlation between high METTL13 expression and PDAC patient survival (Figures S4A and S4B). Moreover, while METTL13 protein expression was largely undetected by immunohistochemistry (IHC) in the normal pancreas, it was clearly observed in sections from murine and human PDAC samples (Figures 4A and S4C). IHC analysis of eEF1AK55me2 signal also showed a similar pattern, with low signal in normal pancreas and a strong signal in adjacent malignant tissue (Figures 4A and S4C). Further, both METTL13 and eEF1AK55me2 immunostaining signals on PDAC patient tissue arrays showed significant correlation with poor patient survival (Figures 4B and 4C). Similar results were observed for METTL13 expression and eEF1AK55me2 signal in lung cancer (Figures S4D–S4F). Consistent with these results, there is a strong correlation be-

tween METTL13 and eEF1AK55me2 protein levels in both cancer types (Figure 4D). Finally, METTL13 and eEF1AK55me2 (and total eEF1A) levels are all elevated in pancreatic and lung cancer cell lines compared to the non-transformed IMR-90 and RPE-1 cell lines (Figure 4E).

Our observations suggest a potential role for METTL13 and eEF1AK55me2 in oncogenesis. In this regard, depletion of METTL13 had no impact on proliferation of the non-transformed RPE-1 cell line (Figure 4F) but inhibited proliferation of the PDAC T3M4 cell line (Figure 4G) and six additional pancreatic, lung, and other cancer cell lines (Figure S4G). The reduction in proliferation upon METTL13 depletion in T3M4 cells was rescued by complementation with CRISPR-resistant ectopic wild-type METTL13, but not by complementation with catalytically inactive METTL13<sub>G58R</sub> (Figure 4H). Our results implicate METTL13 methylation of eEF1AK55 in PDAC cell proliferation. We next wanted to independently test the role of eEF1AK55 in the regulation of T3M4 cell proliferation. Since the highly abundant eEF1A1 isoform of eEF1A is essential for mRNA translation and eEF1A2 expression is re-activated in cancers, we focused on testing K55 in the context of eEF1A2 function in proliferation. Depletion of eEF1A2 led to a moderate reduction in overall eEF1AK55me2 levels (with the likely remaining signal being chiefly eEF1A1K55me2) and moderately attenuated proliferation of T3M4 cells (Figure 4I). Complementation with wild-type eEF1A2, but not eEF1A2 harboring a K55R substitution (eEF1A2<sub>K55R</sub>), was able to fully restore cancer cell proliferation (Figure 4I). Together these data argue that METTL13 regulates

### Figure 2. *In Vitro* Methylation of eEF1A at Lysine 55 by METTL13

(A) *In vitro* methylation assay with recombinant METTL13 and recombinant wild-type GST-eEF1A1/2 or K55R mutants as indicated. Top panel, <sup>3</sup>H-SAM is the methyl donor and methylation visualized by autoradiography. Bottom panel, Coomassie stain of proteins in the reaction. Asterisks in (A)–(C) and (E) indicate METTL13 breakdown product.

(B) *In vitro* methylation assay as in (A) with non-radiolabeled SAM. Top panel, western analysis with anti-eEF1AK55me2. Bottom panel, Coomassie stain of proteins in the reaction.

(C) The N-terminal MT1 domain of METTL13 is necessary for eEF1AK55 methylation. *In vitro* methylation assay on GST-eEF1A1 with recombinant wild-type METTL13 or the indicated domain deletion fragments. Top panel, schematic diagram of putative methyltransferase (MT) domains of METTL13 and the truncated fragments used in methylation assays. Middle panel, autoradiogram of methylation assay. Bottom panel, Coomassie stain of proteins in the reaction.

(D) Amino acids 1–401 of METTL13 are sufficient for eEF1AK55 methylation. *In vitro* methylation assay on GST-eEF1A1 with wild-type METTL13 or the indicated METTL13 truncated proteins. Top panel, autoradiogram of methylation assay. Bottom panel, Coomassie stain of proteins in the reaction.

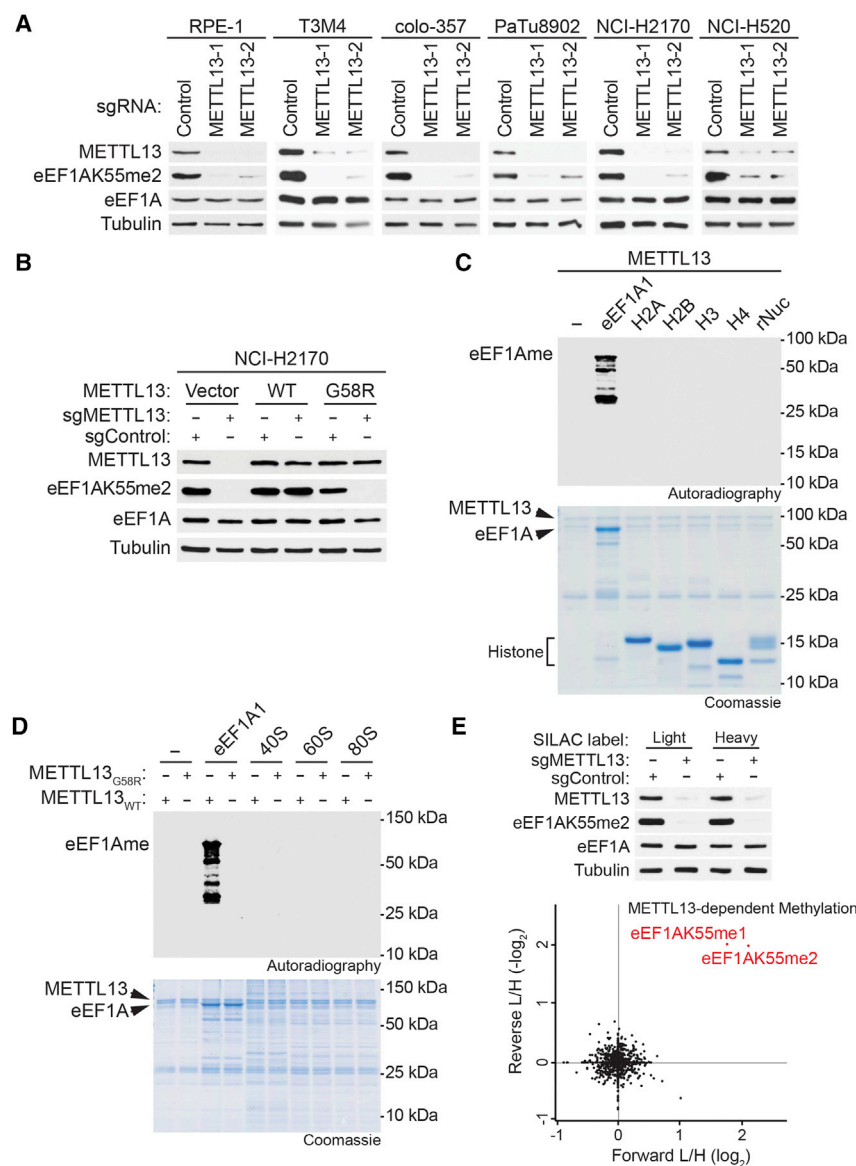


**Figure 3. The Principal Physiologic Activity of METTL3 Is eEF1AK55 Methylation**

(A) METTL3 is required for eEF1AK55 methylation in multiple human cell lines. Western analysis with the indicated antibodies of whole-cell extracts (WCEs) from the indicated cell lines (see STAR Methods) expressing two independent sgRNAs targeting METTL3 or a control sgRNA is shown.

(B) Reconstitution with wild-type METTL3 but not the inactive mutant restores EF1AK55me2 in cells. Western analysis with the indicated antibodies of WCEs from wild-type or METTL3-deficient NCI-H2170 cells complemented with CRISPR-resistant METTL3 (WT or G58R), or control as indicated, is shown.

(C) Histones and nucleosomes are not methylated by METTL3. *In vitro* methylation assay as in Figure 2 on recombinant GST-eEF1A1, core histones (H2A, H2B, H3, and H4), or recombinant nucleosome (rNuc) with METTL3. eEF1A breakdown products containing K55 are seen below full-length with long exposure. Top panel, autoradiogram of methylation assay. Bottom panel, Coomassie stain of proteins in the reaction.

(D) Purified ribosomes are not methylated by METTL3. *In vitro* methylation assay is as in (C) on recombinant GST-eEF1A1, 40S, and 60S ribosomal subunits, and 80S ribosomes isolated from cytoplasmic extracts of T3M4 cells with indicated METTL3 protein.

(E) Methylation of eEF1AK55 is the only change out of >1,000 methylated events detected upon METTL3 depletion in cells. Top panel, western analysis with the indicated antibodies of WCEs maintained in stable isotope labeling by amino acids in cell culture (SILAC) media. Bottom panel, SILAC-based quantitative proteomic analysis of methylated peptides in cells  $\pm$  METTL3. Methylated peptides are plotted by their SILAC ratios in two independent experiments in the forward (x axis) and reverse (y axis) experiments. Any methylated peptide that is dependent upon METTL3 will reside in the top-right quadrant. Of the >1,000 methylated peptides detected in the analysis (see Table S2), only the two eEF1A peptides harboring K55me1 and K55me2 are present in the top-right quadrant as indicated in red. L/H, light over heavy fraction ratio. See also Figure S3 and Table S2.

the proliferation of pancreatic cancer cells via di-methylation of eEF1AK55.

### Methylation Regulates eEF1A GTPase Activity and mRNA Translation in Cells

Since K55 of eEF1A is located on the catalytic surface of the eEF1A GTPase domain, we investigated the possibility that methylation may modulate its GTPase activity. To this end, recombinant FLAG-tagged eEF1A proteins  $\pm$  K55me were purified from either METTL3-overexpressing 293T cells or METTL3-depleted 293T cells expressing METTL3<sub>G58R</sub> (leading to virtually complete loss of K55 methylation) (Figures 5A and S5A). We performed *in vitro* GTP hydrolysis assays to determine Michaelis-Menten kinetic properties of purified eEF1A proteins  $\pm$

K55me2 (Figure S5B). The catalytic efficiency ( $k_{cat}/K_M$ ) of eEF1A was  $\sim$ 20% higher in the K55 methylated state relative to the unmethylated state (Figures 5B and S5B), due to an increase in  $V_{max}$  with no change in the Michaelis constant (Figure 5B). Notwithstanding that K55 dimethylation increased basal GTPase activity of eEF1A, aminoacyl-tRNAs (aa-tRNAs) stimulation of eEF1A GTPase activity did not depend on the K55 methylation status (Cavallius and Merrick, 1998; Van Noort et al., 1986) (Figure S5C). Though upon aa-tRNA stimulation, GTPase activity of K55 dimethylated eEF1A remained higher as compared to K55 methylation deficient eEF1A (Figure S5C). These results suggest that METTL3-dependent eEF1A K55 dimethylation increases its GTPase activity, which may boost translation elongation and thereby increase protein synthesis.

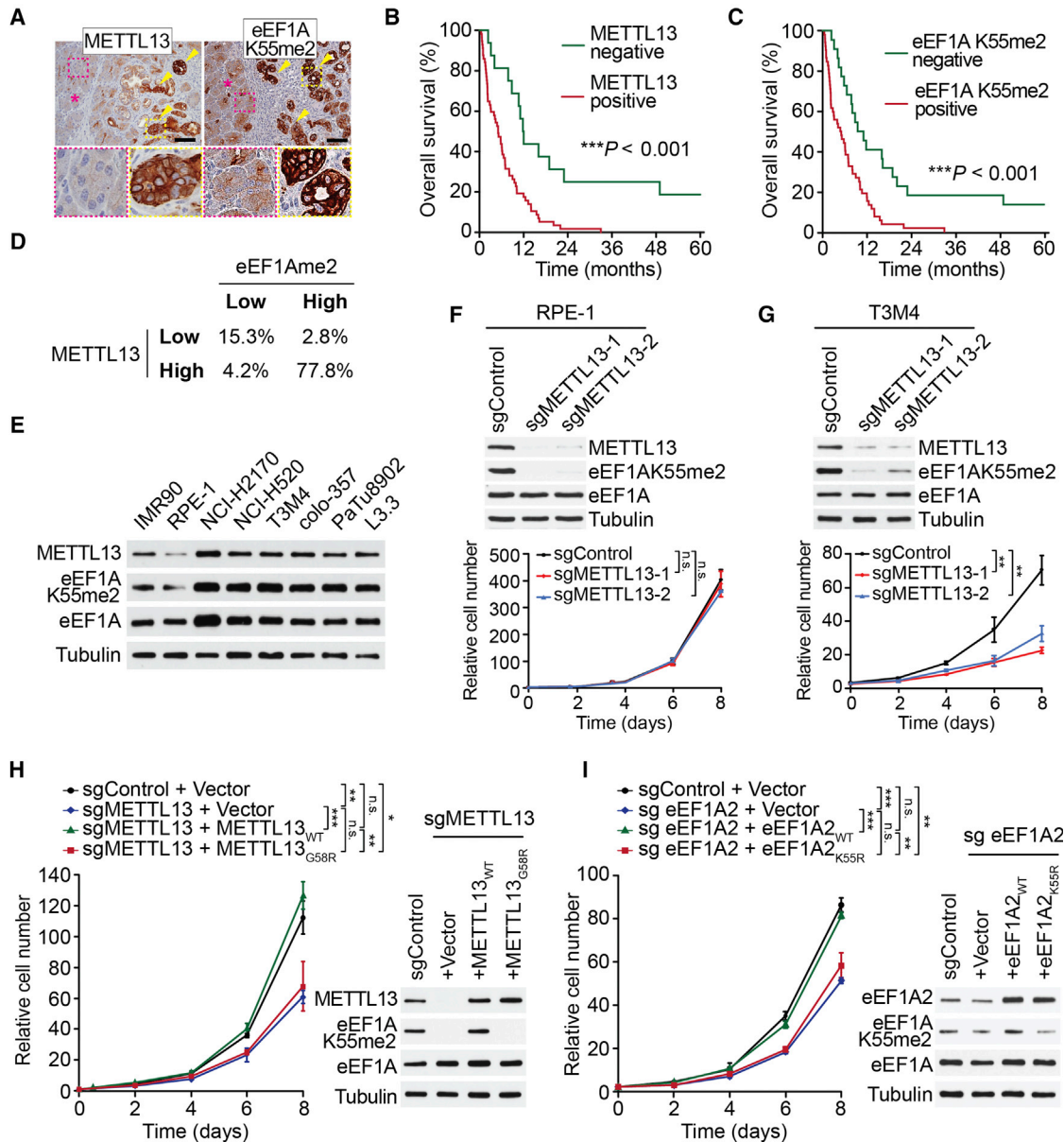


**Figure 4. METTL13 and eEF1AK55me2 Promote Cancer Cell Proliferation**

(A) Representative IHC images showing METTL13 and eEF1AK55me2 expression in pancreatic cancer lesions (arrowheads) but not in adjacent normal acini (asterisk) in human tissue samples (representative of 12 independent samples). Scale bars, 100  $\mu$ m. The area marked with dotted lines is presented at higher magnification in the insets.

(B and C) Analysis of correlation of METTL13 (B) and eEF1AK55me2 (C) staining and PDAC patient survival assessed by IHC.  $***p < 0.001$ , log-rank test, 72 different samples were stained in total for each antibody, a representative staining presented on the right. Scale bars, 100  $\mu$ m.

(D) Correlation analysis of METTL13 and eEF1AK55me2 IHC signal (from B and C; **Figures S4E and S4F**). Spearman correlation  $r = 0.715$ ,  $p$  value  $< 0.0001$ , data presented as percentage of samples in each category (see **STAR Methods**).

(E) Upregulation of METTL13 expression and eEF1AK55me2 levels in pancreatic and lung cancer cells compared to non-transformed cell lines. Western analysis with the indicated antibodies of WCEs from the indicated cell lines. IMR90 are normal human fibroblasts, RPE-1 are immortalized non-transformed human epithelial cells. Tubulin is shown as a loading control.

(F and G) METTL13 depletion inhibits cell proliferation in a PDAC cell line but not in non-transformed cells. Western analysis (top panel) of WCEs and cell proliferation rates (bottom panel) of the non-transformed cell line RPE-1 (F) and human PDAC cell line T3M4 (G) expressing two independent METTL13 sgRNAs or a control sgRNA are shown. Error bars represent SD from three independent experiments.  $**p < 0.01$ , n.s., not significant, two-tailed unpaired Student's  $t$  test.

(H) METTL13 catalytic activity is required for METTL13-dependent proliferation of T3M4 cells. Western analysis and cell proliferation rates as in (G) of control or METTL13-depleted T3M4 cells complemented with CRISPR-resistant METTL13<sub>WT</sub>, METTL13<sub>G58R</sub>, or control are shown. Error bars represent SD from three independent experiments.  $*p < 0.05$ ,  $**p < 0.01$ ,  $***p < 0.001$ , n.s., not significant, two-tailed unpaired Student's  $t$  test.

(legend continued on next page)

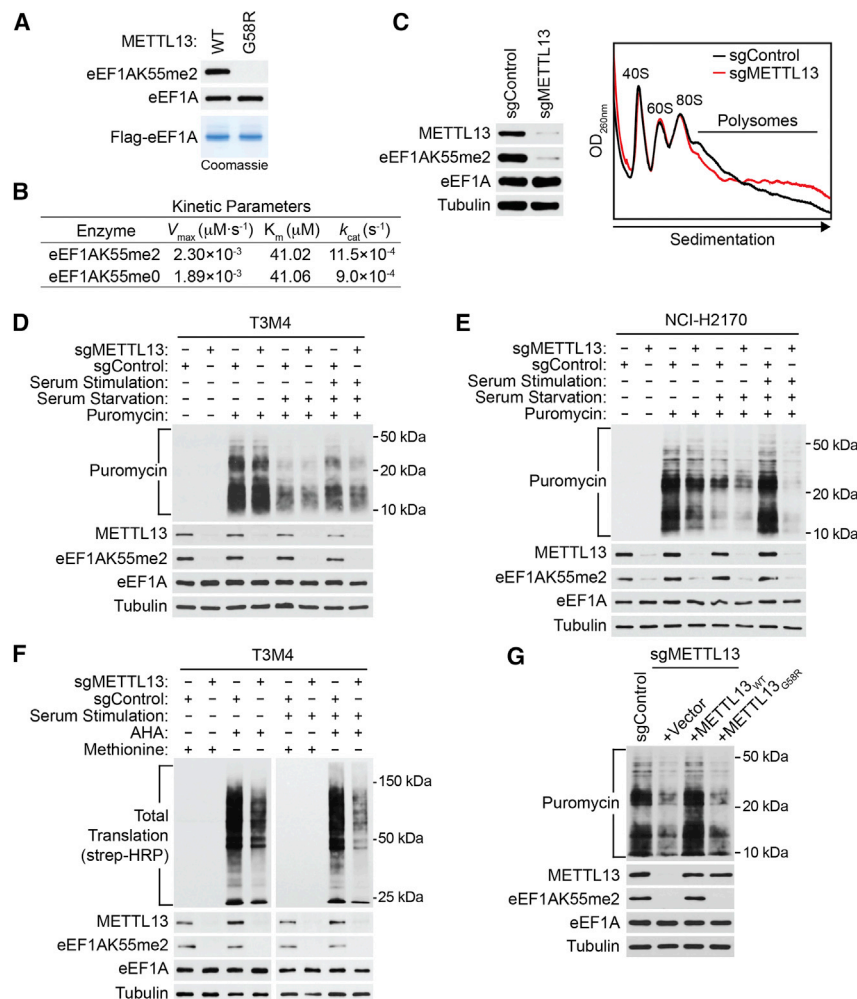


**Figure 5. METTL13-Mediated eEF1AK55 Di-methylation Enhances Protein Synthesis in Cells**

(A) Purification of recombinant eEF1A1  $\pm$  K55me2. Top and middle panels, western analysis with the indicated antibodies of eEF1A purified from 293T cells  $\pm$  catalytically active METTL13 as indicated. Bottom panel, Coomassie stain of purified eEF1A1. (B) K55me2 increases the catalytic efficiency of GTP hydrolysis by eEF1A. The Michaelis-Menten kinetic parameters of FLAG-eEF1A1  $\pm$  K55me2 purified from (A) are shown.

(C) Cytosolic extracts were isolated from control or METTL13-depleted T3M4 cells and fractionated on 5%–50% sucrose gradients. Absorbance profiles show distribution of 40 and 60S ribosomal subunits, 80S monosome, and polysomes.  $OD_{260nm}$ , optical density at 260 nm. Left panel, western analysis represents WCEs from the indicated cell lines used for the polysome profiling are shown. (D and E) SUnSET assays under the indicated conditions reveal reduced protein production in METTL13-depleted T3M4 (D) and NCI-H2170 (E) cells. WCEs were isolated and probed the indicated antibodies.

(F) AHA labeling under the indicated conditions shows decrease in protein synthesis upon depletion of METTL13 in T3M4 cells. WCEs of T3M4 probed with the indicated antibodies are shown. (G) METTL13's catalytic activity is required for enhanced protein synthesis in cells. SUnSET assays as in (D) of control (sgControl plus vector control) or METTL13-depleted T3M4 cells complemented with CRISPR-resistant METTL13<sub>WT</sub>, METTL13<sub>G58R</sub>, or control as indicated and after recovery from serum starvation are shown. WCEs were isolated and probed the indicated antibodies.

See also [Figure S5](#).

To analyze the impact of eEF1AK55me2 depletion on mRNA translation, we performed polysome profiling experiments on extracts from T3M4 cells  $\pm$  METTL13 ([Gandin et al., 2014](#)). An accumulation of heavy polysomes and a decrease in light polysomes were observed in cells depleted of METTL13 relative to control cells ([Figures 5C and S5D](#)). An elevated heavy-to-light polysome ratio may reflect (1) increase in translation initiation, which results in an engagement of a higher number of ribosomes into polysomes thereby suggesting upregulation of protein synthesis, or (2) downregulation of protein synthesis due to the reduction in elongation rates, which lead to protracted occupancy and stalling of polysomes on mRNA. Since these scenarios are expected to have opposing effects on mRNA translation rates, we directly measured protein synthesis using surface sensing of translation (SUnSET) (a method for moni-

toring global protein synthesis through detection of puromycin-labeled neosynthesized proteins [[Schmidt et al., 2009](#)]), in pancreatic (T3M4) and lung (NCI-H2170) cancer cell lines  $\pm$  METTL13 ([Figures 5D and 5E](#)). In both cancer cell lines, METTL13 depletion decreased global protein synthesis, which was most evident after serum re-feeding of serum-starved cells wherein protein synthesis is acutely stimulated. In contrast, METTL13 depletion had no impact on global protein synthesis in the non-transformed RPE-1 cell line irrespective of conditions ([Figure S5E](#)). To avoid potential biases associated with puromycylation approaches, we pulsed cells with the methionine analog L-azidohomoalanine (AHA) ([Iwasaki and Ingolia, 2017](#)). When incorporated into newly synthesized proteins, the analog can be detected with streptavidin by first clicking the azide group of AHA to biotin-alkyne. The AHA incorporation

(I) Role for intact K55 on eEF1A2 in promoting T3M4 proliferation. Western analysis and cell proliferation rates as in (G) of eEF1A2-depleted T3M4 cells complemented with CRISPR-resistant eEF1A2<sub>WT</sub>, eEF1A2<sub>K55R</sub>, or control. Error bars represent SD from three independent experiments. \*\* $p < 0.01$ , \*\*\* $p < 0.001$ , n.s., not significant, two-tailed unpaired Student's t test.

See also [Figure S4](#).

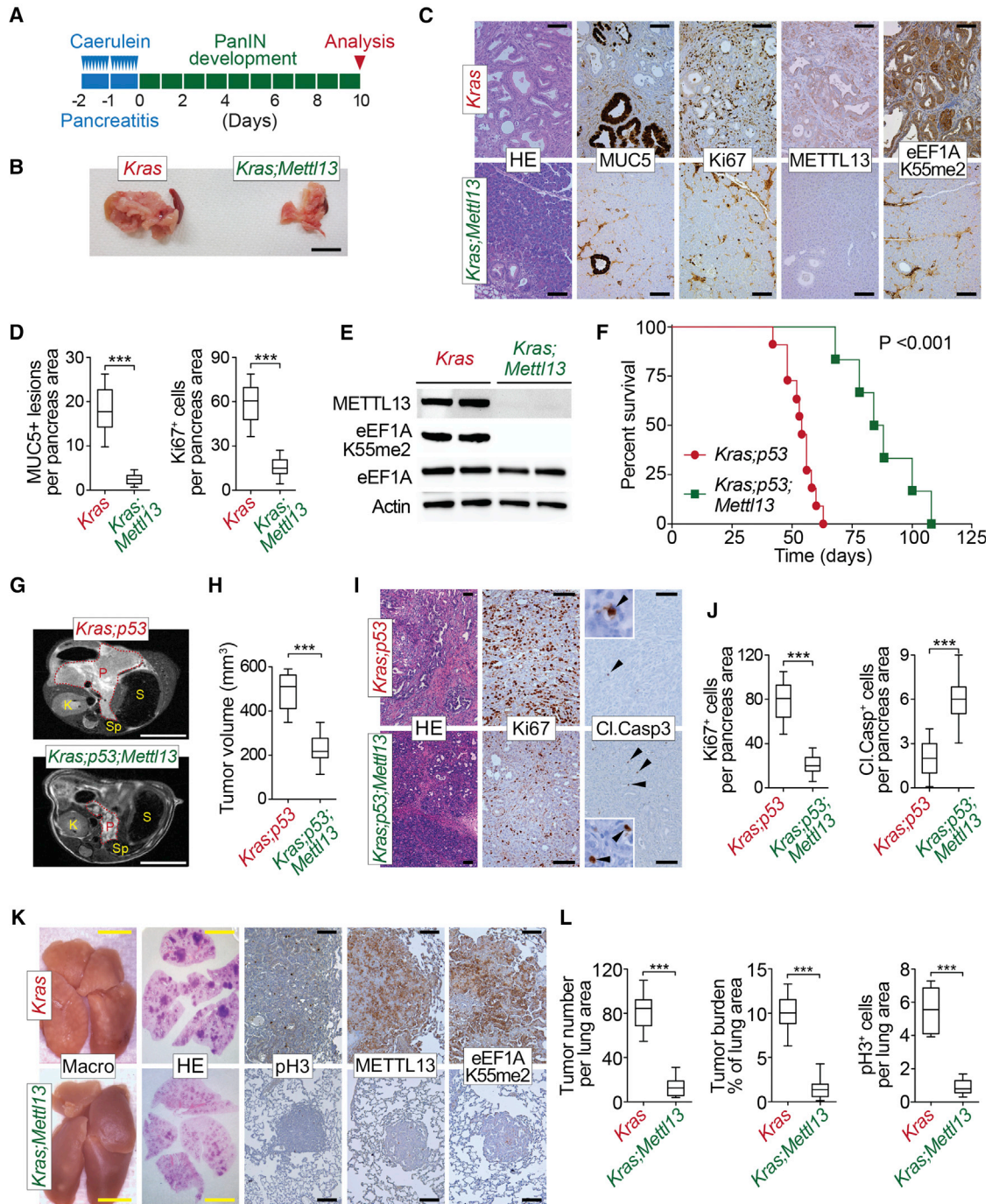


**Figure 6. METTL13 Deletion Represses KRAS-Driven Pancreatic and Lung Tumorigenesis In Vivo**

(A) Schematic of the caerulein pancreatitis-induced precancerous (PanINs) lesion formation protocol used in *Kras;Mettl13* and *Kras* (control) mice.

(B) Representative examples of pancreata gross images (representative of 12 independent samples). Scale bar, 1 cm.

(C) Representative H&E staining and IHC for MUC5, a marker of PanIN lesions, Ki67, a marker of cell proliferation, METTL13, and eEF1AK55me2 (representative of 12 independent samples). Scale bars, 100  $\mu$ m.

(D) Quantification of Ki67-positive proliferating cell and MUC5-positive lesions in caerulein-treated pancreata from *Kras* control (n = 12) and *Kras;Mettl13* (n = 12). \*\*\*p < 0.001, two-tailed unpaired Student's t test. Data are represented as mean  $\pm$  SEM.

(E) Westerns with the indicated antibodies of pancreatic tissue lysates from *Kras;Mettl13* and *Kras* (control) mutant mice (two independent and representative samples are shown for each genotype).

(F) Kaplan-Meier survival curves of *Kras;p53* control mice (n = 10, median survival = 54 days) and *Kras;p53;Mettl13* mutant mice (n = 6, median survival = 86 days). \*\*\*p < 0.001, log-rank test for significance.

(legend continued on next page)

assays mirrored results obtained by SUnSET in T3M4 cells (Figure 5F). Moreover, reconstitution of METTL13-depleted T3M4 cells with wild-type METTL13 restored protein synthesis levels to those observed in the control, whereas complementation with catalytic-dead METTL13<sub>G58R</sub> failed to do so (Figure 5G). Finally, depletion of eEF1A1 and eEF1A2, which as expected resulted in decreased protein synthesis of serum-stimulated cells, was partially rescued by complementation with wild-type eEF1A2, but not with the K55R eEF1A2 mutant (Figure 5F). These data suggest that consistent with its effect on proliferation, eEF1AK55 methylation by METTL13 stimulates protein synthesis in pancreatic cancer cells.

### METTL13 Ablation Inhibits Ras-Driven Tumorigenesis

METTL13 and eEF1AK55me2 levels negatively correlate with PDAC patient survival, while stimulating processes required for neoplastic growth (i.e., protein synthesis and proliferation). To directly test the role of METTL13 in Ras-driven PDAC, we first generated conditional *Mettl13*<sup>loxP/loxP</sup> mutant mice, which develop normally, are viable, and fertile (Figures S6A and S6B). Deletion of *Mettl13* specifically in the pancreas of mice using a pancreas-specific Cre-recombinase expressing strain *Ptf1a*<sup>Cre/+</sup> (Kawaguchi et al., 2002) resulted in no apparent developmental consequences and no evident physiological defects (data not shown).

Acinar-to-ductal metaplasia (ADM) is an early step in PDAC initiation triggered by KRAS-activating mutations (Crawford et al., 2002; Kanda et al., 2012). Using an *ex vivo* 3D culture system in which EGF-stimulated RAS activation induces ADM (Guerra et al., 2003; Zhu et al., 2007), as well as *Mettl13* expression (Figure S6B), we found that *Mettl13* deletion inhibited the appearance of duct-like structures (Figures S6C–S6E). To further investigate the role of METTL13 in KRAS-driven PDAC, *Mettl13* mutant mice were crossed to mice harboring a *loxP*-Stop-*loxP* *Kras*<sup>G12D</sup> knockin allele (*Kras*<sup>LSL-G12D/+</sup>, hereafter *Kras*) (Hingorani et al., 2003), which allows for the controlled induction of oncogenic KRAS and the initiation of cancer. *In vivo*, ADM and PDAC initiation can be triggered in young *Kras* mutant mice by inducing severe acute pancreatitis via repeated injections of caerulein (Lee and Bar-Sagi, 2010; Morris et al., 2010) (see schematic, Figure 6A). In this system, deletion of *Mettl13*, which led to complete loss of eEF1AK55me2 (Figures 6C and 6E), greatly reduced the appearance of pancreatic intra-epithelial neoplasia (PanIN) brought on by *Kras* activation (Figure 6D), as assessed by histopathological analysis and decreased signals for MUC5 (a marker of PanINs) and Ki67 (proliferation marker) (Figures

6B–6E). These data suggest that METTL13 is required for efficient initiation of pancreatic cancer by oncogenic KRAS.

To study pancreatic tumor development and to perform survival studies, we used the *Ptf1a*<sup>+Cre</sup>;*Kras*<sup>+LSL-G12D</sup>;*p53*<sup>loxP/loxP</sup> (*Kras*;*p53*) mutant model in which PDAC develops with 100% penetrance 6–8 weeks after birth (Bardeesy et al., 2006). In this aggressive malignancy model, *Mettl13* deletion extended median survival by 60% relative to controls—from 54 days to 86 days (Figure 6F). Accordingly, MRI revealed that tumor volumes in *METTL13* knockouts were roughly reduced by 2/3 as compared to the age-matched control mice (Figures 6G and 6H) (Mazur et al., 2015). Finally, at autopsy, pancreatic tissue from *Kras*;*p53* mutant mice is entirely occupied by transformed cells, whereas in *Kras*;*p53*;*Mettl13* mutant mice areas of normal pancreatic tissue remain with overall decreased proliferation (Ki67) (Figures 6I and 6J). Together these data support a key *in vivo* role for METTL13 in oncogenic KRAS-driven pancreatic tumorigenesis.

METTL13 and eEF1A are also potentially involved in LAC (Figures S4D–S4F), a cancer in which Ras is frequently activated (Cancer Genome Atlas Research Network, 2014). We tested METTL13 function in LAC by intratracheal injection of an adenovirus expressing the Cre recombinase (Ad-Cre) in adult *Kras*<sup>+LSL-G12D</sup> (*Kras*) and *Kras*<sup>+LSL-G12D</sup>;*Mettl13*<sup>loxP/loxP</sup> (*Kras*;*Mettl13*) mice. As expected *Kras* mutant mice developed widespread adenocarcinoma at 16 weeks after Ad-Cre infection (Jackson et al., 2001; Johnson et al., 2001), which was clearly visible at the whole organ level and by histopathology (Figure 6K). Strikingly, this was paralleled by the upregulation of METTL13 and eEF1AK55me2 (Figure 6K). In contrast, *Kras*;*Mettl13* mutant mice, which are devoid of eEF1AK55me2 (Figure 6K), tumor development was dramatically attenuated based on gross observation, quantification of tumor number and burden, and cell proliferation analysis by phospho-Histone H3 immunostaining (Figures 6K–6L). Of note, a substantial fraction of tumors that emerged in the LAC model retained METTL13 expression and eEF1A methylation as assessed by IHC, suggesting incomplete bi-allelic Cre recombination in these clonal growths (Figure S6F) (Jackson et al., 2001; Liu et al., 2010). Together, these *in vivo* data indicate a central role for METTL13 in carcinogenesis of Ras-driven epithelial tumors of the pancreas and lung.

Next, we investigated the role of METTL13-eEF1AK55me2 in human cancers using PDAC and LAC PDX models. First, we performed *ex vivo* complementation to knockdown endogenous METTL13 and deplete eEF1AK55me2 and then reconstituted samples with either wild-type or catalytic-dead METTL13 using

(G) Representative MRI scan in 7<sup>th</sup> week to analyze tumor volume in *Kras*;*p53*;*Mettl13* and *Kras*;*p53* mutant mice. Red dotted lines indicate pancreas area; p, pancreas; S, stomach; K, kidney; Sp, spleen. Scale bars, 1 cm.

(H) Pancreas tumor volume quantification in 7<sup>th</sup> week of age based on MRI scan (detailed procedure in STAR Methods) of *Kras*;*p53*;*Mettl13* and *Kras*;*p53* mice (n = 4, each genotype) \*\*\*p < 0.001, two-tailed unpaired Student's t test. Data are represented as mean ± SEM.

(I) Representative HE and IHC for Ki67 (a marker of proliferation) and Cleaved Caspase 3 (Cl.Casp 3, a marker of apoptosis) in pancreas tumors at autopsy in *Kras*;*p53*;*Mettl13* and *Kras*;*p53* mutant mice. Scale bars, 100 μm, insets magnification ×10.

(J) Quantification of Ki67-positive proliferating cell and Cleaved Caspase 3 apoptotic cells in pancreata at autopsy from *Kras*;*p53* control (n = 6) and *Kras*;*p53*;*Mettl13* (n = 6) mutant mice. \*\*\*p < 0.001, two-tailed unpaired Student's t test. Data are represented as mean ± SEM.

(K) Representative macroscopic picture of lungs, HE staining, and IHC for phospho-Histone H3 (pH3, a marker of proliferation), METTL13, and eEF1AK55me2 (representative of 8 independent samples). Scale bars: yellow, 1 cm; black, 100 μm.

(L) Quantification of tumor number, tumor area (burden), and phospho Histone H3-positive (pH3<sup>+</sup>) proliferating cells per lung area in *Kras* control (n = 8) and *Kras*;*Mettl13* (n = 8). \*\*\*p < 0.001, two-tailed unpaired Student's t test. Data are represented as mean ± SEM.

See also Figure S6.

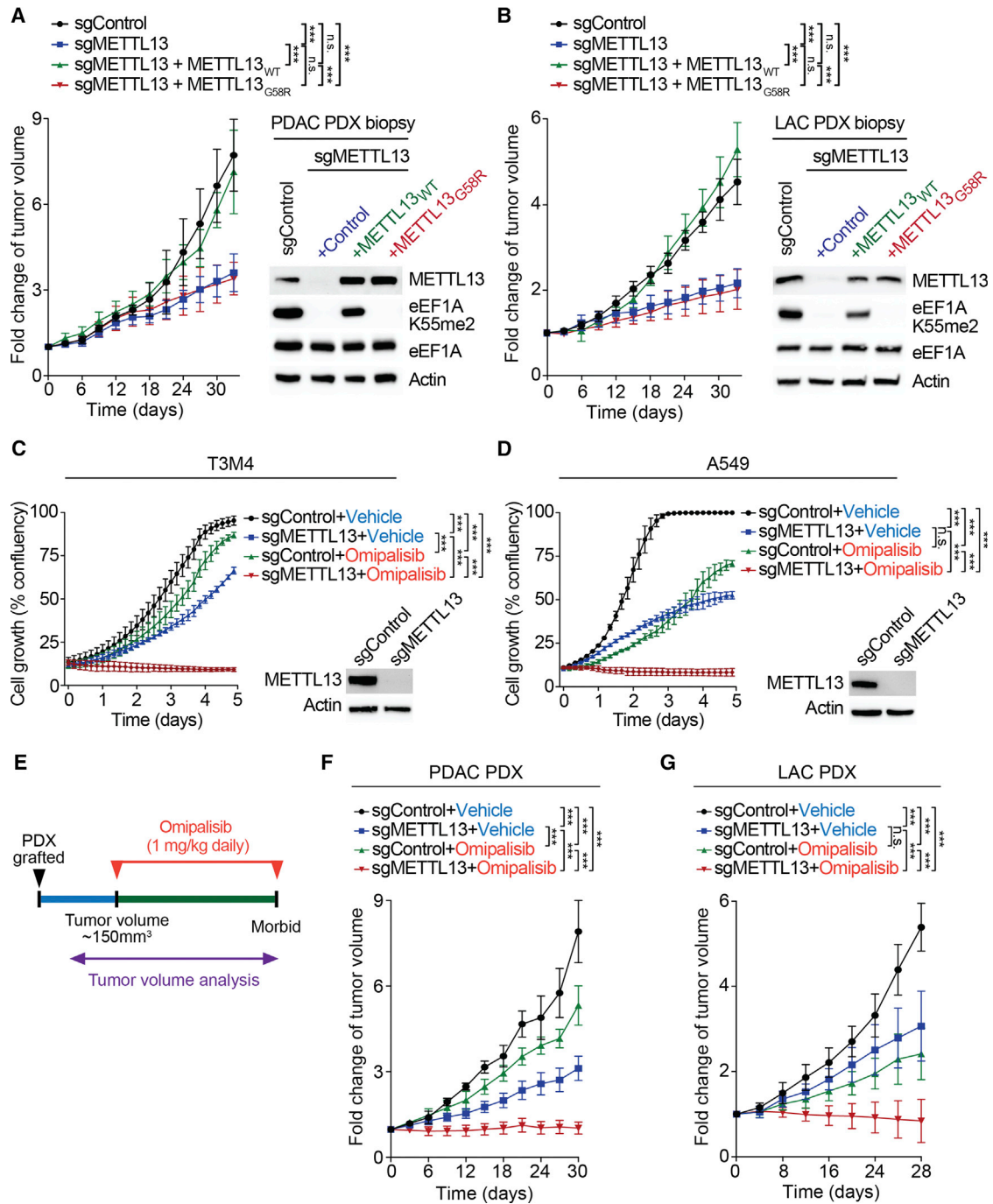


**Figure 7. Depletion of METTL13's Catalytic Activity Inhibits Growth of Pancreatic and Lung Cancer PDX Tumors *In Vivo* and Regression of PDX Tumors by METTL13 Depletion and PI3K and mTOR Inhibitors**

(A) Tumor volume quantification for patient-derived PDAC xenografts modified to express sgRNA METTL13 or sgRNA control and overexpressing METTL13<sub>WT</sub> or catalytically deficient METTL13<sub>G58R</sub> in mice (n = 8 mice for each treatment group). \*\*\*p < 0.001, two-tailed unpaired Student's t test. Data are represented as mean ± SEM. Westerns with the indicated antibodies of patient-derived xenograft (PDX) biopsies (one representative sample for each condition is shown).

(B) Tumor volume quantification for patient-derived lung adenocarcinoma (LAC) xenografts modified to express sgRNA METTL13 or sgRNA control and overexpressing METTL13<sub>WT</sub> or METTL13<sub>G58R</sub> in mice (n = 8 mice for each treatment group). \*\*\*p < 0.001, two-tailed unpaired Student's t test. Data are represented as mean ± SEM. Westerns with the indicated antibodies of PDX biopsies (one representative sample for each condition) are shown.

(C) Population growth of T3M4 pancreatic cancer cell line depleted for METTL13 by CRISPR-Cas9 sgRNA (sgMETTL13) or control (sgControl). Confluency of cells over 96 hr treated with Omipalisib (1 μM) or placebo (vehicle). \*\*\*p < 0.001, two-tailed unpaired Student's t test. Data are represented as mean ± SEM (three independent experiments). Westerns of WCEs with the indicated antibodies are shown.

(legend continued on next page)

multiple independent PDXs from both cancers types (Figures 7A, 7B, S7A, and S7B). The depletion of METTL13 attenuated xenograft tumor growth in both PDAC and LAC models (Figures 7A, 7B, S7A, and S7B). Complementation with wild-type METTL13, which restored eEF1AK55me2 levels close to the levels of control cells, also reestablished tumor growth (Figures 7A, 7B, S7A, and S7B). In contrast, reconstitution with METTL13<sup>G58R</sup> did not rescue tumor growth (Figures 7A, 7B, S7A, and S7B). These data suggest that the pro-tumorigenic functions of METTL13 require its catalytic activity.

A feature of cancers triggered by oncogenes such as KRAS is upregulation of protein synthesis (Bhat et al., 2015; Robichaud et al., 2018; Truitt and Ruggero, 2016). We postulated that one mechanism by which this may be achieved is through the METTL13-eEF1AK55me2 axis. This led us to speculate that inhibiting METTL13 may cooperate with compounds targeting growth signaling, which renders malignant cells addicted to increased protein synthesis. To test this idea, a comparative cell-based screen using a library assembled of 285 characterized inhibitors covering ~170 cancer targets (Table S3) was performed to identify drugs that have increased efficacy against T3M4 pancreatic cancer cells in the absence of METTL13. Twelve drugs elicited a 50% increase in synthetic lethality when combined with METTL13 depletion (Table S3); these drugs predominantly inhibit the PI3K-mTOR and MAPK pathways (e.g., Omipalisib, Dactolisib, and Trametinib). Relative to control, treatment of pancreatic (T3M4) and lung (A459) cancer cells with the dual pan-PI3K and mTOR inhibitor Omipalisib or METTL13 depletion had modest effects on proliferation, and the combination of Omipalisib treatment with METTL13 depletion prevented both cell types from growing (Figures 7C and 7D). To test whether this synergy occurs in an *in vivo* context, PDX tumors ± METTL13 depletion were treated with Omipalisib, and tumor growth was monitored (Figure 7E). Notably, PDAC and LAC PDX tumor growth stalled or regressed in size by the combination treatment (Figures 7F, 7G, S7C, and S7D). Based on our results, we postulate that eEF1AK55 methylation by METTL13 constitutes a hitherto unappreciated mechanism required by neoplasms driven by KRAS pathways to meet their increased protein synthesis requirements (Chio et al., 2016; Martineau et al., 2014; Ruggero et al., 2004). These data also suggest that the METTL13-eEF1AK55me2 axis may constitute a clinically targetable vulnerability of cancers driven by aberrant growth signaling.

## DISCUSSION

In a screen of 107 potential KMTs, we identified METTL13 as an active enzyme that specifically di-methylates the elongation fac-

tor eEF1A at lysine 55. Based on both depletion and reconstitution experiments in multiple independent cell lines, including primary pancreatic and lung cancer lines, as well as mouse tissue knockouts, we propose that METTL13 is the principal enzyme tasked with generating physiologic eEF1AK55me2. Another functionally important question we address is whether METTL13 has other lysine substrates besides eEF1AK55, particularly in the context of METTL13-associated translation regulation and cancer phenotypes. METTL13 does not methylate histones or any of the proteins stably associated with the 40S and 60S ribosomal subunits or 80S ribosomes. Moreover, eEF1AK55 methylation was the only observed change out of >1,000 detected methylation events in cells depleted of METTL13. Consistently with the crucial role of eEF1A1/2 proteins in translation elongation and the pivotal role of protein synthesis in stimulating cell division (Brooks, 1977), we also observed a role for K55 of eEF1A2 in increasing proliferation of pancreatic cancer cells. Together, these findings, in combination with the expression patterns of METTL13 and eEF1AK55me2 in cancer, support our hypothesis that the biological and pathologic functions of METTL13 reported here are mediated through eEF1AK55 methylation. Further support comes from a recently published study that independently identified eEF1AK55 to be specifically methylated by METTL13 (Jakobsson et al., 2018b).

In the methylation of histones, several KMTs are highly selective enzymes with a single physiologic substrate (Carlson and Gozani, 2016); for example, the 7βS KMT hDOT1L recognizes a specific topology (the nucleosome) to methylate a single lysine (H3K79). As with histones, there are several KMTs—including METTL13—that are devoted to methylating distinct lysines on eEF1A (Hamey and Wilkins, 2018; Jakobsson et al., 2018a). At chromatin, methylation dynamics are regulated not only by KMTs, but also by lysine demethylases and specific methyl-lysine “reader” domains, which together have a major impact in fine-tuning histone functions. We postulate that similar mechanisms are at play in the regulation of translation, and that eEF1A demethylases and readers will soon be identified. Future work may also uncover crosstalk between eEF1AK55 methylation and other eEF1A modifications in the regulation of translation elongation in diverse settings including human disease. Finally, it will also be interesting to explore potential roles for K55me2 in regulating non-canonical eEF1A functions such as RNA export, AKT signaling, and degradation of newly synthesized polypeptides (Abbas et al., 2015; Gandin et al., 2013).

Translation is among the most energy-consuming processes in cells, and dysregulation in translation mechanisms is a common etiologic agent in neoplastic diseases (Bhat et al., 2015; Robichaud et al., 2018; Truitt and Ruggero, 2016). Here, we have

(D) Population growth of A549 lung cancer cell line depleted for METTL13 by CRISPR-Cas9 sgRNA (sgMETTL13) or control (sgControl) as in (C). \*\*\*p < 0.001, two-tailed Student's t test. Data are represented as mean ± SEM (three independent experiments). Westerns of WCEs with the indicated antibodies are shown.

(E) Treatment schedule for administration of Omipalisib (GSK2126458, 1 mg kg<sup>-1</sup>, intraperitoneal injection once daily) to immunocompromised mice grafted with PDX pancreatic (see F) or lung cancer (see G). Control mice received placebo (vehicle). Treatment started when tumors were around 150 mm<sup>3</sup>.

(F and G) Tumor volume quantification for patient-derived PDAC (F) and LAC (G) xenografts modified to express sgRNA METTL13 or sgRNA control treated with placebo (vehicle) or Omipalisib. Plots showing fold change in tumor volume compared to initial tumor volume. \*\*\*p < 0.001, n.s., not significant, two-tailed unpaired Student's t test. Data are represented as mean ± SEM.

See also Figure S7 and Table S3.

provided evidence for a model in which METTL13-mediated methylation of eEF1A increases translation elongation and enhances protein synthesis to promote oncogenesis (see [Figure S7E](#)). METTL13 and eEF1AK55me2 protein levels are higher in transformed versus non-transformed cells, and higher in malignant Ras-driven pancreatic and lung cancer tissue relative to adjacent normal tissue. Consistently, increased expression of eEF1A1/2 is frequent in malignancies ([Lee and Surh, 2009](#)). Deletion of METTL13 profoundly inhibited the ability of oncogenic Ras to drive the development of pancreatic and lung cancers *in vivo* and greatly reduced tumor growth in mice of PDX models from primary human pancreatic and lung tumors. In contrast, METTL13 appears to be dispensable for proliferation of non-transformed cells and normal development of the pancreas. In this regard, the paradigm that translational capacity is in excess in normal tissue but becomes restrictive for tumorigenesis was established in mice haploinsufficient for eIF4E ([Truitt et al., 2015](#)). Notably, these mice develop normally, but, like METTL13-deleted mice, Ras-driven tumorigenesis is attenuated in the LAC mouse model ([Truitt et al., 2015](#)); indeed, inhibition of translation initiation with the eIF4A inhibitor SDS-1-021 ([Chu et al., 2016](#)) impacted cancer cells with aberrant Ras signaling but not IMR90 cells ([Figures S7F and S7G](#)). Our results raise the possibility that METTL13-eEF1AK55me2 enhancement of translation elongation becomes rate limiting in growth-signal-driven tumors like PDAC and LAC, which could potentially render these lethal cancers vulnerable to METTL13 inhibition. This is consistent with the findings that the eEF2-dependent modulation of translation elongation rates may play a context-dependent role in determining the fate of cancer cells ([Faller et al., 2015](#); [Leprivier et al., 2013](#)).

In addition to PDAC and LAC, METTL13 depletion attenuated proliferation in two squamous cell lung cancer cell lines (NCI-H2170 and H520) with activated PI3K, suggesting a relatively broad oncogenic role for METTL13. In a focused cell-based small-molecule screen, we identified PI3K inhibitors and several other oncogenic growth pathway inhibitors that selectively cooperate with METTL13 depletion to prevent pancreatic and lung PDX tumor growth. As METTL13 appears to be selectively needed in the transformed cellular state and nonessential in normal tissue, a METTL13 inhibitor, in the context of a combination treatment strategy, may help overcome the narrow therapeutic index of compounds targeting growth signaling (e.g., PI3K) ([Infante et al., 2014](#)). In summary, we have identified METTL13 methylation of eEF1AK55 as a mechanism to regulate translation elongation and promote tumorigenesis. These results identify the METTL13-eEF1AK55me2 axis as a vulnerability of growth-signaling-driven malignancies and provide a molecular basis for the future development of METTL13 inhibitors for the clinic.

## STAR★METHODS

Detailed methods are provided in the online version of this paper and include the following:

- [KEY RESOURCES TABLE](#)
- [CONTACT FOR REAGENT AND RESOURCE SHARING](#)

## ● EXPERIMENTAL MODEL AND SUBJECT DETAILS

- Mice
- Cell Lines
- Human Tumor Samples

## ● METHOD DETAILS

- Pancreatic Cancer Mouse Models
- LAC Mouse Models
- Magnetic Resonance Imaging
- Histology and Immunohistochemistry
- Preparation of Pancreatic Epithelial Explants Culture
- Meta-analysis of Gene Expression
- Patient-derived Cancer Xenografts
- Transfection and Viral Transduction
- Plasmids
- CRISPR-Cas9 Knockout Library Screen
- Immunoblot Analysis and Immunoprecipitation
- Expression and Purification of Recombinant Proteins
- Structural Modeling of METTL13 (1-400)
- Polysome Profiling
- Methylation and GTPase Assays
- Mass Spectrometry of eEF1AK55 Methylation
- Proteome-wide Labeling and Analysis of METTL13 Substrates
- Cell Assays
- Translation Assays

## ● QUANTIFICATION AND STATISTICAL ANALYSIS

## SUPPLEMENTAL INFORMATION

Supplemental Information includes seven figures and three tables and can be found with this article online at <https://doi.org/10.1016/j.cell.2018.11.038>.

## ACKNOWLEDGMENTS

We thank Pål Falnes, Jerry Pelletier, and Julien Sage for helpful discussion, Lauren Brown and William Devine for SDS-1-021, and members of the Gozani and Mazur laboratories for critical reading of the manuscript. This work was supported in part by grants from the NIH to S.M.C. (K99CA190803), M.P.K. (5K08CA218690-02), J.A.P. (R35GM118173), M.C.B. (1DP2HD084069-01), J.S. (1R35GM119721), I.T. (R01CA202021), P.K.M. (R00CA197816, P50CA070907, and P30CA016672), and O.G. (R01GM079641). J.E.E. received support from Stanford ChEM-H, and A.M. was supported by the MD Anderson Moonshot Program. I.T. is a Junior 2 Research Scholar of the Fonds de Recherche du Québec – Santé (FRQ-S). P.K.M. is supported by the Neuroendocrine Tumor Research Foundation and American Association for Cancer Research and is the Andrew Sabin Family Foundation Scientist and CPRIT scholar (RR160078). S.H. is supported by a Deutsche Forschungsgemeinschaft Postdoctoral Fellowship. J.W.F. is supported by 5T32GM007276.

## AUTHOR CONTRIBUTIONS

S.L. and S.H. were responsible for the experimental design, execution, data analysis, and manuscript preparation. M.E.F., J.W.F., and M.C. helped S.L. and S.H. with experimental design and execution. S.L. and R.P. performed the polysome profiling experiments and C.V.R. supervised. L.H., K.T., I.T., and J.A.P. performed SDS-1-021 experiments. N.D.N. contributed to MRI analysis. S.M.L. performed bioinformatic meta-analysis of gene expression and survival. I.I.W. and H.W. performed pathologic and histological analyses. A.M. and M.P.K. provided PDX samples. S.L. performed and analyzed the mass spectrometry experiments, with help from J.E.E.. S.M.C. generated the KMT sgRNA library with help from A.L., and M.C.B. and S.M.C. generated the lysate library. J.L. and J.S. provided the structural model. I.T. helped with

manuscript preparation. O.G. and P.K.M. were equally responsible for supervision of research, data interpretation, and manuscript preparation.

## DECLARATION OF INTERESTS

O.G. is a co-founder of Epiccypher and Athelas Therapeutics.

Received: August 17, 2018

Revised: October 18, 2018

Accepted: November 21, 2018

Published: January 3, 2019

## REFERENCES

- Abbas, W., Kumar, A., and Herbein, G. (2015). The eEF1A proteins: At the crossroads of oncogenesis, apoptosis, and viral infections. *Front. Oncol.* *5*, 75.
- Almoguera, C., Shibata, D., Forrester, K., Martin, J., Arnheim, N., and Perucho, M. (1988). Most human carcinomas of the exocrine pancreas contain mutant c-K-ras genes. *Cell* *53*, 549–554.
- Bardeesy, N., Aguirre, A.J., Chu, G.C., Cheng, K.H., Lopez, L.V., Hezel, A.F., Feng, B., Brennan, C., Weissleder, R., Mahmood, U., et al. (2006). Both p16(Ink4a) and the p19(Arf)-p53 pathway constrain progression of pancreatic adenocarcinoma in the mouse. *Proc. Natl. Acad. Sci. USA* *103*, 5947–5952.
- Bhat, M., Robichaud, N., Hulea, L., Sonenberg, N., Pelletier, J., and Topisirovic, I. (2015). Targeting the translation machinery in cancer. *Nat. Rev. Drug Discov.* *14*, 261–278.
- Brooks, R.F. (1977). Continuous protein synthesis is required to maintain the probability of entry into S phase. *Cell* *12*, 311–317.
- Cancer Genome Atlas Research Network (2014). Comprehensive molecular profiling of lung adenocarcinoma. *Nature* *511*, 543–550.
- Carlson, S.M., and Gozani, O. (2016). Nonhistone lysine methylation in the regulation of cancer pathways. *Cold Spring Harb. Perspect. Med.* *6*. Published online November 1, 2016. <https://doi.org/10.1101/cshperspect.a026435>.
- Cavallius, J., and Merrick, W.C. (1998). Site-directed mutagenesis of yeast eEF1A. Viable mutants with altered nucleotide specificity. *J. Biol. Chem.* *273*, 28752–28758.
- Chi, P., Allis, C.D., and Wang, G.G. (2010). Covalent histone modifications—miswritten, misinterpreted and mis-erased in human cancers. *Nat. Rev. Cancer* *10*, 457–469.
- Chio, I.I.C., Jafarnejad, S.M., Ponz-Sarvise, M., Park, Y., Rivera, K., Palm, W., Wilson, J., Sangar, V., Hao, Y., Öhlund, D., et al. (2016). NRF2 promotes tumor maintenance by modulating mRNA translation in pancreatic cancer. *Cell* *166*, 963–976.
- Chu, J., Cencic, R., Wang, W., Porco, J.A., Jr., and Pelletier, J. (2016). Translation inhibition by rocaglates is independent of eIF4E phosphorylation status. *Mol. Cancer Ther.* *15*, 136–141.
- Clarke, S.G. (2013). Protein methylation at the surface and buried deep: Thinking outside the histone box. *Trends Biochem. Sci.* *38*, 243–252.
- Cox, J., and Mann, M. (2008). MaxQuant enables high peptide identification rates, individualized p.p.b.-range mass accuracies and proteome-wide protein quantification. *Nat. Biotechnol.* *26*, 1367–1372.
- Crawford, H.C., Scoggins, C.R., Washington, M.K., Matrisian, L.M., and Leach, S.D. (2002). Matrix metalloproteinase-7 is expressed by pancreatic cancer precursors and regulates acinar-to-ductal metaplasia in exocrine pancreas. *J. Clin. Invest.* *109*, 1437–1444.
- Demirci, H., Gregory, S.T., Dahlberg, A.E., and Jøgl, G. (2007). Recognition of ribosomal protein L11 by the protein trimethyltransferase PrmA. *EMBO J.* *26*, 567–577.
- Faller, W.J., Jackson, T.J., Knight, J.R., Ridgway, R.A., Jamieson, T., Karim, S.A., Jones, C., Radulescu, S., Huels, D.J., Myant, K.B., et al. (2015). mTORC1-mediated translational elongation limits intestinal tumour initiation and growth. *Nature* *517*, 497–500.
- Gandin, V., Gutierrez, G.J., Brill, L.M., Varsano, T., Feng, Y., Aza-Blanc, P., Au, Q., McLaughlan, S., Ferreira, T.A., Alain, T., et al. (2013). Degradation of newly synthesized polypeptides by ribosome-associated RACK1/c-Jun N-terminal kinase/eukaryotic elongation factor 1A2 complex. *Mol. Cell. Biol.* *33*, 2510–2526.
- Gandin, V., Sikström, K., Alain, T., Morita, M., McLaughlan, S., Larsson, O., and Topisirovic, I. (2014). Polysome fractionation and analysis of mammalian translomes on a genome-wide scale. *J. Vis. Exp.* Published online May 17, 2014. <https://doi.org/10.3791/51455>.
- Guerra, C., Mijimolle, N., Dhawahir, A., Dubus, P., Barradas, M., Serrano, M., Campuzano, V., and Barbacid, M. (2003). Tumor induction by an endogenous K-ras oncogene is highly dependent on cellular context. *Cancer Cell* *4*, 111–120.
- Hamey, J.J., and Wilkins, M.R. (2018). Methylation of elongation factor 1A: Where, who, and why? *Trends Biochem. Sci.* *43*, 211–223.
- Hingorani, S.R., Petricoin, E.F., Maitra, A., Rajapakse, V., King, C., Jacobetz, M.A., Ross, S., Conrads, T.P., Veenstra, T.D., Hitt, B.A., et al. (2003). Preinvasive and invasive ductal pancreatic cancer and its early detection in the mouse. *Cancer Cell* *4*, 437–450.
- Infante, J.R., Somer, B.G., Park, J.O., Li, C.P., Scheulen, M.E., Kasubhai, S.M., Oh, D.Y., Liu, Y., Redhu, S., Steplewski, K., and Le, N. (2014). A randomised, double-blind, placebo-controlled trial of trametinib, an oral MEK inhibitor, in combination with gemcitabine for patients with untreated metastatic adenocarcinoma of the pancreas. *Eur. J. Cancer* *50*, 2072–2081.
- Iwasaki, S., and Ingolia, N.T. (2017). The growing toolbox for protein synthesis studies. *Trends Biochem. Sci.* *42*, 612–624.
- Jackson, E.L., Willis, N., Mercer, K., Bronson, R.T., Crowley, D., Montoya, R., Jacks, T., and Tuveson, D.A. (2001). Analysis of lung tumor initiation and progression using conditional expression of oncogenic K-ras. *Genes Dev.* *15*, 3243–3248.
- Jakobsson, M.E., Matecki, J., and Falnes, P.O. (2018a). Regulation of eukaryotic elongation factor 1 alpha (eEF1A) by dynamic lysine methylation. *RNA Biol.* *15*, 314–319.
- Jakobsson, M.E., Matecki, J.M., Halabelian, L., Nilges, B.S., Pinto, R., Kudithipudi, S., Munk, S., Davydova, E., Zuhairi, F.R., Arrowsmith, C.H., et al. (2018b). The dual methyltransferase METTL13 targets N terminus and Lys55 of eEF1A and modulates codon-specific translation rates. *Nat. Commun.* *9*, 3411.
- Johnson, L., Mercer, K., Greenbaum, D., Bronson, R.T., Crowley, D., Tuveson, D.A., and Jacks, T. (2001). Somatic activation of the K-ras oncogene causes early onset lung cancer in mice. *Nature* *410*, 1111–1116.
- Kanda, M., Matthaehi, H., Wu, J., Hong, S.M., Yu, J., Borges, M., Hruban, R.H., Maitra, A., Kinzler, K., Vogelstein, B., et al. (2012). Presence of somatic mutations in most early-stage pancreatic intraepithelial neoplasia. *Gastroenterology* *142*, 730–733.
- Kawaguchi, Y., Cooper, B., Gannon, M., Ray, M., MacDonald, R.J., and Wright, C.V. (2002). The role of the transcriptional regulator Ptf1a in converting intestinal to pancreatic progenitors. *Nat. Genet.* *32*, 128–134.
- Lee, K.E., and Bar-Sagi, D. (2010). Oncogenic KRas suppresses inflammation-associated senescence of pancreatic ductal cells. *Cancer Cell* *18*, 448–458.
- Lee, M.H., and Surh, Y.J. (2009). eEF1A2 as a putative oncogene. *Ann. N Y Acad. Sci.* *1171*, 87–93.
- Leprieux, G., Remke, M., Rotblat, B., Dubuc, A., Mateo, A.R., Kool, M., Agnihotri, S., El-Naggar, A., Yu, B., Somasekharan, S.P., et al. (2013). The eEF2 kinase confers resistance to nutrient deprivation by blocking translation elongation. *Cell* *153*, 1064–1079.
- Liu, M., Sjogren, A.K., Karlsson, C., Ibrahim, M.X., Andersson, K.M., Olofsson, F.J., Wahlstrom, A.M., Dalin, M., Yu, H., Chen, Z., et al. (2010). Targeting the protein prenyltransferases efficiently reduces tumor development in mice with K-RAS-induced lung cancer. *Proc. Natl. Acad. Sci. USA* *107*, 6471–6476.
- Martineau, Y., Azar, R., Müller, D., Lasfargues, C., El Khawand, S., Anesia, R., Pelletier, J., Bousquet, C., and Pyronnet, S. (2014). Pancreatic tumours escape from translational control through 4E-BP1 loss. *Oncogene* *33*, 1367–1374.

- Mazur, P.K., Reynoird, N., Khatri, P., Jansen, P.W., Wilkinson, A.W., Liu, S., Barbash, O., Van Aller, G.S., Huddleston, M., Dhanak, D., et al. (2014). SMYD3 links lysine methylation of MAP3K2 to Ras-driven cancer. *Nature* *510*, 283–287.
- Mazur, P.K., Herner, A., Mello, S.S., Wirth, M., Hausmann, S., Sánchez-Rivera, F.J., Lofgren, S.M., Kuschma, T., Hahn, S.A., Vangala, D., et al. (2015). Combined inhibition of BET family proteins and histone deacetylases as a potential epigenetics-based therapy for pancreatic ductal adenocarcinoma. *Nat. Med.* *21*, 1163–1171.
- Morgens, D.W., Wainberg, M., Boyle, E.A., Ursu, O., Araya, C.L., Tsui, C.K., Haney, M.S., Hess, G.T., Han, K., Jeng, E.E., et al. (2017). Genome-scale measurement of off-target activity using Cas9 toxicity in high-throughput screens. *Nat. Commun.* *8*, 15178.
- Morgenstern, J.P., and Land, H. (1990). Advanced mammalian gene transfer: High titre retroviral vectors with multiple drug selection markers and a complementary helper-free packaging cell line. *Nucleic Acids Res.* *18*, 3587–3596.
- Morris, J.P., 4th, Cano, D.A., Sekine, S., Wang, S.C., and Hebrok, M. (2010). Beta-catenin blocks Kras-dependent reprogramming of acini into pancreatic cancer precursor lesions in mice. *J. Clin. Invest.* *120*, 508–520.
- Murn, J., and Shi, Y. (2017). The winding path of protein methylation research: Milestones and new frontiers. *Nat. Rev. Mol. Cell Biol.* *18*, 517–527.
- Orimo, A., Gupta, P.B., Sgroi, D.C., Arenzana-Seisdedos, F., Delaunay, T., Naeem, R., Carey, V.J., Richardson, A.L., and Weinberg, R.A. (2005). Stromal fibroblasts present in invasive human breast carcinomas promote tumor growth and angiogenesis through elevated SDF-1/CXCL12 secretion. *Cell* *121*, 335–348.
- Robichaud, N., Sonenberg, N., Ruggero, D., and Schneider, R.J. (2018). Translational control in cancer. *Cold Spring Harb. Perspect. Biol.* Published online June 29, 2018. <https://doi.org/10.1101/cshperspect.a032896>.
- Ruggero, D., Montanaro, L., Ma, L., Xu, W., Londei, P., Cordon-Cardo, C., and Pandolfi, P.P. (2004). The translation factor eIF-4E promotes tumor formation and cooperates with c-Myc in lymphomagenesis. *Nat. Med.* *10*, 484–486.
- Sanjana, N.E., Shalem, O., and Zhang, F. (2014). Improved vectors and genome-wide libraries for CRISPR screening. *Nat. Methods* *11*, 783–784.
- Schmidt, E.K., Clavarino, G., Ceppi, M., and Pierre, P. (2009). SUnSET, a nonradioactive method to monitor protein synthesis. *Nat. Methods* *6*, 275–277.
- Schuller, A.P., and Green, R. (2018). Roadblocks and resolutions in eukaryotic translation. *Nat. Rev. Mol. Cell Biol.* *19*, 526–541.
- Stewart, S.A., Dykxhoorn, D.M., Palliser, D., Mizuno, H., Yu, E.Y., An, D.S., Sabatini, D.M., Chen, I.S., Hahn, W.C., Sharp, P.A., et al. (2003). Lentivirus-delivered stable gene silencing by RNAi in primary cells. *RNA* *9*, 493–501.
- Truitt, M.L., and Ruggero, D. (2016). New frontiers in translational control of the cancer genome. *Nat. Rev. Cancer* *16*, 288–304.
- Truitt, M.L., Conn, C.S., Shi, Z., Pang, X., Tokuyasu, T., Coady, A.M., Seo, Y., Barna, M., and Ruggero, D. (2015). Differential requirements for eIF4E dose in normal development and cancer. *Cell* *162*, 59–71.
- Van Noort, J.M., Kraal, B., Sinjorgo, K.M., Persoon, N.L., Johanns, E.S., and Bosch, L. (1986). Methylation in vivo of elongation factor EF-Tu at lysine-56 decreases the rate of tRNA-dependent GTP hydrolysis. *Eur. J. Biochem.* *160*, 557–561.
- Zhu, L., Shi, G., Schmidt, C.M., Hruban, R.H., and Konieczny, S.F. (2007). Acinar cells contribute to the molecular heterogeneity of pancreatic intraepithelial neoplasia. *Am. J. Pathol.* *171*, 263–273.

## STAR★METHODS

## KEY RESOURCES TABLE

Reagent or Resource	Source	Identifier
<b>Antibodies</b>		
β-actin	Sigma-Aldrich	Cat# A4700; RRID: AB_476730
MUC5AC	Thermo Fisher Scientific	Cat# 145P1
Ki67	BD Bioscience	Cat# 550609; RRID: AB_393778
Phospho-Histone H 3	Millipore	Cat# 06-570; RRID: AB_310177
Cleaved Caspase 3	Cell Signaling Technologies	Cat# 9664; RRID: AB_2070042
CK19	Developmental Studies Hybridoma Bank	Cat# Troma-III; RRID: AB_2133570
anti-Mouse HRP	Cell Signaling Technologies	Cat# 7076; RRID: AB_330924
anti-Rabbit HRP	Cell Signaling Technologies	Cat# 7074; RRID: AB_2099233
eEF1AK55me1	ABclonal Biotechnology	N/A
eEF1AK55me2	ABclonal Biotechnology	N/A
eEF1AK55me3	ABclonal Biotechnology	N/A
eEF1A	Millipore	Cat# 05-235; RRID: AB_309663
β-tubulin	Millipore	Cat# 05-661; RRID: AB_309885
puromycin	Millipore	Cat# MABE343; RRID: AB_2566826
METTL13	Bethyl Laboratories	Cat# A304-195A; RRID: AB_2620392
peroxidase-conjugated streptavidin	Jackson ImmunoResearch	Cat# 016-030-084; RRID: AB_2337238
eEF1A2	Abnova	Cat# H00001917-A01; RRID: AB_489646
eIF3A	Abcam	Cat# ab86146; RRID: 2096634
RPS6	Abcam	Cat# ab70227; RRID: 1270413
RPL6	Abcam	Cat# ab126100; RRID: 11127520
CD45-Biotin	eBiosciences	Cat# 13-0451-81
CD31-Biotin	eBiosciences	Cat# 13-0319-80
Ter119-Biotin	eBiosciences	Cat# 13-5921-81
Biotin Micro Beads	Miltenyi Biotec	Cat# 130-042-401
<b>Bacterial and Virus Strains</b>		
One Shot TOP10	Invitrogen	Cat# C404003
Adenovirus-Cre	Baylor College of Medicine, Viral Vector Production Core	Cat# Ad5-CMV-Cre
DH5α	Thermo Fisher Scientific	Cat# K4520-1
BL21	Thermo Fisher Scientific	Cat# C6070-03
<b>Biological Samples</b>		
Human PDAC and LAC Tissue Array	MD Anderson Pathology	N/A
<b>Chemicals, Peptides, and Recombinant Proteins</b>		
Geneticin	Thermo Fisher Scientific	Cat# 10131027
Blasticidin S	Thermo Fisher Scientific	Cat# R21001
Puromycin	Thermo Fisher Scientific	Cat# A1113802
Hygromycin B	Corning	Cat# 30240CR
G418 Sulfate	Corning	Cat# MT30234CI
MACS separation columns	Miltenyi Biotec	Cat# 130-042-401
Complete Protease Inhibitor Cocktail	Sigma-Aldrich	Cat# 4693159001
Phosphatase Inhibitor Cocktail	Thermo Fisher Scientific	Cat# 78420
Hydrogen Peroxide	Thermo Fisher Scientific	Cat# H325-500
Sequencing Grade Modified Trypsin	Promega	Cat# V5113

(Continued on next page)

**Continued**

Reagent or Resource	Source	Identifier
Glu-C	Promega	Cat# V1651
Collagenase-VIII	Sigma-Aldrich	Cat# C2139
TRIzol Reagent	Invitrogen	Cat# 15596018
Forane (Isoflurane)	AbbVie	Cat#B506
Caerulein	Sigma-Aldrich	Cat# C9026
Soybean trypsin inhibitor	Sigma-Aldrich	Cat# T6522
Rat Tail Collagen	Corning	Cat# 354236
Recombinant mouse EGF	Thermo Fisher Scientific	Cat# PMG8044
Bovine Serum Albumin (BSA)	Thermo Fisher Scientific	Cat# BP9703100
TransIT-293	Mirus Bio	Cat# MIR-2706
SUPERase In RNase Inhibitor	Thermo Fisher Scientific	Cat# AM2694
RNasin Ribonuclease Inhibitors	Promega	Cat# N2511
GTP solution	Thermo Fisher Scientific	Cat# R1461
L-lysine-2HCl	Thermo Fisher Scientific	Cat# 88429
L-arginine-HCl	Thermo Fisher Scientific	Cat# 88427
L-proline	Thermo Fisher Scientific	Cat# 88430
<sup>13</sup> C <sub>6</sub> , <sup>15</sup> N <sub>2</sub> -L-lysine HCl	Silantes GmbH	Cat# 211604102
<sup>13</sup> C <sub>6</sub> , <sup>15</sup> N <sub>4</sub> -L-arginine HCl	Silantes GmbH	Cat# 201604102
l-azidohomoalanine (AHA)	Click Chemistry Tools	Cat# 1066-100
Biotin-PEG4-Alkyne	Click Chemistry Tools	Cat# TA105-25
Peptides: AEMGKGSFYAWVLDKLGKGGK-biotin (X = Kme0, Kme1, Kme2, Kme3)	Chinapeptides	N/A
<b>Critical Commercial Assays</b>		
RNeasy Mini Kit	QIAGEN	Cat# 74106
ZymoPURE Plasmid Miniprep Kit	Zymo	Cat# D4211
ZymoPURE II Plasmid Maxiprep Kit	Zymo	Cat# D4203
DAB Substrate Kit	Abcam	Cat# ab64238
Vectastain ABC kit	Vector Laboratories	Cat# PK-6100
BCA Protein Assay Kit	Pierce	Cat# 23227
ECL Substrate	Amersham	Cat# RPN2106
PCR Mycoplasma Test Kit I/C	PromoKine	Cat# PK-CA91-1096
ATPase/GTPase Activity Assay Kit	Sigma	Cat# MAK113-1KT
Cell Proliferation ELISA BrdU (colorimetric)	Roche	Cat# 11647229001
Coomassie Plus assay	Thermo Fisher Scientific	Cat# 23236
InstantBlue Protein Stain	Expedeon	Cat# ISB1L
SilverQuest Silver Staining Kit	Thermo Fisher Scientific	Cat# LC6070
Click Chemistry Reaction Buffer Kit	Click Chemistry Tools	Cat# 1001
Site-directed mutagenesis kit	Agilent	Cat# 200523
MACS LS column	Miltenyi Biotec	Cat# 130-042-401
<b>Experimental Models: Cell Lines</b>		
Human: 293T/17 cells	ATCC	Cat# CRL-11268
U2OS	ATCC	Cat# HTB-96
hTERT RPE-1	ATCC	Cat# CRL-4000
A549	ATCC	Cat# CCL-185
T3M4	Riken	Cat# RCB1021
PaTu8902	DSMZ	Cat# ACC 179
Colo-357	ECACC	Cat# 94072245
L3.3	RRID	Cat# CVCL_8147

(Continued on next page)

**Continued**

Reagent or Resource	Source	Identifier
NCI-H520	ATCC	Cat# HTB-182
NCI-H2170	ATCC	Cat# CRL-5928
HT1080	ATCC	Cat# CCL-121
IMR90	ATCC	Cat# CCL-186
Experimental Models: Organisms/Strains		
Mouse: <i>Kras</i> <sup>LSL-G12D</sup>	The Jackson Laboratories	Strain# 008179
Mouse: <i>p53</i> <sup>lox/lox</sup>	The Jackson Laboratories	Strain# 008462
Mouse: <i>Ptf1a</i> <sup>Cre</sup>	(Kawaguchi et al., 2002)	MGI# 2387812
Mouse: <i>Mettl13</i> <sup>lox/lox</sup>	In this study	N/A
Mouse: <i>NOD.SCID-IL2Rg</i> <sup>-/-</sup> (NSG)	The Jackson Laboratories	Strain# 005557
Oligonucleotides		
sgRNA: Control: 5'-CTTCGAAATGTCGGTTCGGT-3'	This paper	N/A
sgRNA: METTL13-1: 5'-GGATGTGTCTCACAAAGGTG-3'	This paper	N/A
sgRNA: METTL13-2: 5'-CTGAAGGATGTGTCTCACAA-3'	This paper	N/A
sgRNA: eEF1A2: 5'-CTAGCCGCCACTCAGTTGG-3'	This paper	N/A
sgRNA: eEF1A1/2-1: 5'-ATTTGAGAAGGAGGCTGCTG-3'	This paper	N/A
sgRNA: eEF1A1/2-2: 5'-GTTTCGAGAAGGAGGCGGCTG-3'	This paper	N/A
sgRNAs for KMT Library: <a href="#">Table S1</a>	This paper	N/A
Recombinant DNA		
Plasmid: lentiCRISPRv2	(Sanjana et al., 2014)	Addgene #52961
Plasmid: lentiCRISPRv2 hygro	A gift from Brett Stringer	Addgene #98291
Plasmid: psPAX2	Trono Lab Packaging and Envelope Plasmids	Addgene #12260
Plasmid: pMD2.G	Trono Lab Packaging and Envelope Plasmids	Addgene #12259
Plasmid: pCMV-dR8.2 dvpr	(Stewart et al., 2003)	AddGene #8455
Plasmid: pCMV-VSV-G	(Stewart et al., 2003)	Addgene #8454
Plasmid: pUMVC	(Stewart et al., 2003)	Addgene #8449
Plasmid: pBABE-neo	(Morgenstern and Land, 1990)	Addgene #1767
Plasmid: pWZL Blast GFP	(Orimo et al., 2005)	Addgene #12269
Plasmid: pGEX-6P-1	GE Healthcare	Cat# 28-9546-48
Plasmid: pcDNA3.1(+)	Thermo Fisher Scientific	Cat# V7020
Plasmid: pENTR3C	Thermo Fisher Scientific	Cat# A10465
Plasmid: pLenti6.2 V5-DEST	Thermo Fisher Scientific	Cat# V36820
Software and Algorithms		
Prism 7	GraphPad	<a href="https://www.graphpad.com/">https://www.graphpad.com/</a> ; RRID:SCR_002798
Excel for Mac 2016	Microsoft	<a href="https://www.microsoft.com/en-us/">https://www.microsoft.com/en-us/</a> ; RRID:SCR_016137
Leica Application Suite X (LAS X)	Leica	<a href="https://www.leica-microsystems.com/">https://www.leica-microsystems.com/</a> ; RRID:SCR_013673
ImageJ – Fiji package	Freeware	<a href="http://fiji.sc">http://fiji.sc</a> ; RRID:SCR_002285
Origin Pro 8	Microcal	<a href="https://www.originlab.com/">https://www.originlab.com/</a> ; RRID:SCR_002815
Horos	GNU Lesser General Public License, Version 3.0	<a href="https://horosproject.org/">https://horosproject.org/</a>
Other		
RPMI 1640 Medium	Corning	Cat# MT10017CV
DMEM Medium	Corning	Cat# MT10040CV

(Continued on next page)

**Continued**

Reagent or Resource	Source	Identifier
McCoy's Medium	Corning	Cat# MT10050CV
EMEM Medium	ATCC	Cat# 30-2003
Waymouth's Medium	Thermo Fisher Scientific	Cat# 11220035
Fetal bovine serum	Thermo Fisher Scientific	Cat# 10500056
PBS	Corning	Cat# MT21031CV
Trypsin-EDTA 0.25%	Corning	Cat# MT25053CI
PVDF membrane (0.2 $\mu$ m)	BioRad	Cat# 1620177
PVDF membrane (0.45 $\mu$ m)	Millipore	Cat# IPVH00010
Insulin-Transferrin-Selenium	Thermo Fisher Scientific	Cat# 41400045
Bovine Pituitary Extract (BPE)	Thermo Fisher Scientific	Cat# 13028014
Ethanolamine	Sigma-Aldrich	Cat# E6133
Nicotinamide	Sigma-Aldrich	Cat# N0636

**CONTACT FOR REAGENT AND RESOURCE SHARING**

Further information and requests for resources and reagents should be directed to and will be fulfilled by the Lead Contact: Or Gozani ([ogozani@stanford.edu](mailto:ogozani@stanford.edu)).

**EXPERIMENTAL MODEL AND SUBJECT DETAILS****Mice**

*Ptf1a*<sup>+/-Cre</sup>, *Kras*<sup>+/-LSL-G12D</sup>, *Trp53*<sup>loxP/loxP</sup> mice have been described before ([Hingorani et al., 2003](#)). Conditional *Mettl13*<sup>loxP/loxP</sup> gene (NCBI Reference Sequence: NM\_144877.1) knockout mice were generated in this study. Briefly, to engineer the targeting vector, homology arms and exon 3 (conditional knockout region) was generated by PCR using BAC clone RP23-270A15 and RP24-316J6 from the C57BL/6J library as template. The targeting vector includes the self-excising Neo cassette flanked by Rox sites and exon 3 sequence were flanked by LoxP sites. DTA cassette (Diphtheria Toxin A) was used for negative selection. The linearized vector was subsequently delivered to ES cells (C57BL/6) via electroporation, followed by drug selection, PCR screening, and Southern Blot confirmation. Correctly targeted ES clones were selected for blastocyst microinjection, followed by founder mice production. Founders were confirmed as germline-transmitted via crossbreeding with wild-type animals. In conjunction with germline transmission of the mutant allele the self-excising Neo cassette was deleted. Mice were in a mixed C57BL/6;129/Sv background, and we systematically used littermates as controls in all the experiments. Immunocompromised NSG mice (*NOD.SCID-IL2Rg*<sup>-/-</sup>) were utilized for transplantation studies. All experiments were performed on balanced cohorts of male and female mice as our initial data did not indicate significant differences in disease progression or response to treatment between females or males. All animals were numbered and experiments were conducted in a blinded fashion. After data collection, genotypes were revealed and animals assigned to groups for analysis. For treatment experiments mice were randomized. None of the mice with the appropriate genotype were excluded from this study or used in any other experiments. Mice had not undergone prior treatment or procedures. Husbandry and housing conditions: All mice were fed a standard chow diet *ad libitum* and housed in pathogen-free facility with standard controlled temperature, humidity, and light-dark cycle (12h) conditions with no more than 5 mice per cage under the supervision of veterinarians, in an AALAC-accredited animal facility at the University of Texas M.D. Anderson Cancer Center. All animal procedures were reviewed and approved by the MDACC Institutional Animal Care and Use Committee (IACUC 00001636, PI: Mazur).

**Cell Lines**

293T (female, embryonic kidney) cells were grown in DMEM medium supplemented with 10% fetal calf serum. U2OS (human bone osteosarcoma) cells were cultured in McCoy's 5a medium supplemented with 10% fetal bovine serum and 100 U/mL penicillin/streptomycin. Colo-357 (female, 77 years old, pancreatic cancer), L3.3 (female, 77 years old, pancreatic cancer), PaTu8902 (female, 44 years old, pancreatic cancer), and T3M4 (male, age not reported, pancreatic cancer) and HT1080 (male, 35 years old, fibrosarcoma) cells were cultured in DMEM supplemented with 10% fetal bovine serum, glutamine, and 100 U/mL penicillin/streptomycin. NCI-H2170 (male, age not reported, lung cancer) and NCI-H520 (male, age not reported, lung cancer) cells were cultured in RPMI 1640 medium supplemented with 10% fetal bovine serum and 100 U/mL penicillin/streptomycin. RPE-1 cells (human epithelial cells immortalized with hTERT) were from ATCC and cultured in DMEM:F12 medium supplemented with 10% fetal bovine serum, 100 U/mL penicillin/streptomycin, and 0.01mg/mL hygromycin B. IMR-90 (female, 16 weeks gestation, normal lung fibroblast) were from ATCC and cultured in EMEM supplemented with 10% fetal bovine serum and 100 U/mL penicillin/streptomycin. All cells

were cultured at 37°C in a humidified incubator with 5% CO<sub>2</sub>. Cell lines were authenticated by short tandem repeat profiling and tested negative for mycoplasma (DDC Medical). Serum stimulation was performed after serum-starving overnight using regular 10% fetal bovine serum. For quantitative proteomics, wild-type and METTL13-depleted T3M4 cells were grown in SILAC media containing light or heavy amino acids (<sup>13</sup>C <sup>15</sup>N -L-lysine/<sup>13</sup>C <sup>15</sup>N - L-arginine, see [Key Resources Table](#)).

### Human Tumor Samples

Surgically resected tumor specimens were obtained from patients with histologically confirmed pancreatic cancer and non-small cell lung cancer blinded for age and gender. All surgically resected tumors were collected after written patient consent and in accordance with the institutional review board-approved protocols of the University of Texas M.D. Anderson Cancer Center (LAB07-0854, LAB10-0704). Information on gender and age were not associated with tumor samples and hence blinded.

## METHOD DETAILS

### Pancreatic Cancer Mouse Models

For pancreatic cancer initiation studies acute pancreatitis was induced at 6 to 8 weeks of age in *Ptf1a*<sup>+Cre</sup>;*Kras*<sup>+LSL-G12D</sup> (*Kras*) and *Ptf1a*<sup>+Cre</sup>;*Kras*<sup>+LSL-G12D</sup>; *Mettl13*<sup>loxP/loxP</sup> (*Kras*;*Mettl13*) mice by administration of 8 hourly intraperitoneal (IP) injections of caerulein (100 µg/kg body weight) over 2 consecutive days as described previously ([Mazur et al., 2014](#)). Pancreatic lesions were analyzed 10 d after the last injection. For survival studies, we used *Ptf1a*<sup>+Cre</sup>;*Kras*<sup>+LSL-G12D</sup>;*Trp53*<sup>loxP/loxP</sup> (*Kras*;*p53*) and *Ptf1a*<sup>+Cre</sup>;*Kras*<sup>+LSL-G12D</sup>;*Trp53*<sup>loxP/loxP</sup>; *Mettl13*<sup>loxP/loxP</sup> (*Kras*;*p53*;*Mettl13*) mice, which develop aggressive disease. Mice were followed for signs of disease progression. At the end of the experiment, tumors were processed for biochemical, histological and immunohistochemical analysis. Histopathological analysis was conducted on de-identified slides based on the classification consensus.

### LAC Mouse Models

To generate tumors sporadically in the lungs of *Kras*<sup>+LSL-G12D</sup> and *Kras*<sup>+LSL-G12D</sup>; *Mettl13*<sup>loxP/loxP</sup> mutant mice, we used replication-deficient adenoviruses expressing Cre-recombinase (Ad-Cre) to deliver transient Cre recombinase expression to infected cells of the lung, as previously described ([Mazur et al., 2014](#)). Briefly, 8 to 10-week old mice were anesthetized by continuous gaseous infusion of 2% isoflurane for at least 10 min using a veterinary anesthesia system (D19 Vaporizer, Vetland Medical). Ad-Cre was delivered to the lungs by intratracheal intubation. Prior to administration, Ad-Cre was precipitated with calcium phosphate to improve the delivery of Cre by increasing the efficiency of viral infection of the lung epithelium. Mice were treated with one dose of 5 × 10<sup>6</sup> PFU of Ad-Cre (Baylor College of Medicine, Viral Vector Production Core). Mice were analyzed for tumor formation and progression at 16 weeks after infection.

### Magnetic Resonance Imaging

Magnetic Resonance Imaging (MRI) experiments were performed on *Kras*;*p53* and *Kras*;*p53*;*Mettl13* mutant mice at an age of 7 weeks. Before imaging, mice were anesthetized by continuous gaseous infusion of 2% isoflurane for at least 10 min using a veterinary anesthesia system (D19 Vaporizer, Vetland Medical). During imaging, the dose was kept at 2% isoflurane, animal temperature was maintained and continuously monitored, respiratory and ECG monitoring were performed using an MRI-compatible physiological monitoring system (Small Animal Instruments, Inc) and eyes were protected with an eye ointment. MRI was performed using the Biospec USR70/30 (Bruker Biospin MRI, Billerica, MA) a small animal experimental MR imaging system based on an actively-shielded 7 T magnet with a 30 cm bore and cryo-refrigeration. The system is equipped with 6 cm inner-diameter gradients that deliver a maximum gradient field of 950 mT m<sup>-1</sup>. A 3.5 cm inner-diameter linear birdcage coil transmits and receives the MR signal. For image acquisition, T2-weighted, respiratory gated, multi-slice imaging will be performed with respiration held to under 25 breaths per minute to minimize motion artifacts in the abdomen. The rapid acquisition with relaxation enhancement (RARE) T2-weighted pulse sequence was modified to include an effective Te (time of echo) of 38 ms, echo train length 9.5 ms, and number of averages equal to 4 in both the coronal and axial planes with a total TR (time repetition) of 2000 ms. A three-orientation (axial, sagittal, and coronal) scout image using a fast, low-angle single shot sequence was obtained to localize the mouse pancreas. Between 18 and 20 coronal and axial slices were acquired per mouse with a slice thickness of 0.7 mm and slice spacing of 1 mm to cover the entire pancreas. In plane, pixel sizes of 0.156 mm × 0.156 mm with a matrix size of 256 × 192 and field of view (FOV) of 40 mm × 30 mm was chosen to minimize in plane partial volume effects, maintain a FOV sufficient to cover the abdomen, while also providing sufficient throughput for the experiment. MR images were analyzed using an open source Horos processing software. Pancreas tumor burden was measured by tracing the outer border of the region of suspected lesions on each slice after image intensities were normalized. Analysis was conducted on de-identified images. Tumor volume (V) was assessed, using three-dimensional volumetric measurements according to the modified Simpson rule. In all contiguous transverse images, the area of tumor (A) in each slice was

multiplied by the slice profile (0.7 mm slice thickness plus 1 mm intersection gap), and total tumor volume was automatically calculated by summation of the adjacent volume according to the formula:

$$V = T_s \times \left( \sum_{i=1}^n A_i \right)$$

where  $T_s$  is the thickness of each slice,  $i$  is the individual slice number and  $n$  is the total number of slices.

### Histology and Immunohistochemistry

Tissue specimens were fixed in 4% buffered formalin for 24 hours and stored in 70% ethanol until paraffin embedding. 3- $\mu$ m sections were stained with hematoxylin and eosin (HE) or used for immunohistochemical studies. Human tissue sections were collected in accordance with the institutional review board-approved protocols of the University of Texas M.D. Anderson Cancer Center (LAB05-0854). Immunohistochemistry (IHC) was performed on formalin-fixed, paraffin embedded mouse and human tissue sections using a biotin-avidin method as described before (Mazur et al., 2014). The following antibodies were used (at the indicated dilutions): cleaved caspase 3 (1:200), Ki67 (1:1,000), MUC5AC (1:500), METTL13 (1:100) and eEF1AK55me2 (1:500). Sections were developed with DAB and counterstained with hematoxylin. Pictures were taken using a Leica microscope equipped with the LAX software. Analysis of the tumor area and IHC analysis was done using ImageJ software by measuring pixel units. Quantification of chromogen intensity was performed by measuring the reciprocal intensity of the chromogen stain. Briefly, standard RGB color images acquired from bright field microscopy have a maximum intensity of value 250 (represented by white, unstained areas) as measured by the standard intensity function in the open source Fiji software (ImageJ). We subtracted the intensity of a stained tissue sample from 250, thereby deriving a reciprocal intensity that is directly proportional to the amount of chromogen present.

### Preparation of Pancreatic Epithelial Explants Culture

Pancreatic epithelial explants from 6-week old wild-type mice were established by modification of previously published protocols (Mazur et al., 2014). In brief, the whole pancreas was harvested and treated twice with 1.2 mg/ml Collagenase VIII. Following multiple wash steps with McCoy's medium containing soybean trypsin inhibitor (SBTI, 0.2 mg/ml), digested samples were filtered through a 100  $\mu$ m filter, resuspended in culture medium (Waymouth's MB 752/1 supplemented with 0.1% BSA, 0.2 mg/ml SBTI; 50  $\mu$ g/ml bovine pituitary extract, 10  $\mu$ g/ml Insulin, 5  $\mu$ g/ml transferrin, 6.7 ng/ml selenium in 30% fetal bovine serum) and allowed to recover for 1h at 37°C. Thereafter, cells were pelleted and resuspended in culture medium supplemented with penicillin G (1000 U/ml), streptomycin (100  $\mu$ g/ml), amphotericin B, 0.1% fetal bovine serum, and an equal volume of rat tail collagen and immediately plated on plates pre-coated with 2.5 mg/ml of rat tail collagen type I. In stimulation experiments, recombinant mouse EGF was added to a final concentration of 25 ng/ml. For quantification, acinar explants were seeded in triplicate. Cell clusters were counted from at least 3 optical fields/well and reported as a percentage of acinar clusters and duct-like spheres. The quantification was performed in two independent experiments; the number of mice is reported in the main text.

### Meta-analysis of Gene Expression

Meta-analysis of public PDAC and NSCLC datasets. We downloaded raw data for gene expression studies (7 pancreatic cancer, 6 NSCLC) from the NCBI GEO and EBI ArrayExpress. After re-annotating the probes, each dataset was normalized separately using gcRMA. We applied two meta-analysis approaches to the normalized data. Briefly, the first approach combines effect sizes from each dataset into a meta-effect size to estimate the amount of change in expression across all datasets. For each gene in each dataset, an effect size was computed using Hedges' adjusted  $g$ . If multiple probes mapped to a gene, the effect size for each gene was summarized using the fixed effect inverse-variance model. We combined study-specific effect sizes to obtain the pooled effect size and its standard error using the random effects inverse-variance technique. We computed  $z$ -statistics as a ratio of the pooled effect size to its standard error for each gene and compared the result to a standard normal distribution to obtain a nominal  $P$ -value.  $P$ -values were corrected for multiple hypotheses testing using false discovery rate (FDR). We used a second non-parametric meta-analysis that combines  $P$ -values from individual experiments to identify genes with a large effect size in all datasets. Briefly, we calculated a  $t$ -statistic for each gene in each study. After computing one-tail  $P$ -values for each gene, they were corrected for multiple hypotheses using FDR. Next, we used Fisher's sum of logs method, which sums the logarithm of corrected  $P$ -values across all datasets for each gene and compares the sum against a chi-square distribution with  $2k$  degrees of freedom, where  $k$  is the number of datasets used in the analysis.

### Patient-derived Cancer Xenografts

Surgically resected tumor specimens were obtained from patients with histologically confirmed pancreatic cancer and non-small cell lung cancer blinded for age and gender. All surgically resected tumors were collected after written patient consent and in accordance with the institutional review board-approved protocols of the University of Texas M.D. Anderson Cancer Center (LAB07-0854, LAB10-0704). PDX tumors were generated by transplanting small tumor fragments isolated directly from surgical specimens subcutaneously into mice. In each case we first propagated the sample in NSG mice. For reconstitution assays, collected PDX tumors were minced using a razor blade and digested in collagenase digestion buffer at 37°C for 1 hour. Cells were passed through 100  $\mu$ m and

40  $\mu\text{m}$  cell strainers and centrifuged for 1200 rpm for 8 min. Cells were incubated in RBC lysis buffer for 2 min and then resuspended in 6 mL of media and spun through 0.5 mL of serum layered on the bottom of the tube to remove cellular debris. Contaminating human or mouse hematopoietic and endothelial cells (CD45, Ter119, CD31) are depleted using biotin conjugated anti-mouse CD45, CD31 and Ter119 antibodies and separated on a MACS LS column using anti biotin microbeads. The isolated cells are transiently cultured on several matrigel coated plates and infected with lentivirus carrying sgRNA Mettl13 (shMettl13) and cDNA of METTL13 WT, METTL13 catalytic dead mutant and briefly selected using appropriate antibiotics. Then cells were collected, mixed with matrigel (1:1) and transplanted to the flanks of NSG mice. When tumors became palpable, they were calipered every 3 days to monitor growth kinetics. Tumor volume was calculated using the formula:  $\text{Volume} = (\text{width})^2 \times \text{length} / 2$  where *length* represents the largest tumor diameter and *width* represents the perpendicular tumor diameter.

### Transfection and Viral Transduction

Transient expression was performed using TransIT-293 (Mirus Bio) following the manufacturer's protocol. For CRISPR-Cas9 knockouts, virus particles were produced by co-transfection of 293T cells with the lentiCRISPR v2 /hygro construct expressing indicated sgRNAs, pCMV-VSV-G and pCMV-dR8.2 dvpr in a ratio of 5:2:3 by mass. 48 hours after transfection, target cells were transduced with 0.45  $\mu\text{m}$  filtered viral supernatant and 4  $\mu\text{g}/\text{mL}$  polybrene. Cells were selected 24h after media replacement with 12.5  $\mu\text{g}/\text{mL}$  puromycin for RPE-1 or 250  $\mu\text{g}/\text{mL}$  hygromycin B for other cell lines. For METTL13 reconstitution, cells were transduced with retroviral pBABE or pWZL constructs using pUMVC and pCMV-VSV-G in a ratio of 2:1:1 by mass. The subsequent selection was carried out with 800  $\mu\text{g}/\text{mL}$  G-418 for NCI-H2170, 2 mg/mL G-418 for T3M4, or 10  $\mu\text{g}/\text{mL}$  blasticidin for 293T cells. For eEF1A2 reconstitution, T3M4 cells were transduced with pLenti6.2 plasmid, pCMV-dR8.2 dvpr and pCMV-VSV-G in a ratio of 5:3:2 by mass and selected with 20  $\mu\text{g}/\text{mL}$  blasticidin.

### Plasmids

Protein sequences were METTL13 (accession number NP\_057019.3), eEF1A1 (accession number NP\_001393.1), and eEF1A2 (accession number NP\_001949.1). Bacterial expression plasmids were created using pGEX-6P-1. Transient mammalian expression was conducted using pcDNA3.1(+). lentiCRISPRv2 was used for CRISPR-Cas9 knockouts in RPE-1 cells, while lentiCRISPRv2 hygro was used in all other cell lines. For stable expression in mammalian cells, METTL13 was cloned into pBABE-neo and pWZL Blast GFP. eEF1A2 was originally cloned into pENTR3C and then recombined into pLenti6.2 V5-DEST. The inserts were amplified by PCR using specific clones from the human ORFeome library as templates. Single point mutations of METTL13 and eEF1A2 were generated by site-directed mutagenesis.

### CRISPR-Cas9 Knockout Library Screen

107 known and candidate KMTs were identified based on literature analyses (e.g., (Clarke, 2013)). The top three sgRNAs targeting each putative KMT were taken from a previously published genome-wide human sgRNA library (Morgens et al., 2017) (Table S1). The control sgRNA, which shows no effect on growth in multiple cell lines, was designed to be at least 2 bases mismatched to anything in the human genome. A total of 322 KMT sgRNAs were cloned into the lentiCRISPR v2 vector. Lentivirus particles were produced as described above. U2OS cells in 6-well plates were infected with virus in 4  $\mu\text{g}/\text{mL}$  polybrene for 2 days, then expanded into 10 cm plates for 3 days in puromycin at 2  $\mu\text{g}/\text{mL}$ . Lysate from each plate was collected in 1 mL RIPA buffer (10 mM Tris-HCl pH 8, 150 mM NaCl, 1 mM EDTA, 0.5 mM EGTA, 1% Triton, 0.1% SDS) supplemented with protease inhibitor cocktail. For Western analysis, 40  $\mu\text{L}$  of cell lysates were mixed with 10  $\mu\text{L}$  of 5  $\times$  SDS loading buffer and boiled for 5 min. 20  $\mu\text{L}$  was resolved by SDS-PAGE, transferred to a PVDF membrane, and probed with the anti-eEF1AK55me2 antibody for screening. Tubulin was used as a loading control.

### Immunoblot Analysis and Immunoprecipitation

For western blot analysis, cells were lysed in RIPA buffer with 1 mM PMSF and protease inhibitor cocktail. Protein concentration was determined using the Pierce Coomassie Plus Assay. Protein samples were resolved by SDS-PAGE and transferred to a PVDF membrane (0.45  $\mu\text{m}$ ). Dot blot analysis was performed by directly loading 1  $\mu\text{L}$  of the indicated amounts of biotinylated peptides onto a PVDF membrane (0.2  $\mu\text{m}$ ). The following antibodies were used (at the indicated dilutions): eEF1AK55me1 (1:3,000), eEF1AK55me2 (1:10,000), eEF1AK55me3 (1:5,000), eEF1A (1:5,000), beta-tubulin (1:5,000), puromycin (1:2,000), METTL13 (1:2,000), peroxidase-conjugated streptavidin (1:10,000), eIF3A (1:5,000), RPS6 (1:2,000), RPL6 (1:3,000), eEF1A2 (1:2,000). All secondary antibodies were used at 1:10,000 dilution. Protein bands were visualized using Amersham ECL or Amersham ECL Prime Western Blotting Detection Reagent.

For immunoprecipitation of endogenous eEF1A, equal amounts of whole cell extracts (WCEs) were incubated with anti-eEF1A at 4°C for overnight and then with protein G magnetic beads at 4°C for 2 hours. The beads were washed with cell lysis buffer at 4°C three times, boiled in Laemmli buffer, and then frozen until processed for MS analysis as described below.

### Expression and Purification of Recombinant Proteins

GST fusion proteins were expressed in BL21 *Escherichia coli* by overnight culture at 20°C in LB medium (10 g/L tryptone, 5 g/L yeast extract, and 10 g/L NaCl) supplemented with 0.1 mM IPTG (isopropyl 1-thio-  $\beta$ -D-galactopyranoside, Sigma), purified using Glutathione Sepharose 4B (GE Healthcare) and eluted in 10 mM reduced glutathione (Sigma). Protein concentrations were measured using Pierce Coomassie Plus Assay. DTT was added to the protein solution at a final concentration of 20 mM. Recombinant human core histones were expressed and purified by ion-exchange chromatography. The histones were combined in equimolar ratio under denaturing conditions and dialyzed against high salt buffer to assemble octamers. Octamers were purified by gel filtration chromatography. Nucleosomes were subsequently assembled with the optimized 601 DNA sequence that was amplified with a 5' biotinylated primer.

For purification of Flag-tagged eEF1A1, eEF1A1 bearing a C-terminal Flag tag was expressed by transient transfection in wild-type or METTL13-depleted 293T cells that were reconstituted with METTL13<sub>WT</sub> or METTL13<sub>G58R</sub>, respectively. After 48h transfection, eEF1A was isolated from whole cell extracts using anti-Flag M2 affinity gel (Sigma) according to the instructions of the manufacturer and eluted with 3  $\times$  Flag peptides (Sigma). The resulting purified eEF1A1 was immediately used for enzymatic reactions.

### Structural Modeling of METTL13 (1-400)

Structural modeling of the first 400 residues of METTL13 (METTL13 1-400) was performed using the I-TASSER software package. Based on the amino acid sequence of METTL13<sub>1-400</sub>, the program identified structural templates from Protein Data Bank (<https://www.rcsb.org/>), which were then subject to template-based fragment assembly simulations to generate the structural model. The relative orientation of the two subdomains of METTL13<sub>1-400</sub>, MTase and SBD, was manually arranged in a similar manner as that of the corresponding domains of PrmA (Demirci et al., 2007).

### Polysome Profiling

Wild-type or METTL13-depleted T3M4 cells were seeded into six 15-cm Petri dishes ( $\sim 10 \times 10^6$  cells per dish) 24 hours prior to serum starvation for 16h followed by replacement with fresh medium for 2h. Cells were treated with 100  $\mu$ g/mL cycloheximide and incubated for 2 min at 37°C. Cells were washed and scraped in cold PBS containing 100  $\mu$ g/mL cycloheximide, pelleted and lysed in lysis buffer (5 mM Tris pH7.4, 2.5 mM MgCl<sub>2</sub>, 1.5 mM KCl, 100  $\mu$ g/mL cycloheximide, 2  $\mu$ M DTT, 0.5% Triton, 0.5% Na-DOC, 100 U/mL SUPERase In RNase inhibitor and protease inhibitors). Lysates were cleared for 10 min at 14,000 rpm at 4°C. RNA contents were determined by Nanodrop and 500  $\mu$ g of RNA were loaded on 10% to 50% sucrose gradients made in 15 mM Tris pH7.4, 15 mM MgCl<sub>2</sub>, 150 mM NaCl and prepared using a BioComp Gradient Station. Gradients were spun for 2 hours in a TH-641 rotor (Sorvall) at 40,000 rpm and 4°C. Gradients were analyzed (260 nm) and fractions collected with a BioComp Gradient Station.

### Methylation and GTPase Assays

*In vitro* methylation assays were performed similar to as described in (Mazur et al., 2014) by combining 3  $\mu$ g of recombinant proteins or 1  $\mu$ g of peptides and equal amounts of recombinant enzymes in a methyltransferase buffer (50 mM Tris pH 8.0, 20 mM KCl, 5 mM MgCl<sub>2</sub>, and 10% glycerol) supplemented with 1 mM S-adenosyl-methionine (SAM, New England Biolabs) or deuterated AdoMet (C/D/N Isotopes) or 2  $\mu$ Ci of tritiated AdoMet (American Radiolabeled Chemicals). The reaction mixtures were incubated overnight at 30°C. Reactions were resolved by SDS-PAGE, followed by autoradiography, Coomassie stain or mass spectrometry analysis.

For *in vitro* methylation assay on ribosomes, 40S and 60S ribosomal subunits and 80S ribosomes were isolated from cytoplasmic extract of T3M4 cells as described in **Polysome Profiling**. The eluting fractions were dialyzed twice in 2 L of 100 mM Tris, pH 8.0 (MCWO 3500) and then concentrated (MWCO 3000) by centrifugation at 14,000  $\times$  g. Methylation reactions were carried out in the methyltransferase buffer containing 3  $\mu$ g of recombinant METTL13 (amino acids 1-498), 17.5  $\mu$ L of concentrated ribosomes, and 1 mM S-adenosyl-methionine or 2  $\mu$ Ci of tritiated AdoMet at 30°C for overnight. The reactions were resolved by SDS-PAGE, followed by autoradiography, Coomassie stain or western blot analysis.

GTPase assays were performed in triplicate using ATPase/GTPase Activity Assay Kit (Sigma) following the manufacturer's protocol. Briefly, 3  $\mu$ g of Flag-tagged eEF1A1K55me0/2 purified from 293T cells (as described above) were incubated with increasing amounts of GTP in 30  $\mu$ L of the reaction buffer provided by the kit at 37°C for 3 hours. The reactions were terminated by adding 200  $\mu$ L of the kit reagent and incubating for an additional 30 min at room temperature. For GTPase activation by aminoacyl-tRNA (aa-tRNA), the GTPase assays were performed using 3  $\mu$ g of Flag-tagged eEF1A1K55me0/2, 500  $\mu$ M GTP, 100 ng/ $\mu$ L total aa-tRNAs and 25-30 units RNasin ribonuclease inhibitors (Promega) in 30  $\mu$ L of the reaction buffer. Isolation of total aa-tRNAs from 293T cells was performed at 4°C using phenol/chloroform extraction under acidic conditions. Formation of hydrolyzed free phosphate was measured at a wavelength of 620 nm, and absorbance was compared with a standard curve. The readings of background blank and negative control reactions were subtracted from the sample readings. The kinetic parameters were evaluated by fitting the data to the Michaelis-Menten equation in Origin Pro 8.

### Mass Spectrometry of eEF1AK55 Methylation

Recombinant and immunoprecipitated eEF1A were separated by SDS-PAGE and stained using InstantBlue Protein Stain (Expedeon). Bands were cut and destained in 50% acetonitrile (ACN), 50% ammonium bicarbonate (NH<sub>4</sub>HCO<sub>3</sub>, 50mM) for 10 min twice.

Gel pieces were incubated in 50 mM  $\text{NH}_4\text{HCO}_3$  containing 10 mM DTT at 60°C for 30 min, followed by treatment with 25 mM iodoacetamide in 50 mM  $\text{NH}_4\text{HCO}_3$  at room temperature for 45 min. In-gel digestion was performed using 100 ng/ $\mu\text{L}$  Glu-C in 50 mM phosphate buffer (pH 7.8) at 37°C or 10 ng/ $\mu\text{L}$  trypsin in 50 mM  $\text{NH}_4\text{HCO}_3$  at room temperature for overnight. Two consecutive peptide extractions were processed with 5% formic acid, 49% water, and 50% ACN. The resulting peptides were dried by speedvac, desalted using C18 StageTips (Thermo Fisher Scientific), and analyzed on an Orbitrap Elite mass spectrometer. Methylation states of eEF1AK55 were manually inspected. Selected ion chromatograms for peptides spanning eEF1AK55 were extracted using Xcalibur Qual Browser (Thermo). The settings were as follows:

Peptide 49-61, *m/z* 501.255 (me0), 505.927 (me1), 510.599 (me2) and 515.271 (me3), 10 p.p.m  
 Peptide 49-61 (deuterated K55me), *m/z* 501.255 (me0), 506.933 (me1), 512.6115 (me2) and 518.290 (me3), 10 p.p.m  
 Peptide 52-62, *m/z* 664.356 (me1), 671.364 (me2) and 678.372 (me3), 10 p.p.m  
 Peptide 52-62 (deuterated K55me), *m/z* 665.865 (me1), 674.382 (me2) and 682.900 (me3), 10 p.p.m

### Proteome-wide Labeling and Analysis of METTL13 Substrates

Wild-type and METTL13-depleted T3M4 cells were grown in SILAC media containing either normal amino acids ('light') or modified amino acids ('heavy') for two weeks and lysed in RIPA buffer with 1 mM PMSF and protease inhibitor cocktail. A 2-way experiment was performed – the 'forward' condition combining light WCE + METTL13 with heavy WCE - METTL13 and the 'reverse' condition combining heavy WCE + METTL13 with light WCE - METTL13 at a ratio of 1:1 by mass. 10  $\mu\text{g}$  of the lysates of each pair were resolved by SDS-PAGE and stained using a SilverQuest Silver Staining Kit. Gel pieces were treated with DTT and iodoacetamide as described above. In-gel digestion was performed using 25 ng/ $\mu\text{L}$  trypsin followed by purification using C18 stage tips. To best extract the methylated peptides from the entire proteome, the resulting digestion products were analyzed on an Orbitrap Elite mass spectrometer and an Orbitrap Fusion mass spectrometer (Thermo Scientific). Data obtained from the two instruments were combined and processed using MaxQuant version 1.3.0.5 (Cox and Mann, 2008) and allowing as variable modifications – methionine oxidation; mono- and dimethylation of arginine; and mono-, di- and tri-methylation of lysine.

### Cell Assays

For cell proliferation assays, cells were seeded at  $2 \times 10^5$  cells/mL in triplicate in 6-well plates. Cell counts were acquired by Countess II FL Automated Cell Counter (Thermo Fisher Scientific) at indicated days for 8-10 days. After each counting, the cells were maintained at a density between  $2-4 \times 10^5$  cells/mL. Trypan blue was used to stain non-viable cells. Cell numbers were expressed relative to  $1 \times 10^5$  cells/mL.

Bromodeoxyuridine (BrdU) incorporation assay were conducted fusing Cell Proliferation ELISA BrdU Kit. Cells were seeded in 96-well plates (1,000 cells/well for HT1080, PaTu8902; 2,000 cells/well for T3M4 and colo-357; and 4000 cells for IMR90) and treated with drug concentrations as indicated in the text or with a vehicle for 72h. Absorbance at 370 nm (corrected for absorbance at the reference wavelength of 492 nm) was measured using a microplate reader (Benchmark Plus microplate reader; Bio-Rad) according to a manufacturer's instructions. Tests were performed in two biological replicates, each carried out in a triplicate. BrdU incorporation is expressed as a fraction of vehicle (DMSO) treated control. For viable cell counting,  $1 \times 10^5$  HT1080, PaTu8902, T3M4 and colo-357 cells and  $2 \times 10^5$  IMR90 cells were seeded in 6-well plates and treated with drug concentrations as indicated in the text or with a vehicle for 72h. Non-viable cells were excluded using Trypan blue staining. Tests were performed in two biological replicates, each carried out in a triplicate. Viable cell count is expressed as a fraction of vehicle (DMSO) treated control. Proliferation curves were generated and fitted using GraphPad [using log(inhibitor) versus response – Variable slope (four parameters)].

### Translation Assays

For SUnSET assays (Schmidt et al., 2009), wild-type or METTL13-depleted T3M4 and NCI-H2170 cells were seeded at  $2-4 \times 10^5$  cells/mL in 6-well plates 24 hours prior to serum starvation. For serum stimulation, cells were maintained in regular media containing 10% fetal bovine serum for an optimized period (2 hours for T3M4 and 1 h for NCI-H2170). Puromycin pulses were performed by incubating the cells with 10  $\mu\text{g}/\text{mL}$  puromycin for 15 min at 37°C. Cells were then washed with cold PBS and lysed in RIPA buffer supplemented with 1 mM PMSF and protease inhibitor mixture. 5-10  $\mu\text{g}$  of the whole cell lysate were assayed by western blot analysis using the anti-puromycin antibody.

For labeling newly synthesized proteins, T3M4 cells were maintained in DMEM free of cysteine and methionine for 1h, then grown in DMEM containing 100  $\mu\text{g}/\text{mL}$  methionine or AHA (l-azidohomoalanine) for 2 hours. T3M4 cells under serum starvation were cultured in DMEM free of cysteine and methionine for 1h, then grown for 2h in DMEM containing 10% fetal bovine serum and 100  $\mu\text{g}/\text{mL}$  methionine or AHA. Cells were then harvested, washed with PBS on ice and lysed in RIPA buffer. Click reactions were performed using Click Chemistry Reaction Buffer Kit (Click Chemistry Tools) following the manufacturer's protocol. Briefly, 50-100  $\mu\text{g}$  of whole cell lysates were incubated with 40  $\mu\text{M}$  Biotin-PEG4-Alkyne for 30 min. The proteins were extracted with methanol and chloroform and 1-5  $\mu\text{g}$  were assayed by western blot analysis using streptavidin-conjugated horseradish peroxidase.

## QUANTIFICATION AND STATISTICAL ANALYSIS

Please refer to the Figure Legends or the Experimental Details for description of sample size ( $n$ ) and statistical details. All values for  $n$  are for individual mice or individual sample. Sample sizes were chosen based on previous experience with given experiments. Cell culture assays have been performed in triplicates and in two independent experiments, unless stated otherwise. Data are expressed as mean  $\pm$  SEM. Differences were analyzed by Spearman's rank correlation, log-rank, two-tailed Student's  $t$  test, Mann-Whitney  $U$  test, one-way ANOVA (using Bonferroni post test), one-sample  $t$  test or  $c^2$ -test using Prism 7 (GraphPad),  $P$ -values  $\leq 0.05$  were considered significant.

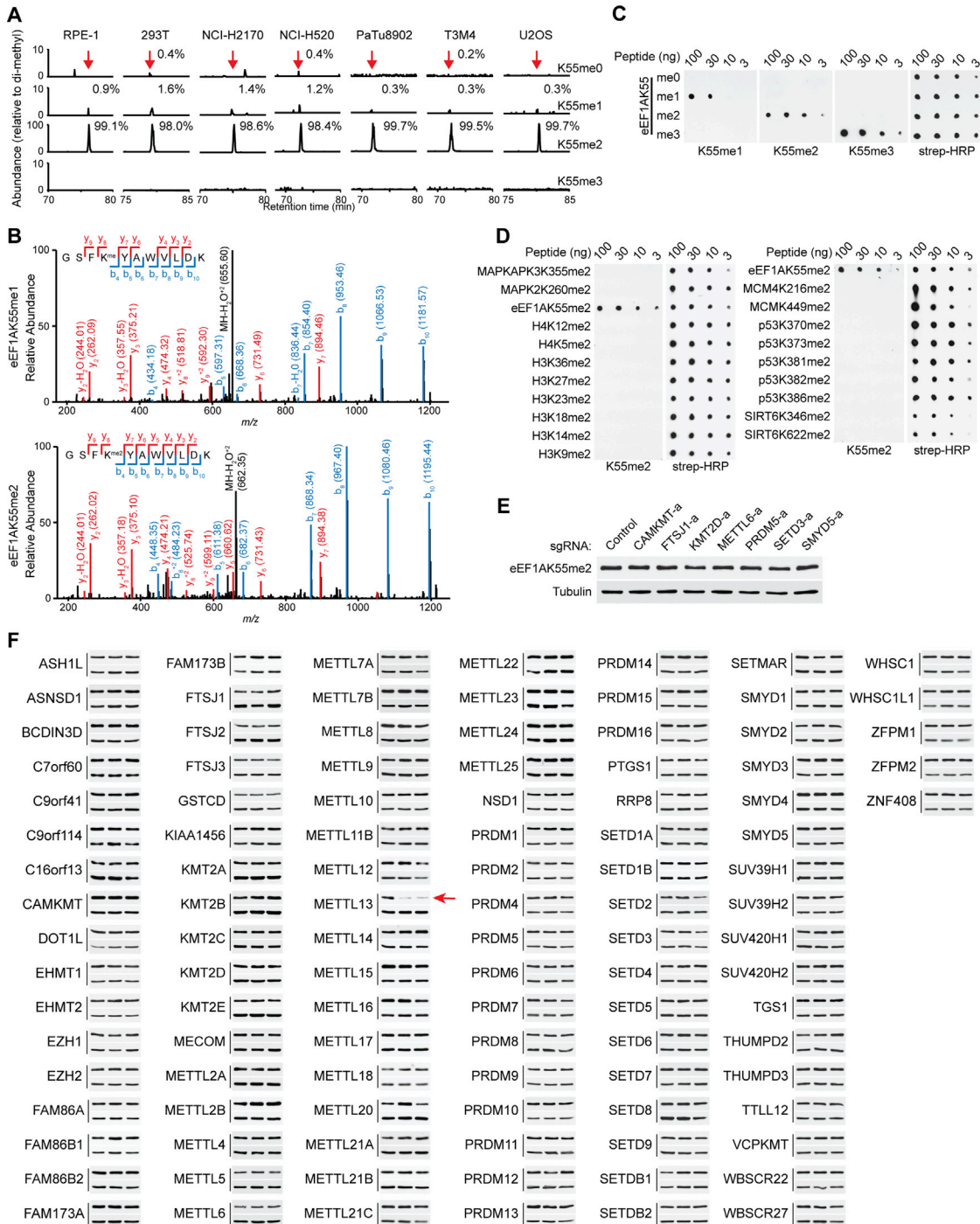


**Figure S1. Identification of METTL13 as a Candidate eEF1A Lysine 55 Methyltransferase, Related to Figure 1**

(A) eEF1AK55 dimethylation is the predominant species in multiple human cell lines. Selected ion chromatograms for non-, mono-, di- and trimethyl eEF1AK55 peptides from GluC digestion of endogenous eEF1A immunoprecipitated from the indicated whole cell lysates (WCEs). HPLC elution profiles show a 10-ppm mass window around expected peptide masses (peptide sequence MGKGSFKYAWVLD, K55 is underlined;  $m/z$  are 501.255, 505.927, 510.599 and 515.271). Red arrows indicate elution peaks of non-, mono- and dimethylated eEF1AK55 peptides in the profiles.

(B) Representative tandem mass spectra identifying mono- (top) and di- (bottom) methylation of endogenous eEF1AK55 immunoprecipitated from WCEs as shown in (A) and followed by trypsin digestion.  $m/z$  for b and y ions observed in spectra were indicated in blue and red, respectively.

(C) Specific recognition of eEF1AK55me by the anti-eEF1AK55me antibodies. Dot blot analysis with state-specific eEF1AK55me1-3 antibodies using the indicated biotinylated peptides. Blots probed with HRP-conjugated streptavidin (strep-HRP) as loading controls.

(legend continued on next page)

---

(D) Specificity of the anti-eEF1AK55me2 antibody in dot blot assays using biotinylated eEF1AK55me2 peptides and 19 different peptides from the indicated proteins that harbor a dimethyl lysine. Blots probed with strep-HRP as loading controls.

(E) Control small guide RNA (sgRNA) for CRISPR-based screen (Figure 1D). Western analysis with the indicated antibodies of WCEs from U2OS cells expressing the control sgRNA from the 322 sgRNA KMT library and seven randomly selected sgRNAs targeting the potential KMTs in the human genome. None of these sgRNAs reduced eEF1AK55me2 levels.

(F) Identification of METTL13 as a candidate eEF1AK55 di-methyltransferase. Western analyses with eEF1AK55me2 and tubulin antibodies of the 322 individual U2OS WCEs. Each cell line expresses CRISPR-Cas9 and one of the 322 sgRNAs. There are three independent sgRNAs targeting 107 known and candidate KMTs in the human genome. For each indicated KMT, eEF1AK55me2 and tubulin protein levels are shown in top and bottom panels, respectively and the data is organized alphabetically.

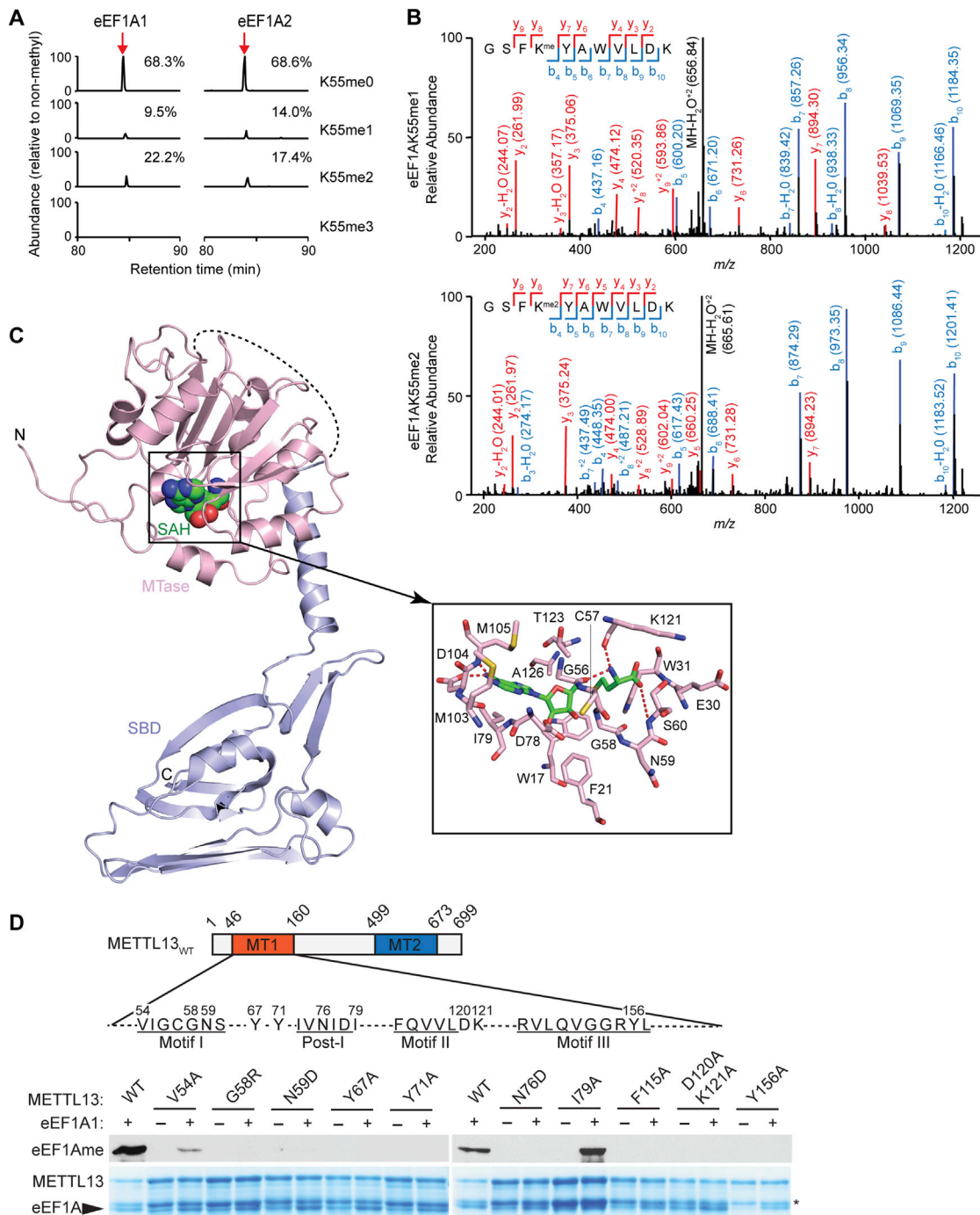


**Figure S2. METTL13 Methylates eEF1AK55 *In Vitro*, Related to Figure 2**

(A) METTL13 methylates eEF1A1/2 at K55 *in vitro*. Selected ion chromatograms for non-, mono-, di- and tri-methyl eEF1A1/2-K55 peptides from GluC digestion after *in vitro* methylation with recombinant METTL13 using deuterated SAM as a methyl donor. HPLC elution profiles show a 10-ppm mass window around expected peptide masses (peptide sequence MGKGSFKYAWVLD, K55 is underlined;  $m/z$  are 501.255, 506.933, 512.6115 and 518.290). Red arrows indicate elution peaks of non-, mono- and dimethylated eEF1AK55 peptides in the profiles.

(B) Representative tandem mass spectra identifying *in vitro* mono- (top) and di- (bottom) methylation of eEF1AK55 by recombinant METTL13 using deuterated SAM and digested with trypsin.  $m/z$  for b and y ions observed in spectra were indicated in blue and red, respectively.

(C) Structural model of METTL13<sub>1-400</sub>, with the MTase domain colored in light pink and the SBD domain colored in light blue. The co-factor byproduct S-Adenosyl-L-homocysteine (SAH) bound to the MTase domain is shown in sphere representation. The MTase and SBD domains are juxtaposed in a random orientation, with

(legend continued on next page)

the linker sequence depicted as a dark dashed line. The SAH-interacting residues are shown in stick representation in the expanded view. The putative hydrogen bonds are shown as red dashed lines.

(D) Identification of point mutations that abrogate METTL3 enzymatic activity. *In vitro* methylation assay on recombinant GST-eEF1A1 with recombinant wild-type METTL3 or the indicated METTL3 single point mutations. Top panel, schematic diagram showing two putative methyltransferase (MT) domains of METTL3 and mutated residues in the MT1 domain. Underlined are signature motifs conserved in METTL3 with other 7βS members with known lysine methylation activity. Middle panel, autoradiogram of methylation assay. Bottom panel, Coomassie stain of proteins in the reaction. Asterisk indicates METTL3 breakdown product.

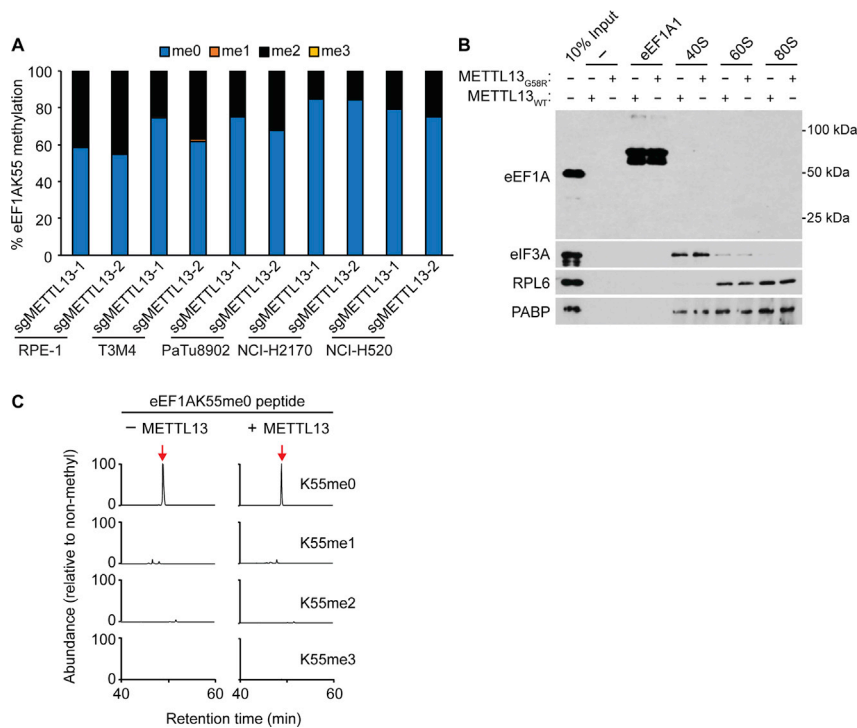
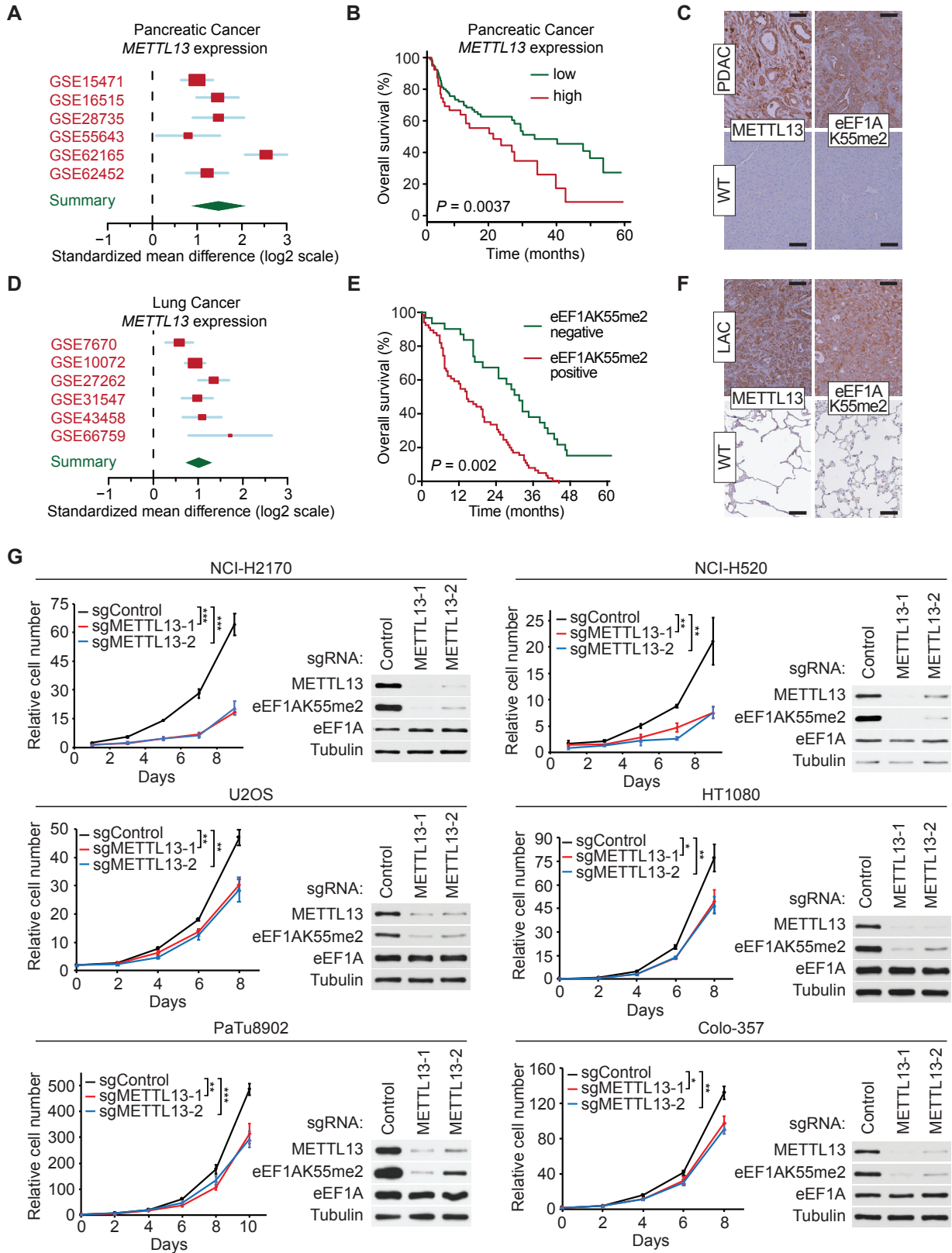


**Figure S3. METTL13 Specifically Methylates eEF1AK55 in Cells, Related to Figure 3**

(A) METTL13 is required for dimethylation of eEF1AK55 in human cell lines. Mass spectrometry-based quantification of eEF1AK55 methylation levels in the indicated cell lines expressing two independent sgRNAs targeting METTL13 and compared to the levels of sgRNA control cells.

(B) Western analysis with the indicated antibodies of *in vitro* methylation reactions on recombinant GST-eEF1A1, 40S, 60S and 80S ribosomes purified from T3M4 cells with recombinant METTL13<sup>WT</sup> or METTL13<sup>G58R</sup>. Input represents cytoplasmic extracts from T3M4 cells used for the isolation of 40S, 60S and 80S. Importantly, no eEF1A signal was detected in purified 40S, 60S and 80S fractions.

(C) Mass spectrometry analysis reveals no METTL13 methylation activity on unmodified eEF1AK55 peptide. Selected ion chromatograms for non-, mono-, di- and tri-methyl eEF1AK55 peptides after *in vitro* methylation on synthesized unmodified eEF1AK55 peptides (aa 45-65) with recombinant METTL13. HPLC elution profiles show a 10-ppm mass window around expected peptide masses (peptide sequence EAAEMGKGSFKYAWVLDKLKA, K55 is underlined; *m/z* are 635.590, 639.094, 642.598 and 646.102). Red arrows indicate elution peaks of non-methylated eEF1AK55 peptide in the profiles.



(legend on next page)

---

**Figure S4. METTL13 and eEF1AK55me2 Are Highly Expressed in Pancreatic and Lung Cancers and Promote Cancer Cell Proliferation, Related to Figure 4**

(A) Summary of *METTL13* expression levels in six publicly available expression datasets of PDAC (n = 294 tumors and n = 141 normal tissue independent samples). Detailed statistical description is in [STAR Methods](#).

(B) Correlation of *METTL13* mRNA expression levels and overall pancreatic cancer survival. Hazard ratio with 95% confidence intervals and log rank *P*-value are calculated. Data from GEO, EGA and TCGA.

(C) Differential epithelial expression levels of *METTL13* and eEF1AK55me2 in human PDAC samples as assessed by immunohistochemistry (72 different samples were stained in total, the representative staining presented). Scale bars: 100  $\mu$ m.

(D) Summary of *METTL13* expression levels in six publicly available expression datasets of LAC (n = 319 tumors and n = 147 normal tissue independent samples). Detailed statistical description is in [STAR Methods](#).

(E) Analysis of correlation of eEF1AK55me2 staining and LAC patient survival assessed by immunohistochemistry. \*\*\**p* < 0.001, log-rank test, 96 different samples were stained in total, the representative staining presented. Scale bars: 100  $\mu$ m.

(F) Differential epithelial expression levels of *METTL13* and eEF1AK55me2 in human LAC samples as assessed by immunohistochemistry (96 different samples were stained in total, the representative staining presented). Scale bars: 100  $\mu$ m.

(G) Cell proliferation rates of human lung cancer cell lines (NCI-H2170 and NCI-H520), human osteosarcoma cell line (U2OS), human fibrosarcoma cell line (HT1080) and human pancreatic cancer cell lines (PaTu8902 and colo357) expressing CRISPR-Cas9 and two independent *METTL13* sgRNAs or a control sgRNA. Top panel, Westerns with indicated antibodies of WCEs from wild-type or *METTL13* deficient cell lines as indicated. Error bars represent SD from three independent experiments. \**p* < 0.05, \*\**p* < 0.01, \*\*\**p* < 0.001, two-tailed unpaired Student's *t* test.

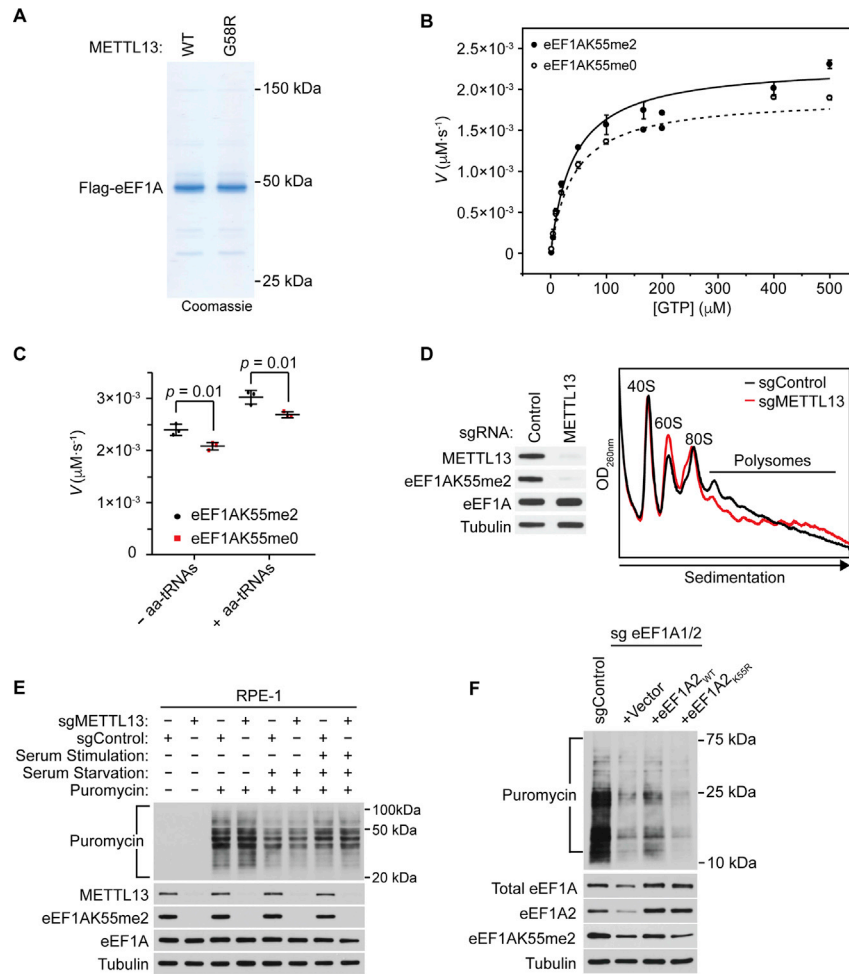


**Figure S5. Methylation Regulates eEF1A GTPase Activity and mRNA Translation in Cells, Related to Figure 5**

(A) Coomassie stain of purified Flag tagged eEF1A1K55me2 and eEF1A1K44me0 protein.

(B) *In vitro* GTP hydrolysis by dimethylated or unmethylated Flag-eEF1A1. Flag-eEF1A1  $\pm$  K55me2 purified from (A) was incubated with increasing amounts of GTP at 37°C for 3h. Error bars represent SD from three independent reactions. Kinetic parameters were obtained by fitting the Michaelis-Menten equation to the plot of velocity of phosphate formation against GTP concentration.

(C) The effect of K55 dimethylation on the GTPase activity of Flag-eEF1A1 is independent of aminoacyl-tRNAs (aa-tRNAs). Flag-eEF1A1  $\pm$  K55me2 purified as in (A) was incubated with 500  $\mu\text{M}$  GTP in reaction buffer at 37°C for 3h in the absence or presence of aa-tRNAs. The y axis shows velocity of phosphate formation. Error bars represent SD from three independent reactions.

(D) Cytosolic extracts were isolated from control or METTL13-depleted T3M4 cells (replicate of Figure 5C) and fractionated on 5%–50% sucrose gradients. Absorbance profiles show distribution of 40 and 60S ribosomal subunits, 80S monosome and polysomes. OD<sub>260nm</sub>, optical density at 260 nm. Left panel, Western analysis represents WCEs from the indicated cell lines used for the polysome profiling.

(E) METTL13 depletion does not impact protein synthesis in non-transformed RPE-1 cells. SUnSET assays as in Figure 5D show no difference in protein production in RPE-1 cells with or without METTL13. After being pulsed with 10  $\mu\text{g}/\text{mL}$  puromycin for 15 min at the indicated conditions, WCEs were isolated and probed with the indicated antibodies.

(F) Requirement for eEF1A55 for serum-stimulated protein synthesis in cells. SUnSET assays after recovery from serum starvation as in Figure 5D with control (sgControl plus vector control) or eEF1A-depleted T3M4 cells complemented with CRISPR-resistant eEF1A2<sub>WT</sub>, eEF1A2<sub>K58R</sub> or control as indicated. WCEs were isolated and probed with the indicated antibodies.

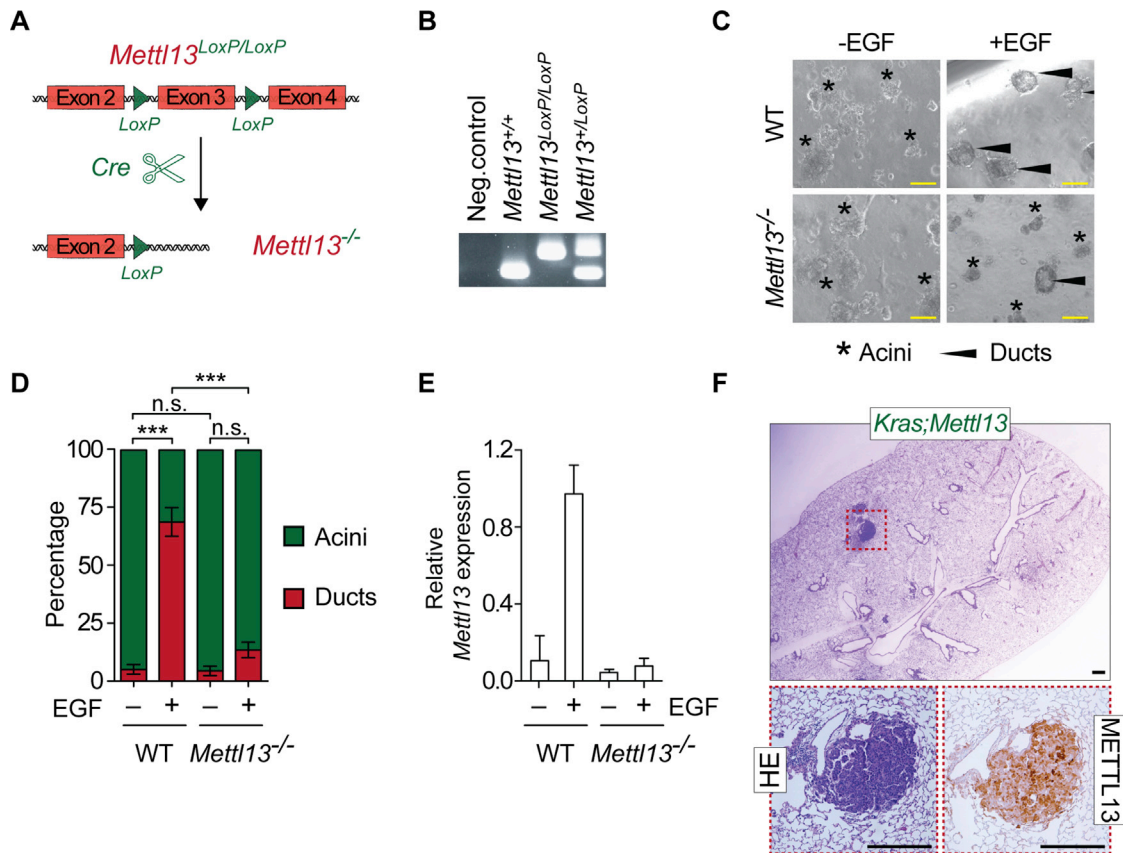


**Figure S6. METTL13 Deletion Represses KRAS-Driven Pancreatic and Lung Tumorigenesis In Vivo, Related to Figure 6**

(A) Schematic of the *Mettl13* conditional allele. In the presence of Cre recombinase, exon 3 is deleted to disrupt *Mettl13* expression.

(B) Deletion of *Mettl13* exon 3 of the conditional allele (Figure S6A) determined by PCR.

(C) METTL13 depletion inhibits ADM. Wild-type (WT, *Ptf1a*<sup>Cre/+</sup>) acinar clusters (asterisk) undergo ADM and form ducts (arrowhead) *ex vivo*, whereas *Ptf1a*<sup>Cre/+</sup>;*Mettl13* mutant (*Mettl13*) acini explants inefficiently form ducts.

(D) Quantification of acinar and ductal clusters from Figure S6C. \*\*\*p < 0.001, n.s. not significant, two-tailed unpaired Student's t test, four independent biological replicas with three technical replicas each. Data are represented as mean ± s.e.m.

(E) *Mettl13* expression by quantitative PCR with reverse transcription (qRT-PCR) analysis at the indicated times from control- and EGF-induced ADM *ex vivo* samples, four independent biological replicas as in Figure S6C.

(F) Immunohistochemical analysis of tumors that emerged in *Kras;Mettl13* LAC model reveals that tumors retained METTL13 expression suggesting incomplete bi-allelic Cre recombination in these clonal growths. Representative staining presented. Scale bars: 1000 μm, insets magnification x10.

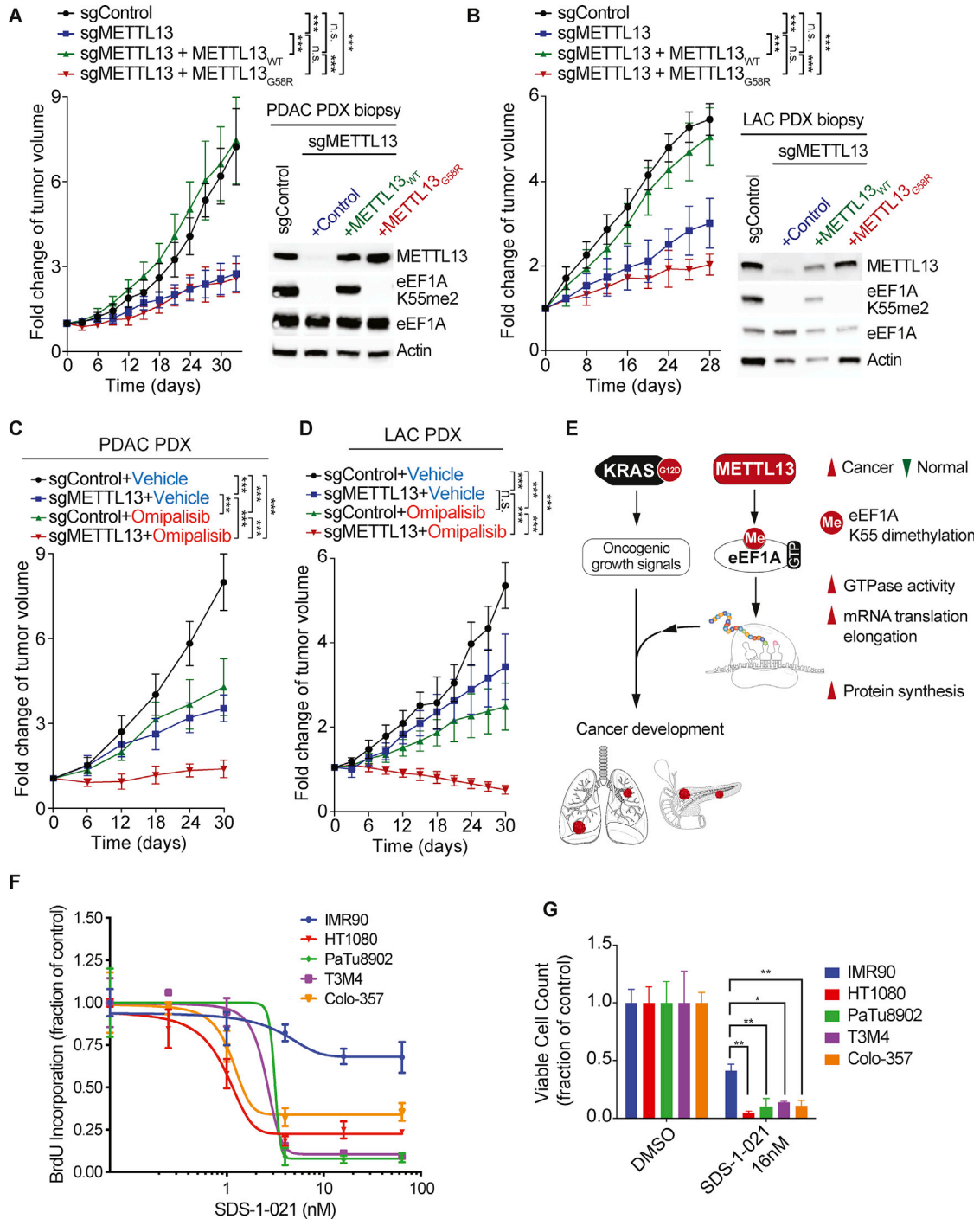


**Figure S7. Depletion of METTL13's Catalytic Activity Inhibits Growth of Pancreatic and Lung Cancer PDX Tumors *In Vivo* and Regression of PDX Tumors by the Combination of METTL13 Depletion and Treatment with PI3K and mTOR Inhibitors, Related to Figure 7**

(A) Tumor volume quantification for patient derived PDAC xenografts modified to express sgRNA METTL13 or sgRNA control and overexpressing wild-type METTL13<sub>WT</sub> or catalytically deficient METTL13<sub>G58R</sub> in mice (n = 8 mice for each treatment group). \*\*\*p < 0.001, two-tailed unpaired Student's t test. Data are represented as mean ± s.e.m. Immunoblots with the indicated antibodies of the PDX biopsies (one representative sample for each condition is shown).

(B) Tumor volume quantification for patient derived LAC xenografts modified to express sgRNA METTL13 or sgRNA control and overexpressing wild-type METTL13<sub>WT</sub> or catalytically deficient METTL13<sub>G58R</sub> in mice (n = 8 mice for each treatment group). \*\*\*p < 0.001, two-tailed unpaired Student's t test. Data are represented as mean ± s.e.m. Immunoblots with the indicated antibodies of the PDX biopsies (one representative sample for each condition is shown).

---

(C) and (D) Tumor volume quantification for patient derived PDAC (C) and LAC (D) xenografts modified to express sgRNA METTL13 or sgRNA Control (see [Figures S7A and S7B](#)) treated with placebo (vehicle) or Omipalisib. Plots showing fold change in tumor volume compared to initial tumor volume. \*\*\* $p < 0.001$ , n.s., not significant, two-tailed unpaired Student's t test. Data are represented as mean  $\pm$  s.e.m. Treatment schedule as in [Figure 7E](#).

(E) Model of the role of METTL13 and eEF1A methylation in enhancing protein synthesis to fuel growth signal-driven tumorigenesis.

(F and G) IMR90 (non-transformed), and the Ras positive HT1080, PaTu8902, T3M4 and colo357 cell lines were treated as indicated with SDS-1-021 for 72h.

(F) Proliferation was determined by BrdU incorporation and expressed as a fraction of the inhibition of BrdU incorporation relative to control (vehicle-treated) cells. Results are presented as mean values  $\pm$  SD ( $n = 3$ ). (G) Viable cell count was measured by Trypan blue exclusion and expressed as a fraction of control (vehicle-treated) cells. Results are presented as mean values  $\pm$  SD ( $n = 3$ ). \* $p < 0.05$ , \*\* $p < 0.01$ , two-tailed unpaired Student's t test.